Highlights

The marsquake catalogue from InSight, sols 0–1011

Savas Ceylan, John F. Clinton, Domenico Giardini, Simon C. Stähler, Anna Horleston, Taichi Kawamura, Maren Böse, Constantinos Charalambous, Nikolaj L. Dahmen, Martin van Driel, Cecilia Durán, Fabian Euchner, Amir Khan, Doyeon Kim, Matthieu Plasman, John-Robert Scholz, Géraldine Zenhäusern, Eric Beucler, Raphaël F. Garcia, Sharon Kedar, Martin Knapmeyer, Philippe Lognonné, Mark P. Panning, Clément Perrin, William T. Pike, Alexander E. Stott, William B. Banerdt

- The V9 catalogue includes 951 events, of which 486 are new since the previous report.
- Multiple large marsquakes with M_W^{Ma}4.0–4.2 were recorded.
- Some new events are within 100 km and beyond the core shadow which were not seen before.
- Four events that locate close to the lander and include chirps have been observed.
- The catalogue also includes 1062 very local events that may be due to thermal stresses.

The marsquake catalogue from InSight, sols 0–1011

Savas Ceylan[a,*], John F. Clinton[b], Domenico Giardini[a], Simon C. Stähler[a], Anna Horleston[c], Taichi Kawamura[d], Maren Böse[a,b], Constantinos Charalambous[e], Nikolaj L. Dahmen[a], Martin van Driel[a], Cecilia Durán[a], Fabian Euchner[a], Amir Khan[a,f], Doyeon Kim[a], Matthieu Plasman[d], John-Robert Scholz[g], Géraldine Zenhäusern[a], Eric Beucler[h], Raphaël F. Garcia[i], Sharon Kedar[j], Martin Knapmeyer[k], Philippe Lognonné[d,l], Mark P. Panning[j], Clément Perrin[h], William T. Pike[e], Alexander E. Stott[i], William B. Banerdt[j]

[a] *Institute of Geophysics, ETH Zurich, Zurich, Switzerland*
[b] *Swiss Seismological Service, ETH Zurich, Zurich, Switzerland*
[c] *School of Earth Sciences, University of Bristol, Bristol, UK*
[d] *Université de Paris, Institut de physique du globe de Paris, CNRS, Paris, France*
[e] *Department of Electrical and Electronic Engineering, Imperial College London, London, UK*
[f] *Physik-Institut, University of Zurich, Zurich, Switzerland*
[g] *Max-Planck-Institut für Sonnensystemforschung, Göttingen, Germany*
[h] *Nantes Université, Université d'Angers, Le Mans Université, CNRS, UMR 6112, Laboratoire de Planétologie et Géosciences, UAR 3281, Observatoire des Sciences de l'Univers de Nantes Atlantique, Nantes, France*
[i] *Institut Supérieur de l'Aéronautique et de l'Espace SUPAERO, Toulouse, France*
[j] *Jet Propulsion Laboratory, California Institute of Technology, Pasadena, CA, USA*
[k] *Institute of Planetary Research, German Aerospace Center, Berlin, Germany*
[l] *Institut Universitaire de France, 1 rue Descartes, Paris, France*

Abstract

The InSight mission (Interior Exploration using Seismic Investigations, Geodesy and Heat Transport) has been collecting high-quality seismic data from Mars since February 2019, shortly after its landing. The Marsquake Service (MQS) is the team responsible for the prompt review of all seismic data recorded by the InSight's seismometer (SEIS), marsquake event detection, and curating seismicity catalogues. Until sol 1011 (end of September 2021),

*Corresponding author

Preprint submitted to Phys. Earth Planet. Inter.

MQS have identified 951 marsquakes that we interpret to occur at regional and teleseismic distances, and 1062 very short duration events that are most likely generated by local thermal stresses nearby the SEIS package. Here, we summarize the seismic data collected until sol 1011, version 9 of the InSight seismicity catalogue. We focus on the significant seismicity that occurred after sol 478, the end date of version 3, the last catalogue described in a dedicated paper. In this new period, almost a full Martian year of new data has been collected, allowing us to observe seasonal variations in seismicity that are largely driven by strong changes in atmospheric noise that couples into the seismic signal. Further, the largest, closest and most distant events have been identified, and the number of fully located events has increased from 3 to 7. In addition to the new seismicity, we document improvements in the catalogue that include the adoption of InSight-calibrated Martian models and magnitude scales, the inclusion of additional seismic body-wave phases, and first focal mechanism solutions for three of the regional marsquakes at distances $\sim$30°.

Keywords: Marsquakes, InSight mission, Mars seismicity catalogue

---

1. Introduction

The primary goal of the InSight mission is to explore the inner structure of Mars (Banerdt et al., 2020). For achieving this purpose, the most critical InSight instrument payload is the SEIS package (Seismic Experiment for Internal Structure), which consists of two 3-component seismometers, named the very broadband (VBB) and the short period (SP) (Lognonné et al., 2019). The InSight lander is also equipped with a set of wind speed, wind direction and pressure sensors (Auxiliary Payload Sensor Suite; APSS) for observing the Martian atmosphere (Banfield et al., 2019), which are crucial for discriminating seismic events from other noise sources.

The mission's nominal duration was one Martian year (about 668 sols, or roughly two Earth years), counting from the day of landing on 2018-11-26 (InSight sol 0; a sol is one Martian day equivalent of ∼24h40m). However, the mission is now well into a second Martian year, and to date, the seismometers continue to perform exceptionally well. InSight is powered by solar panels, which have been progressively affected by dust. By late 2020, available power had become so limited that the scientific instrumentation was selectively turned off. Since then, only the VBB has regularly been operational - the weather sensors and the SP seismometer were only rarely powered on.

The Marsquake Service (MQS) is one of the vital ground segment support services of the mission (Clinton et al., 2018, 2021). The MQS team comprises researchers from the InSight science team, with its operations based at ETH Zurich. The team is responsible for prompt routine data review, detecting the seismic signals, locating quakes, and curating the seismicity catalogue.

When a signal potentially of seismic origin is identified, MQS investigates

possible contamination in the waveforms that may exist due to atmospheric disturbances. If weather sensors are operational during the event, seismic data are checked against pressure and wind channels. Otherwise, MQS utilizes the excitation of lander modes as seen in the seismic data, which are very well correlated with wind speed (Dahmen et al., 2021b; Charalambous et al., 2021).

Once a suspicious signal is confirmed not to be due to atmospheric noise, it is often possible to identify multiple seismic phases that can be interpreted as body waves. When phases are confirmed to be P and S arrivals or their surface reflections (PP and SS, respectively), the event distance is computed following the probabilistic single-station location algorithm (Khan et al., 2016; Böse et al., 2017) using a set of a priori interior models. For events with estimated distances, MQS reports event magnitudes since catalogue version 8 (V8), employing the updated relations provided in Böse et al. (2021). The event backazimuth is obtained using polarization analysis of the primary body waves (Böse et al., 2017), though this is only rarely possible.

MQS continues to classify events by their frequency content. At low amplitudes, when winds are low, the InSight data are characterised by a resonance at 2.4 Hz (Dahmen et al., 2021b; Hobiger et al., 2021), that is also strongly excited during seismic events. The low frequency (LF) family events include energy predominantly below 2.4 Hz, though sometimes also at this resonance. They are similar to teleseismic events observed on Earth, where P and S waves are often identified. The high frequency (HF) family of events are predominantly at and above 2.4 Hz. These events include phases that are assigned to be Pg and Sg and interpreted as crustal guided waves (Giardini et al., 2020; van Driel et al., 2021). Finally, super high frequency (SF) events are very short duration events with energy above 5 Hz. In

addition to event type, an event quality is assigned to each event, ranging from A (best - located) to D (worst - very weak energy, possibly speculative).

This paper describes V9 of the catalogue (InSight Marsquake Service, 2022), spanning sols 0–1011 (from 2018-11-26 until 2021-10-01), which was released on 2022-01-01. For a small number of LF family events in V9, recent studies have successfully identified secondary phase arrivals, including reflections within the crust such as pS, at the free surface (PP, PPP, SS, SSS), and core (ScS). These have been used to generate the first Martian models constrained by seismic data (Stähler et al., 2021b; Khan et al., 2021; Knapmeyer-Endrun et al., 2021). Up to catalogue V8 (InSight Marsquake Service, 2021b), MQS has used pre-landing structural models for LF family event distance determination (Clinton et al., 2021). In the V9 catalogue, all events have their distances revised using this most recent model set of Khan et al. (2021) and Stähler et al. (2021b).

The majority of LF family events located by the MQS are closer than the core shadow zone (98–102°) with distances determined by direct P and S arrivals. Two events (S0976a and S1000a) in this new catalogue lie beyond the core shadow and have PP and SS phases (Horleston et al., 2022). MQS located S0976a in the Valles Marineris region 146°(±7°) away from InSight. The distance of S1000a is 116°(±9°), but a backazimuth determination based on the PP arrival alone is not clear and therefore not provided. S1000a includes very broadband energy that rises well above 2.4 Hz - a unique feature among broadband events in the catalogue. Further, S1000a shows the first Pdiff phase observed so far. These two events are the largest magnitude marsquakes recorded since landing. The largest HF family event (S0976b) was also observed on the same sol as the most distant marsquake. Further, the V9 catalogue includes four recent HF family events with very short epi-

Event type	Total number	Quality A	Quality B	Quality C	Quality D
Low frequency family					
LF	45 (+17)	4 (+3)	9 (+3)	18 (+7)	14 (+4)
BB	24 (+11)	2 (+1)	6 (+5)	13 (+4)	3 (+1)
High frequency family					
VF	56 (+33)	–	21 (+12)	27 (+19)	8 (+2)
HF	95 (+43)	–	51 (+20)	36 (+18)	8 (+5)
2.4 Hz	731 (+382)	–	46 (+8)	263 (+126)	422 (+248)
Other events					
SF	1062 (+350)	–	–	252 (+124)	810 (+226)

Table 1: Breakdown of V9 catalogue in terms of event type and quality. The changes since the V3 catalogue (InSight Marsquake Service, 2020b) as reported by Clinton et al. (2021) are indicated in parentheses. These statistics also include some re-classification of event types and qualities during the routinely performed checks before each catalogue release. See the text for definition of event types and qualities. By definition, all QA events have both distance and backazimuth determined. S0183a is the only exception to this rule, having a full location but assigned as QB since the event distance is speculative.

central distances that include chirp signals not previously observed.

Here, we provide an update of Clinton et al. (2021), documenting the seismicity (Figs. 1 and 2) that occurred until sol 1011 (2021-10-01). In the following sections, we first summarize the data collected until sol 1011 (Fig. 3). Then, we report on major changes to both MQS procedures and the catalogue content since the release of V3 (InSight Marsquake Service, 2020b), including updated magnitude relations (Böse et al., 2021), first focal mechanism solutions for three marsquakes (Brinkman et al., 2021), and additional seismic phase picks (Khan et al., 2021; Stähler et al., 2021b). Finally, we describe the evolution of marsquakes and key catalogue features for each of the LF and HF event families and the SF events, with descriptions of fundamental attributes for the key new events between 478-1011. A breakdown of the catalogue in terms of event type and quality is provided in Table 1. Supp. Tables S1 and S2 list all marsquakes individually and include key event attributes.

2. Data collection

InSight is powered by two solar panels. With dust accumulating on these panels, the available power for InSight has steadily decreased over time. The cleaning events from local dust devils, as seen at other Martian landers (Lorenz et al., 2021), had been expected to occur for InSight but have unfortunately not been observed.

The nominal mission duration for InSight was a full Martian year, which was reached on sol 668, and was mainly driven by power expectation. However, InSight has managed to operate well beyond this period. Nevertheless, by late 2020, solar power generation had reduced to the extent that scientific instruments began to be turned off. Around this time, the magnetometer, wind speed, wind direction and pressure sensors were no longer operated continuously. On sol 789 (2021-02-14), the continuous SP operation was also suspended. The data collected across the entire period until sol 1011 are shown in Fig. 3 for a selection of the channels commonly used by MQS from the seismic, weather and magnetic sensors.

Ceylan et al. (2021) summarised the characteristics of seismic data collected up to sol 478, the same period that Clinton et al. (2021) covered for seismicity. For the majority of the mission, and until the SP sensor was turned off, the VBB was acquired at 20 sps (location and channel codes 02.BH? where the question mark is a wildcard) and transmitted to Earth continuously. The SP sensor was acquired at 100 sps (65.EH?), but only transmitted to Earth in short windows via specific requests. MQS routinely requested the 100 sps SP data for each identified marsquake. Once SP was switched off, the VBB was acquired at 100 sps (00.HH?), and since then we have 20 sps VBB transmitted continuously with some event-based VBB

data at 100 sps for significant marsquakes.

A notable gap of 21 sols occurred during the solar conjunction in the first Martian year due to InSight entering safe mode with all science payload turned off. The data were fully collected over the conjunction in the second Martian year.

3. Summary of data and seismicity

Following the completion of the deployment and commissioning phases, both the VBB and SP seismometers exceeded the mission target noise levels (Lognonné et al., 2019; Lognonné et al., 2020). In addition, the steps of placing SEIS on the Martian surface and then covering with the wind and thermal shield (WTS) on sol 76 both led to significant noise reduction (Clinton et al., 2021). Nevertheless, SEIS is still sensitive to the effects of the local weather perturbations, which is evident in diurnal patterns in the seismic recordings. The evolution of the seismic background noise for the VBB vertical component, with detected events overlain, is presented in Fig. 1.

At the beginning of the nominal science monitoring phase (around sol 100), an average sol had rather predictable seismic noise during the spring and summer in the northern hemisphere. Turbulent winds were observed each afternoon which resulted in very high seismic noise. This period was followed by a sharp decline in the noise level shortly before sunset, with subsequently the quietest period of each sol lasting for a few hours. Light winds caused an increase in the noise level in the early morning. Since the initial catalogue description ending on sol 478 (Clinton et al., 2021), InSight has collected almost an entire additional Martian year of data. It has become apparent that the seismic noise is seasonally predictable.

The background seismic noise unfortunately increases dramatically during the autumn and winter seasons at the InSight landing site (Fig. 1). As a result, consistently observed quiet periods in the early evenings disappear. Although the average noise level during the middle of the sol does slightly decrease, the noise in this season is still too high to observe any but a few large quakes that have poor signal to noise. To date, the background noise patterns closely repeat the first Martian year, with minor perturbations even repeating on the same sol one Martian year later. These general noise patterns are also evident in Fig. 4, which tracks the evolving daily noise amplitudes across various percentiles of power spectral density for the dominant frequency ranges within which the HF and LF families are observed.

An overview of noise sources and artefacts was given by Ceylan et al. (2021) as observed in the data until sol 478. A specific group of artefacts named glitches (broadband spikes) are the most dominant features in the seismic data. It is possible to partially remove these spikes (Scholz et al., 2020). However, it is crucial that they should still be carefully considered not only during marsquake characterisation, but also for phase identification and auto-correlation procedures for structural interpretation (Kim et al., 2021) in particular.

From sol 790, we began to observe a new long-period signal. At first, the signal lasted only a few minutes and was relatively low in amplitude at the order of a few nm/s. It became very regular in the following sols, appearing every night as soon as the typical Martian calm evening ends around 22:30 LMST (Local Mean Solar Time). The signal stops during the night, generally between 2:30–4:30 LMST, without a clear correlation with the decrease of atmospheric disturbances. Its maximum amplitude can reach tens of nm/s. It is visible on all raw VBB components (UVW). When the

data are rotated into ZNE, there is almost no energy on the vertical. The polarization of the signal is very stable, with an apparent regular elliptical motion in the horizontal plane. The azimuth is clear and around 21°. The period of the signal is quite constant around 18–25 s with slight oscillations during the nighttime. Finally, we also observe some harmonics of the signal at 6 and 12 s for many sols. An example of this signal is shown in Fig. 5, which is present at the pre-event noise and early part of event S0976a and discussed in the event description section.

4. Revisiting marsquake attributes

This section summarises the conventions that MQS uses to prepare the InSight seismicity catalogue. We refer the reader to Clinton et al. (2021) for a more thorough documentation on event characterisation, classification, and MQS procedures.

When an event is catalogued, MQS assigns two essential attributes for classification: *event type* and *quality*. These properties are qualitative criteria defined early in the mission as MQS started to gain significant experience with the observed signals and background seismic noise. The *event type* is used to classify marsquakes according to their energy content, while *event quality* provides a measure of the significance of an event in terms of the signal-to-noise ratio, seismic phase picks, and ultimately whether a location can be provided. The event numbers per type and quality for the V9 catalogue are provided in Table 1. Event types and qualities for each event in the catalogue are provided in Supp. Tables S1 and S2.

4.1. Event type

The event type indicates the dominant energy content of a marsquake. The natural resonance at 2.4 Hz (Giardini et al., 2020) and a lander related mode at 4 Hz (e.g. Ceylan et al. (2021), Dahmen et al. (2021b)) are the key discriminants for the event type. The traditional seismic events in the catalogue are classified into two main groups as the low frequency family that contains energy predominantly below 2.4 Hz, and in contrast, the high-frequency family contains energy predominantly at and above 2.4 Hz (Fig. 6).

The low frequency family includes two event types as *low frequency* (LF) and *broadband* (BB). The LF events contain energy in all three components, all below 2.4 Hz. The BB events are similar to the LF quakes with energy predominantly at longer periods in three components, but also include energy at and sometimes even above 2.4 Hz.

The high-frequency event family (van Driel et al., 2021) consists of three sub-classes as *2.4 Hz*, *high frequency* (HF), and *very high frequency* (VF). The *2.4 Hz* events exhibit energy limited only around the 2.4 Hz resonance. These events are strongest in the vertical component, consistent with the vertically polarised resonance. The *HF* events have a broader range of frequencies, extending at least above 4 Hz. Strong HF events occasionally show energy below 2.4 Hz, some extending down to ∼4–5 s; however the event energy is predominantly at 2.4 Hz and above. Similar to the 2.4 Hz events, these events have energy in all three components but are strongest in the vertical direction. The *VF* events are a special case within the high-frequency family, as they include energy that rises higher than HF events, typically reaching 10 Hz. Energy can be observed up to 30 Hz and above on occasion. Their high-frequency component is horizontally polarised, with

significantly stronger energy on the horizontal components than the vertical.

Another event type reported in the InSight catalogue is the *super high frequency* (SF) events that are substantially different from the low- and high-frequency families due to their much shorter duration and frequency content (Dahmen et al., 2021a). These ∼10–25-seconds-long signals include energy only above ∼5 Hz and sometimes reach up to ∼30 Hz. Similar to VF events, there is significantly stronger energy on the horizontal components.

Each event in the catalogue is assigned a name following the alpha-numerical convention of *S0000x* (or *T0000x* for SF events), where *0000* is a 4–digit sol number on which the events occur, and x is an alphabetical character to uniquely identify events and typically indicates the order of events on a particular sol.

4.2. Event quality

Event quality is closely related to the signal-to-noise ratio (SNR) of the seismic phase arrivals. MQS employs a four–level quality measure for each event from quality A through D (QA–QD). QA is the highest quality, indicating that MQS was able to identify multiple clear seismic phases in the time domain and compute a robust full location with distance and backazimuth. QB is used to mark the medium quality events with either multiple clear phase identifications but no polarization or vice versa, while QC shows low quality events with signals clearly observed but phase picking is difficult, speculative, and often aided by spectrograms. Lastly, quality D indicates suspicious signals that are weak or may not be attributed to seismicity. We show examples of LF events with degrading event quality in Fig. 7.

All energy above 1 Hz, including the 2.4 Hz resonance, shows highly scattered characteristics (Giardini et al., 2020; van Driel et al., 2021), which

means it is not possible to obtain a reliable backazimuth estimate for individual events using the signal at high frequencies. Therefore, all HF family events are assigned a quality of QB or lower, following the MQS rules.

The SF events (Dahmen et al., 2021a) are different to all other marsquake types catalogued, with very short durations and no identifiable picks. The quality assessment for the SF-type events is limited to C and D, based on the peak amplitude: a quality of C when the peak amplitude is above $2x10^{-9}$ m/s (7–9 Hz bandpass filter), and D otherwise.

In addition to the event quality, the catalogue includes three SNR measures: SNR_S using the seismic waveforms, SNR_W for the wind data, and SNR_P using the pressure data. The SNR_W and SNR_P are reported depending on the data availability of the weather sensors and become rare after autumn 2020, once the weather sensors were no longer continuously operated. All available SNR for each event are indicated in Tables S1 and S2.

4.3. Seismic phase picks and event depths

Once a suspected event is identified, MQS first marks the event window by picking the earliest and latest energy arrivals, labelled as *start* and *end*, respectively. Additionally, a time window of representative background noise near the event is identified by *noise start* and *noise end* phase labels. Following the QuakeML standards (Schorlemmer et al., 2011), all start and end times for event and noise windows are stored in the catalogue as *arrivals*, but no pick uncertainties are assigned.

In the case of the HF event family, high-frequency seismic phases are identified as slope breaks on vertical component STA/LTA (short time average / long time average) envelopes centered around the 2.4 Hz resonance

(Fig. 8). Often, two clear and separated phases are observed. The excitation of the 2.4 Hz resonance is interpreted as trapped energy within the layered Martian crust (Giardini et al., 2020; van Driel et al., 2021); therefore, these phases are labelled as Pg and Sg, respectively, following the phase naming nomenclature for Earth (Storchak et al., 2003). When identified using the envelopes, the uncertainties for Pg and Sg phases are generally assigned as $\pm$10, $\pm$20, or $\pm$60 s. When envelopes and waveforms exhibit sharp onsets for high-quality events, the uncertainties can be as narrow as $\pm$1 s. Typically, phases for the higher frequency VF events are also picked at 2.4 Hz on the vertical component. In order to reflect the energy content of the VF events, the STA/LTA filter is also computed on the horizontals for frequencies 7.9–9 Hz, and used for phase verification.

A handful of the LF family events have high amplitudes above the noise level that allow for clear P and S phase identification in the time domain. The uncertainties are typically chosen as $\pm$1, $\pm$2, or $\pm$5 s for these relatively clear arrivals. When the signal and phase onsets are weaker, phase picking is often aided by spectrograms, with uncertainties of $\pm$20 or $\pm$60 s in general.

For all event types, any other additional phases identified at lower frequencies below 2.4 Hz resonance are labelled as *x1–xn* with appropriate uncertainties assigned as described above. By definition, the broadband events have high-frequency content around 2.4 Hz, which may also exhibit distinct energy arrivals. These phases are labelled as *y1–yn*. Furthermore, the SF events do not include any seismic phase picks since these events do not contain any clear arrivals. All phases for each event are indicated in Supp. Tables S1 and S2.

There are no constraints on event depths as of catalogue V9. Therefore, MQS assigns a fixed value of 50 km to HF and LF families regardless of the

event type and quality. The SF events are not assigned any depths. The event depths will be updated in future versions when positive depth phase identifications are confirmed.

5. Updates in the new catalogue version

In addition to the newly observed seismicity, the V9 catalogue includes updates and additions to both methods and content. Substantial changes are the inclusion of new magnitude definitions (Böse et al., 2021), first focal mechanism solutions (Brinkman et al., 2021) for three marsquakes (S0173a, S0183a, and S0235b), and a first set of surface-reflected body wave picks (PP, PPP, SS, SSS from Khan et al. (2021)) and core reflected transversal S-phases (ScS) from Stähler et al. (2021b). In light of the new seismicity that occurred after Clinton et al. (2021), the event similarity analysis (alignments) has been extended and distances for the older events have been revised. The catalogue is also extended to include alternative source interpretations from other studies (Martire et al., 2020; Kedar et al., 2021). In this section, we describe these updates in more detail.

5.1. New phase labelling conventions

As we observe and identify more complex phases and continue to extend our overall interpretation of the Martian seismicity, we take the opportunity to update the basic conventions used to describe them.

The BB events, by definition, exhibit seismic energy at and above the 2.4 Hz resonance that can often be picked using the 2.4 Hz STA/LTA filter. Prior to V9, these picks were assigned to be Pg and Sg phases, compatible with the phase association of the HF family events picked using the same

filter. However, often only a single 2.4 Hz phase is observed, though sometimes more than 2 can be identified, and it is not likely that distances from these picks can be reconciled with the typical teleseismic BB event distances. Hence, starting from V9, all high-frequency picks for the BB events (including previously labelled Pg and Sg phases) are relabelled as *y1, ..., yn*. The Pg and Sg picks for the HF family events remain the same.

Recently, some of the HF family events exhibit chirp-like signals at lower frequencies extending below 1 Hz. Consequently, all picks identified at frequencies below 2.4 Hz are marked with *x1, ..., xn*. Note that this convention is already being used for long period picks or unknown phase types regardless of the event type.

5.2. Velocity models for inversion

Since V9, the distance estimates for LF family events in the MQS catalogue use new interior models based on the inversion of multiple body wave phases (Khan et al., 2021; Stähler et al., 2021b). The models result from 3 different inversion approaches: (1) a purely "seismic" one that produces a model of linear velocity gradients to fit travel times, conceptually similar to IASP91 (Kennett and Engdahl, 1991). (2) A "geophysical" parametrization that fits the travel times against interior models from thermodynamical modelling (Khan et al., 2018). These models allow for variation of mineralogical compositions, but use an adiabatic temperature profile. (3) A "geodynamical" parametrization, similar to (2), but restricted to one composition. The temperature profile is based on 1D convection simulations (Samuel et al., 2021).

Each approach produced 100 velocity models by Markov Chain Monte Carlo inversion. Together, these 300 models are used to determine the MQS

distances. The software used for estimating event distances can be found on (Stähler, 2020). The models are available from Stähler et al. (2021a), and shown in Fig. 9.

5.3. Updated distance probabilities

Following the release of catalogue V3 (InSight Marsquake Service, 2020b), MQS identified an error in the implementation of the single station distance algorithm (Böse et al., 2017). The P-pick uncertainties were not taken into account, and consequently, the distance probability distributions for LF family events were underestimated. The under-estimation became more significant as the P-phase picking uncertainties increased. This error affected only the width of the probability distributions. Its effects on the final distance determination was minor.

Fig. 10 shows the distances and backazimuths for all LF family events reported in V9. For the subset of events also included in the V3 catalogue and presented in Fig. 9 of Clinton et al. (2021), we also include here the distance computations before and after the software correction. The absolute values of distance estimates remain practically the same, with a maximum change of 3°, which is negligible. The error specifically affects the probability distributions of S0185a and S0474a, both with large P-uncertainties of ±60 s. Our previous error estimates indicate values within the mission requirements (25% for distance; horizontal error bars in Fig. 10). As opposed to prior error estimates, current 2σ errors show that the mission requirements are not met for these two events.

In total, the V9 catalogue includes 27 LF family events with phase-based distances. 13 of these were also reported in the V3 catalogue. Five events out of these do not meet the mission requirements (Fig. 10), while the remaining

events show distributions less than or comparable to the error margin.

For the HF events, the procedure for determining the event distance is unchanged since Clinton et al. (2021) where we assume a simplistic crustal model with a $V_S = 2.3\ km/s$ and $V_P/V_S = 1.7$. The distances for all HF events with their Pg and Sg picks are listed in Supp. Table S2.

5.4. Alignments

Alignment refers to a procedure that provides a first order determination of distance and origin time for LF family events, initially presented in Giardini et al. (2020). The approach relies on identifying similarities amongst seismic events via visual inspection of spectral envelopes (Fig. 11), and weaker events are placed relatively in distance to well located quality A events. It provides an opportunity to review existing phase-based distances, and assign distances to events too weak to have a phase-picked distance estimate. The envelopes are checked against a suite of models, although the final distance estimation is generally made on a single reference model (Fig. 9b).

The alignment procedure uses these high-quality events with known locations as anchors. Each event is individually analyzed on the 3-component spectrograms to identify the frequency range of the dominant energy. Typically, we compute the spectrograms using a window length of 30 s, and an overlap of 50%. The data are detrended and instrument response is removed prior to spectrogram computation. Through practice, we prefer to use acceleration spectrograms, although events are also checked using the data in velocity and displacement as well as with different window lengths. The events are isolated between the frequencies of the dominant energy, i.e. spectrogram content is ignored except for the energy in the event-specific

frequency range. For a majority of the events, this frequency range is 0.2–0.9 Hz. Subsequently, the spectral envelopes are calculated by summing the spectral amplitudes along the frequency axis between the two frequencies. Before the final analysis, contaminated parts of the spectral envelopes (due to instrumental artefacts such as glitches and atmosphere) are masked.

Alignment is a practical way of visualizing an overview of seismic events relative to each other, providing an alternative for interpreting the seismicity, specifically for the events that could not be fully located by MQS. It helps to classify the events that are similar to each other for further analysis and their relative positions in distance-travel time domain. So far, alignments have been efficiently employed for magnitude determinations (Böse et al., 2021), broad structural interpretations (Giardini et al., 2020), and as a gateway for picking additional seismic phases (Khan et al., 2021).

The uncertainties associated with the aligned distances are not trivial to quantify, and typically are rather large at the order of a few degrees. The first source for these large uncertainties arise from the reference model used. Different distances can be found when different model or model sets are used. The window length chosen for calculating the spectral envelopes is also important - longer windows smooth and smear the envelopes. The smearing opens a window of possibilities of performing the alignments, introducing an additional uncertainty margin. Shorter window lengths show more details; however, it becomes often harder to identify and interpret common features. The third and most critical source of uncertainty comes from the envelope interpretation. The alignment is a qualitative practise, highly depending on the perception of main energy packages. In the case of complex events such as S0809a (see the event descriptions section), alignments suggest various solutions.

The InSight catalogue V9 includes a total of 36 events that were aligned (Fig. 11) that is 11 more events since Clinton et al. (2021), and 9 events more than the phase-based approach. In light of the recent results on the interior of Mars (Khan et al., 2021; Stähler et al., 2021b; Knapmeyer-Endrun et al., 2021), the reference model used for the alignment is updated using a representative model from Stähler et al. (2021b) (Fig. 9b). When possible, MQS prefers to keep the aligned distances previously reported in Clinton et al. (2021) unchanged, but accommodates the differential travel time differences by updating the aligned event origin times.

In general, there are five clusters of events that arise from envelope similarities (Fig. 11). The first cluster includes the LF family closest to InSight, distances starting from the Cerberus Fossae events roughly from 28° to 40°. These marsquakes show relatively clear P and S energy in the envelopes. The next family of events do not show any clear S-wave energy. These quakes are aligned using the P-wave and length of its coda in the spectral envelopes around 46°. The third cluster of events located around ∼60° with relatively emergent P- and S-wave energy, and are anchored by a relatively clear QB event S0185a. The events aligned at distances 88–100° are positioned only using their S-wave coda length along the reference S-arrivals. These events, without a high quality anchoring event, are generally noisy with unclear P-energy that is at or below the noise level. Their S-wave coda is relatively longer. Lastly, there are two more distant anchor events, S0976a and S1000a, which show clear but emergent energy for PP and SS waves and are described further in the event description section and in Horleston et al. (2022).

The aligned distances for LF family events are indicated in Supp. Table S1, when available.

5.5. Magnitudes

The magnitude relations for marsquakes were first derived by Böse et al. (2018) using synthetic seismograms produced for a set of pre-launch Martian models that are also listed in Ceylan et al. (2017). In Giardini et al. (2020), these pre-landing relations were updated to better reflect the actual content of marsquakes, subsequently used by Clinton et al. (2021) for V3 and used until V7. Böse et al. (2021) updated these scaling relations using real data from 485 marsquakes that occurred up to October, 2020 (InSight Marsquake Service, 2021a). The relations, first adopted in V8, are also used in V9.

The magnitudes are computed for all events that have an estimated distance, with several scales based on P- and S-wave peak amplitudes for LF events, and the maximum amplitude of excitation around the 2.4 Hz resonance for HF events (Böse et al., 2018; Giardini et al., 2020; Clinton et al., 2021). For all events, the preferred magnitude type is moment magnitude (M_W^{Ma}) derived depending on the event type; hence the dominant event energy.

We show the distance vs moment magnitude distribution in Fig. 12. The largest HF family event in the catalogue is S0976b with a M_W^{Ma}4.1, and for the LF family S0976a with M_W^{Ma}4.2. In general, the HF family events cluster at distances up to 41° with magnitudes below M_W^{Ma}2.5. The LF family events are distributed at larger magnitudes $M_W^{Ma} > 2.5$ and greater distances between ∼30°–146°.

The preferred magnitudes (M_W^{Ma}) for each event are shown in Supp. Tables S1 and S2. In the QuakeML file, all magnitude types are attached to the origins with distances.

5.6. Moment tensors

The first focal mechanisms of three of the marsquakes (S0173a, S0183a, S0235b) were determined in the recent study of (Brinkman et al., 2021) (Fig. 2). The authors approach the problem of source mechanism determination with a single-station using both a grid search method and a direct linear inversion. S0173a and S0235b are both quality A events with clear P- and S-wave arrivals. S0183a is a quality B event, with an impulsive P phase, but exhibits a weak secondary phase with ±60 s uncertainties.

The focal mechanism solutions provided by Brinkman et al. (2021) for all three events suggest an extensional source. In the QuakeML data structure (Schorlemmer et al., 2011), the solutions for these three events are included in the V9 catalogue attached to separate origins other than the preferred origin. The originating study is mentioned in the *creationInfo* element of the origin block in the QuakeML data model.

5.7. Additional body-wave phase picks

Up to catalogue V7, MQS have reported seismic phase picks only from the direct time series analysis and from alignments. From V7, the catalogue includes arrivals identified by two recent studies concentrating on the upper mantle structure (Khan et al., 2021) and the core (Stähler et al., 2021b) of Mars.

Khan et al. (2021) focus on the surface-reflected body wave phase identification (PP, PPP, SS, and SSS) with the purpose of inverting for the upper mantle structure on Mars. The study combines seismic phase picks from three different and independent approaches, using 8 teleseismic marsquakes. Stähler et al. (2021b) extends the phase pick collection of Khan et al. (2021)

concentrating on the core-reflected S-waves (ScS) with a focus on the Martian core.

As of V9 catalogue, these picks are included into the catalogue but not associated with any particular origin. The additional picks can be retrieved using their *publicID* properties under the *pick* object in the QuakeML (Schorlemmer et al., 2011). The *publicID* is constructed with a method identifier (Table 2) to discriminate the teams and methods used (see Khan et al. (2021); Stähler et al. (2021b) for details). The picking method is also available in the *methodID* attribute of the pick. The *creation info* property includes the digital object identifier (DOI) of the originating study. An example for a QuakeML *pick* block is provided in Fig. 13.

Table 2: Additional phases and their method identifiers included in the V9 catalogue from Khan et al. (2021) and Stähler et al. (2021b). The travel paths of each phase is shown in Fig. 9c. An example QuakeML *pick* block is in Fig. 13.

Phase group	Reference	Method identifier
Body waves reflected from free surface (PP, PPP, SS, SSS)	Khan et al. (2021)	TDE: Time-domain envelopes WM: Waveform matching PFV: Polarization filters and vespagrams
Transversal body-waves reflected from the core-mantle boundary (ScS)	Stähler et al. (2021b)	A through E, depending the participating team and their preferred approaches.

5.8. Alternative source interpretations

MQS catalogue versions include alternative source interpretations from other studies as well. Kedar et al. (2021) identify S0105a and S0189a as potential volcanic tremors. This information is included under the *event* element of the QuakeML as *comment* as found in the event XML. Mar-

tire et al. (2020) also suggested that events presenting a single dominant frequency in the 0.4-2 Hz range, with 90° phase shift between horizontal and vertical components, could be generated by horizontally propagating acoustic waves. Similar to additional seismic phase picks, alternative interpretations are not tied to any specific origin.

6. Review of recent significant seismicity

In this section, we summarise the seismicity in V9, and highlight in detail the most significant marsquakes from both the LF and HF families that occurred after sol 478. Significant events that were recorded before this sol are already described in Clinton et al. (2021). Detail event reports include the characteristics of events, seismic phase picks, and location determination when available. All LF and HF events with their key attributes are listed in Supp. Table S1 and S2, respectively.

6.1. LF family

Since sol 478, InSight recorded 28 new LF family events for a new total of 69 (Table 1, Supp. Table S1). The number of QA events increased from 2 to 6, and fully-located events from 3 to 7 (S0183a, described in Clinton et al. (2021), is QB, but a location is provided despite having a very uncertain distance estimate). The magnitude and distance distribution of events is shown in Fig. 12, which also includes HF family events. The seismicity map of the LF family events, including the aligned events, is in Fig. 2.

The two most distant and largest LF events (S0976a and S1000a) occurred within 24 sols - both are the only events with confirmed distances beyond the core shadow that starts at 98–102° distance (Stähler et al., 2021b),

and the first events to be located using body phases further than 60°. Horleston et al. (2022) describes these events in detail. S0976a is the most distant event at 146°, with M_W^{Ma}4.2, and S1000a at 116° has M_W^{Ma}4.1. The strong amplitudes of these events are illustrated in Fig 4. In the bandwidth between 1.5-6 s, S1000a is the largest event seen so far, and S0976a is similar in amplitude to S0235b. S1000a is an exceptional BB event, with a very broad frequency range, including energy below 10 s and exceeding 5 Hz.

There is no obvious difference for the LF event rates between the first marsquake season (spring and summer) and what has been observed so far in the second (Figs. 1 and 4). What is remarkable though is the seasonal variation in the distances observed: In the first season, events were well distributed in distance from Cerberus at 28° out to about 60°. In the second season, events were only located at distances compatible with Cerberus from 28-35°, until the two large distant events occurred. Not surprisingly, no significant LF family marsquake activity was observed during the noisy autumn and winter seasons, though at the end of the season, on sol 729, a LF QD event (S0729a) with very large amplitude ($1.14 \times 10^{-9} m/s$, bandpass 0.2-0.5 Hz) was observed during the strongest wind gust period. Due to the noise conditions, no seismic phases could be identified, so the event has no distance.

In terms of time of sol (Fig. 1), the LF events cluster inside the early evening window as expected, once the winds die down before sunset. Some events are found in the morning period, that occasionally has periods with light winds. It is exceedingly rare to observe events during the high wind periods.

In the following, we present the key marsquakes - first the 4 new Quality A, then some key Quality B events, ordered by quality and date.

6.1.1. S0809a-LF quality A

S0809a (origin time 2021-03-07 11:09:26 UTC, ∼23:33 LMST) occurred during a quiet period of the night (Fig. 14 a). It is the first event that can be located to occur in the 2nd Martian year of InSight. Its equivalent sol in the first year is sol 141, so it occurred earlier in the year than the first QA event in the catalogue, S0173a. The event has energy between ∼1–8 s (Figs. 14b, 15), with clear seismic phase arrivals visible in all three components (Figs. 14b,c and 16). It is the sixth largest LF family event in the catalogue to date, with a magnitude of $\mathrm{M}_{\mathrm{W}}^{\mathrm{Ma}} 3.3 \pm 0.5$.

There is no apparent contamination originating from the Martian atmospheric conditions. Although wind speed and direction data are not available, the pressure data are benign. Further, the known lander modes (Dahmen et al., 2021b) are not excited during the event, meaning that the wind conditions in the vicinity of SEIS and the lander were very calm. (Fig. 14b).

The waveforms are free of instrumental artefacts such as glitches. The signal-to-noise ratio calculated from the seismic data (SNR_S) is 53, the fourth highest value in the catalogue. We obtain an SNR_P of 11.7 from the pressure data. The event does not have an SNR_W since the wind sensors were not operational. The event duration is 19 minutes.

The event time series exhibit four impulsive and linearly polarized arrivals:

(i) The first arrival, which MQS identified as the P–phase, is clearly observed in both time domain and spectrograms on all three components (Figs. 14, 16). The pick uncertainty is assigned as ±1 s. The polarization analysis of this wave package reveals a backazimuth of ∼ 87° (−20°, +18°) from North (Fig. 16b), pointing towards the Cerberus

Fossae region. This observation is further confirmed by an independent method (Zenhäusern et al., 2022) using polarization ellipses shown in Fig. 17.

(ii) The second identified phase, which is labelled as *x1*, has the similar polarization characteristics (azimuth, ellipticity, and inclination) as the initial P–phase (Fig. 17). Its amplitude is higher than the initial P–wave, dominantly observed on the vertical component. The pick uncertainties are $\pm 5s$.

(iii) The third phase is predominantly observed on the horizontal components. The polarization of the wave package shows an azimuth of $\sim 270^\circ$ (Fig. 17). This phase is identified as the direct S–wave arrival by MQS, with an uncertainty of $\pm 5s$.

(iv) The fourth and last significant phase is labelled as *x2*, and shows similar polarization properties as the S–pick mentioned above. Similar to the comparison of P and x1 phases, it has a larger amplitude than the MQS S–pick, clearly observed in the time domain. This phase is the most uncertain of all the phases above with picking errors of $\pm 10s$.

The differential arrival times of S–P, and x2–x1 are 173 and 175 s, respectively. Using the P– and S–phase picks, we compute a distance of $29.8^\circ(-2.0^\circ, +1.9^\circ)$. Assuming x1 and x2 phases are also P– and S–arrivals, we obtain a very similar distance at 30.2°.

In V9, this marsquake is listed as a single event. However, the observations of multiple phases that can be explained with twin P and S phases that have comparable differential times and consistent polarization suggest it is plausible to interpret this event as twin events of similar size and location

occurring within 2 minutes of each other. The final location of the event is the Cerberus Fossae region which is also consistent with our previous observations with the other high quality LF family events in the catalogue (Giardini et al., 2020; Clinton et al., 2021).

Since the waveforms show clear seismic phases that are visible in the time domain and we are able to obtain a robust backazimuth estimate, the event qualifies as a quality A event according to the MQS nomenclature. The alignment distance for this event is 29.5°.

6.1.2. S0820a-LF quality A

S0820a (origin time 2021-03-18 14:51:33 UTC, ∼20:06 LMST) is the second quality A event that occurred after the long period of non-detection due to higher background seismic noise levels during the Martian winter.

The event shows clear P and S arrivals (Fig. 18), which indicate a distance of 30.2°(±2.4°). The noise conditions during the event are calm. The P–wave train is free from contamination, and the polarization analysis (Fig. 19) points to a backazimuth of 88° (−12°, +19°). The event shows energy between ∼1.5–8 s (Fig. 20). The moment magnitude is computed as $M_W^{Ma} 3.3 \pm 0.2$. The event duration is ∼9 minutes.

Similar to S0809a, S0820a is a complex event with two additional phases (x1 and x2) identified:

(i) The first arrival is rather weak in the time series. However, the energy is clear on the vertical component spectrogram. This phase does not show any clear polarization. MQS labelled this arrival as x1, with an uncertainty of ±20 s.

(ii) The second phase, labelled as P (pick uncertainty ±5 s) is clearly

visible in time domain. The phase is impulsive and shows a clear backazimuth of $\sim 88^\circ$ (Fig. 19). The time difference between P and x1 phases is 43 s.

(iii) The third identified phase is labelled as x2 (pick uncertainty ± 10 s), which is visible in the time domain with a polarization $\sim 90^\circ$, similar to what we observe for the S-wave package.

(iv) The S-phase (± 5 s) is also clearly visible in the time domain. The time difference between S and x2 picks is 49 s. This arrival shows an azimuth of $\sim 180^\circ$, with a 90° shift from the P-waves which is consistent with an expected S-wave observation (Fig. 21).

The phase pair of x1 and x2 again suggests two separate events. Unlike S0809a, the first event is weaker in the S0820a case. MQS followed the same procedure as S0809a, and catalogued a single event using the most apparent P- and S-phases. The signal-to-ratios for S0820a are 47.6 for both SNR_S (fifth largest in the catalogue) and SNR_P. The event does not have an SNR_W since the wind sensors were not functional at the time.

6.1.3. S0864a-BB quality A

S0864a occurred in the early morning (origin time 2021-05-02 00:57:35 UTC, 01:01 LMST), during mild windy conditions (Fig. 22). The event has energy between 0.125 and 2.4 Hz; hence it is classified as broadband. The event duration is $\sim$18 minutes.

MQS identified a P- (± 10 s) and an S-phase (± 5 s). Using these phases, the distance is obtained as $28.7 \pm 3.5^\circ$. The P-wave train is clearly visible in the time-domain, which points to a backazimuth of 97° (-14°, $+19^\circ$) (Fig. 23), which is further confirmed by the wavelet transform analysis

(Fig. 24). Similar to a vast majority of the events in the MQS catalogue, the event is located in the vicinity of the Cerberus Fossae region.

MQS also identified an additional phase in the S-wave coda. The arrival is clear in the time domain. MQS labelled the phase as x1 with a picking uncertainty of ±5 s. Further, the event shows a high-frequency arrival around 2.4 Hz, which is labelled as y1 (±5 s) (Fig. 25).

The event has a magnitude of $M_W^{Ma}3.1\pm0.2$. The SNRs are $SNR_S7.3$ and $SNR_P455.6$, the highest SNR value in the catalogue calculated from pressure data.

6.1.4. S0976a-LF quality A: the most distant event

The event on sol 976 (origin time 2021-08-25 03:32:20 UTC, ∼02:20 LMST) is an LF event with energy dominantly between 1–8 s period (Figs. 26 and 27). The event duration is roughly 1 hour. Another very significant event, S0976b (VF QB), occurred later in the sol, and is described later.

This event shows two clear arrivals with a differential travel time of ∼840 s, which appear to be vertically and horizontally inclined respectively (Fig. 28), suggestive of P and S-wave energy. However, according to the current understanding of the Martian interior (Durán et al., 2022; Khan et al., 2021; Stähler et al., 2021b), the maximum difference between the direct P and S phases can be ∼600 s (Fig. 9). Therefore, MQS labelled the identified phases as PP and SS (mantle body-wave phases that reflect at the planet's surface once), with uncertainties of ±10 s.

MQS locates S0976a at the Valles Marineris region, with a distance of $146°(\pm7°)$ and a backazimuth of $101°(-30°, 20°)$ (Fig. 29). The location estimate is relatively reliable, therefore the event is assigned quality A.

S0976a is the furthest event in the MQS catalogue. Although it is not the

largest amplitude ($1.46 \times 10{-}9\ m/s$ around the SS pick; bandpass 2-5 s.), it has the largest moment magnitude of $M_W^{Ma}4.2{\pm}0.3$ due to its distance. The event occurred in the early morning hours when the seismic background noise was relatively high; the seismic energy has an SNR_S31 and SNR_P34. Furthermore, the 25 s monochromatic anomaly (Fig.5) is dominant in the pre-event noise and during the start of the event. However, the artefact does not affect the analysis as the energy content of the event is focused at higher frequencies. The pressure sensors were recording during the event, and the data shows nothing anomalous (Fig. 26d).

6.1.5. S0784a-BB quality B

The event on sol 784 (origin time 2021-02-09 12:11:32 UTC, ∼17:16 LMST) is a relatively high amplitude event ($7 \times 10{-}10\ m/s$ around the S pick using a bandpass between 2-5 s.) with a duration of ∼30 minutes (Fig. 30). This event is the first marsquake observed after the long period of non-detection during the Martian winter. The equivalent sol in the first year is 116, and so is very similar time of year to the first LF family event observed on sol 105.

MQS was able to identify a P-wave arrival (±10 s) in the time domain and with the aid of the spectrograms. It is not possible to reliably obtain a backazimuth using the P-wave. The S-phase pick (±5 s) is clear in the time domain, and free of glitch contamination.

The event shows energy between 0.2 and ∼2.4 Hz; hence classified as a BB (Fig. 31). MQS identified the beginning of the energy arrival at 2.4 Hz with a y1 pick (±10 s) 15 s after the P-arrival.

The event occurred in the afternoon, right after the noisy period of the sol that is dominated by heavy winds. The seismic energy has an SNR_S

of 21 and SNR_P of 32. Due to the ongoing winds, the lander modes are partially activated coinciding with the event. The energy is dominated by continuous contamination from the wind noise below 5 s.

Using the S-P travel time, we compute an event distance of 34.5°(±3.5). The aligned distance for S0784a is 32.1°. The event magnitude is calculated as $\mathrm{M}_{\mathrm{W}}^{\mathrm{Ma}} 3.3 \pm 0.2$.

6.1.6. S0802a-BB quality B

S0802a (origin time 2021-02-28 06:07:21 UTC, ∼23:09 LMST) occurred in the late evening period, in between two weak wind gusts, though the waveforms are relatively clean (Fig. 32). The energy is visible between ∼0.125–2.4 Hz. The P-wave coda is free of glitch contamination; however, there are several large amplitude glitches in the S-wave train (Fig. 33). The seismic energy has SNR_S of 9 and SNR_P of 11.

MQS was able to identify clear P(±2 s) and S(±10 s) phases. With these picks, the MQS distance from inversions is calculated as $30 \pm 3.5°$. The aligned distance for S0802a is 29.9°. The event magnitude obtained using the MQS distance is $\mathrm{M}_{\mathrm{W}}^{\mathrm{Ma}} 2.9 \pm 0.2$.

Although the P-wave energy is clear in the time domain, it was not possible to obtain a robust backazimuth. Similar to the two QA events described above (S0809a and S0820a), this event shows a clear intermediate phase arrival ∼1 m after the direct P-phase. The phase is labelled as x1 and pick uncertainties are assigned as ±20 s. Furthermore, a y1 phase (±5 s) is identified from excitation of the 2.4 Hz resonance about 5-s after the P. However, the STA/LTA envelopes do not show clear slope breaks that would allow for a y2 phase pick. The event duration is ∼12 min.

6.1.7. S0899d-LF quality B

S0899d (origin time 2021-06-07 20:07:39 UTC, 21:12 LMST) has energy between ∼1–8 s (Fig. 34). It occurred during a relatively quiet time of the evening period. The seismic energy has an SNR_S of 10, and a duration of 11 minutes.

The most striking characteristic of this event is that it exhibits only one impulsive phase arrival, which MQS has labelled as x1 with an uncertainty of ±10 s. The phase has linear polarization with strong vertical inclination, suggesting a P-wave, that has a backazimuth of 25° (-14, +12°) (Fig. 35). Since there is no convincing indication of a secondary phase, it is not possible to compute an event distance.

S0899d is not the only event with a clear backazimuth but only a poorly determined or missing distance estimate. Another early event, S0183a (LF, QB), also includes an impulsive single arrival. MQS was able to pick a weak secondary phase and located S0183a at 46°. Following the envelope similarity and alignment procedure, S0899d might also be coming from a similar distance. Since it is not possible to compute the event distance, S0899d is marked with an equidistant curve at 46° in Fig. 2.

6.1.8. S1000a-BB quality B

S1000a is the second most distant event after S0976a in the V9 catalogue. Horleston et al. (2022) provides a more detailed report on these two special events.

The event occurred on 2021-09-18 17:48:00 UTC (00:48:25 LMST) with strong energy between ∼0.1–5 Hz (Figs. 36 and 37). MQS located the event at 116°($^{\pm}$9°). This distance was obtained using PP, SS, and a first observation of Pdiff (diffracted P-wave at the core-mantle boundary. The distance

for S1000a using PP and SS phases only is 128±19°. Although, the P-wave velocities below ∼800 km are not well constrained (Khan et al., 2021) and inclusion of the Pdiff phase leads to unrealistically narrow uncertainties, the first origin is the preferred one in the catalogue V9.

Both the PP and SS phases are emergent and complicated. Therefore MQS assigned wide uncertainties for the picks as ±20 s and ±60 s, respectively. The Pdiff phase is more clear, and picked with an uncertainty of ±10 s. It was not possible to obtain a robust backazimuth estimate. Due to its wide frequency range of energy above 2.4 Hz and lack of backazimuth based on the PP arrival, the event is classified as a BB quality B.

Another BB event (S1000b, QC) occurred 81 minutes after S1000a. Although the second event is much weaker and it appears to have a different frequency content, it could be interpreted as a potential aftershock. Alternatively, it could be a very rare case on Mars of a closely spaced but independent event. S1000b is weakly visible in Fig. 37) at about 4850 s.

6.2. HF family

Like the LF family events, the activity of HF events during the first year of observation showed a clear time dependency, with activity effectively ceasing for over 200 sols, beginning shortly after sol 500 until sol 713. During these autumn / winter seasons with of strong, persistent winds, only large VF events and a few QD 2.4 Hz were observed. Knapmeyer et al. (2021), focusing on the HF event type only, compared the observed event times of the first year with several seasonally variable external driving forces and concluded that the HF activity follows an annual cycle, even after taking the change in noise into account. They predicted that vigorous HF event activity would commence between sol 850 and sol 900.

Fig. 38 shows the occurrence times of HF events in years one and two, up to sol 1011. As in year one, detection efficiency (a measure for how likely events of a certain amplitude are detected, introduced by Knapmeyer et al. (2021)) attained high values while only a few events were detected. As predicted, the event rate started increasing in spring, after sol 850 and under essentially constant detection efficiency. The event rate in the second year appears to be higher than in the first year, but a concluding assessment will be possible only after the predicted cease around sol 1200.

A comparison of all VF, HF and 2.4 Hz events that were reported in V3 and V9 catalogues are shown in Fig. 39, following van Driel et al. (2021). The VF events recorded after sol 478 include the 4 largest events, all at distances between 17-20°, as well as the 3 closest events to the lander - each of these events includes a chirp signal in the coda and are described below.

Fig 7, also following van Driel et al. (2021), presents the alignments for the quality B VF, HF and 2.4 Hz events in V9, showing the consistent moveout in 2.4 Hz envelope shapes. The amplitude-distance range (Fig.39) for the HF and 2.4 H event types is not substantially different compared to the first martian year.

Kernel density estimations (KDE) for the VF for the 2.4 Hz and HF events are basically unchanged, clustering tightly at a distance between 15-30°, though the VF events continue occur across a much broader distance range, now with a larger density closer to the lander.

By definition, HF type events show energy predominantly at 2.4 Hz and above. However, some strong HF events show relatively weak energy below 2.4 Hz down to ∼4–5 s. This class of HF events became more evident as the catalogue evolved in the second Martian year. We show an example from early in the mission from sol 260 (S0260a, HF QB) in Fig. 40.

Below, we describe the most remarkable HF family events that occurred between sol 478 (Clinton et al., 2021) and sol 1011 (InSight Marsquake Service, 2022), including those with chirp-like signals in the S–wave coda. All events described are type VF. The HF and 2.4 Hz events observed in this second year remain similar to those initially presented in (Clinton et al., 2021), with similar amplitudes, distance and frequency content.

6.2.1. VF events with chirps: S0533a (QC), S0793a (QB), S0981c (QB), S0986c (QB)

On sol 981 at ∼22:55 LMST (2021-08-31 03:59 UTC), MQS detected a quality B VF event, S0981c, with strong Pg (±2 s) and Sg (±10 s) phases (Fig. 41). The event is clearly visible both in time domain and spectrograms although it occurred during the evening with mild winds. The event is one of the closest events, with a Pg-Sg derived distance of ∼3.5°, roughly 200 km from the InSight lander.

What made S0981c an exceptional event was not only its high-quality seismic phases and close distance, but also that the event waveforms include a vertically polarised, dispersive chirp-like signal in the S-wave coda approximately 15 minutes after the Sg pick just before the energy terminates. MQS labelled this arrival as an x1 phase with ±5 s uncertainty. The chirp signal is visible on the event spectrograms at 2 Hz and continues down to approximately 8 s until the amplitudes fall below the background noise level.

Only 5 days afterwards, another VF event, S0986c, was observed, that included multiple even stronger chirp signals (Fig. 42). Upon further investigation, similar but weaker chirps were identified in two more events (S0533a and S0793a).

S0986c (origin time 2021-09-05 05:18:58 UTC, 21:15 LMST) is the most

unique event among the four events with chirps (Fig. 42): 3 successive chirp signals are identified, with increasing amplitudes and dispersion. MQS picked clear Pg(±2 s) and Sg(±5 s) phases, which locate the event at 1.2 ° away from InSight, the closest distance reported thus far. The event has very clear energy from 0.5 Hz up to 20 Hz with a duration of 12 minutes. The magnitude is computed as $M_W^{Ma} 1.2 \pm 0.2$. The first chirp is visible ∼2 m45 s after the Pg arrival and does not show dispersive character. The second and third chirps are identified approximately 1 minute apart from each other, following the first packet of energy with more evident dispersive characteristics. These chirps are labelled as x1–x3 in the V9 catalogue.

S0986c has initial energy arrivals (Pg and Sg) at around 5 Hz. There is also another distinct energy arrival at 2.4 Hz after the Sg pick, which MQS labelled as y1 phase.

6.2.2. The largest VF event: S0976b, quality B

Sol 976 was a momentous day for InSight with the key events. S0976a (LF QA), the largest and most distant event recorded so far, occurred in the early morning. S0976b (VF QB), the largest magnitude event from the HF family, was observed only hours later in the afternoon during heavy winds.

S0976b (origin time 2021-08-25 16:51:30 UTC) begins at ∼15:21 LMST (Fig. 43) and lasts for ∼18 minutes. Due to the ambient noise conditions, event energy is observed up to ∼20 Hz but not above this, unlike some other strong VF events at similar distances. The Sg phase has significant lower frequency energy out to several seconds period (Fig. 43b and c). There are no significant glitches during the event (typical for this time of day), and it has an SNR_S of 9.4.

The MQS identified the Pg phase in the time domain with a ±5 s uncer-

tainty. Energy appears to arrive at 2.4 Hz just prior to higher frequencies. The Sg phase is identified with ±10 s uncertainty using the time domain and the 2.4 Hz and VF STA/LTA filters. The distance is calculated to be ∼15.7°. The magnitude is $M_W^{Ma}4.1 \pm 0.2$, making it the largest VF event recorded so far, by a full magnitude unit (Fig. 12).

6.2.3. The most distant VF event: S0923d, quality C

The most distant VF event in the catalogue to date is S0923d (origin time 2021-07-02 12:08:31 LMST, ∼21:30 LMST) at a distance of ∼41.4°. This event is complicated by the apparent arrival of three separate energy packets. The event contains energy from ∼0.25-8 Hz, the lowest frequency energy being in the latest arrival (Fig. 44).

The event is relatively weak and occurred during a mild wind gust. Therefore, the waveforms are possibly highly contaminated and the event is assigned a quality value of C. MQS has catalogued the three energy packets as y1 (±60 s), Pg (±20 s) and Sg (±60 s). The magnitude is calculated to be $M_W^{Ma}2.1 \pm 0.2$.

6.2.4. S0734a-VF quality B

S0734a (origin time 2020-12-19 10:12:02), like S0756a occurs early on a Martian winter morning at ∼00:45 LMST with an SNR_S of 6.3. Again this event shows a very broad range of frequencies with energy extending up to ∼30 Hz. Unlike S0756 there is limited energy below ∼1 Hz. Despite the early morning winds the event onset is clear in the time domain and Pg is picked with ±1 s uncertainty, Sg with ±5 s. There is very little glitch contamination. The event distance is ∼8.3° and the magnitude is $M_W^{Ma}2.5 \pm 0.2$.

6.2.5. S0756a-VF quality B

Sol 756 is also in the late winter on Mars but S0756a is a very strong VF event and is clearly visible in the daily spectrogram with origin time 2021-01-11 01:07 UTC, ∼01:11 LMST. Although the SNR_S is only 6.6 this is a very clear event with strong energy across a broad frequency range, extending from ∼0.4 - 30 Hz. This is also a relatively long duration event within the HF family lasting ∼24 minutes.

The event onset is sharp and Pg was picked with a ±1 s uncertainty in the time domain. Sg is more complicated and was picked using the 2.4 Hz STA/LTA with ±20 s uncertainty. The event distance is calculated to be ∼19.1° and the magnitude is $\mathrm{M}_{\mathrm{W}}^{\mathrm{Ma}} 2.8 \pm 0.2$ (joint 4^{th} largest VF event).

6.2.6. S0794a-VF quality B

S0794a (origin time 2021-02-19 01:22:11 UTC) occurred at ∼00:22 LMST and is the second strongest VF event catalogued to date after S0976b. It stands out in the daily spectrogram during light early morning winds with an SNR_S of 8.6. Energy is observed from 0.5-30 Hz making it one of the most broad spectrum events so far.

Energy arrives very slightly earlier at 2.4 Hz than at high frequencies, so the Pg was picked using the 2.4 Hz STA/LTA with an uncertainty of ±5 s. The onset of the Sg phase is more prominent at higher frequencies and so was picked using the VF STA/LTA (7-9 Hz) with a ±10 s uncertainty. The event distance is ∼17.6° and the magnitude is $\mathrm{M}_{\mathrm{W}}^{\mathrm{Ma}} 3.1 \pm 0.2$. For comparison, the only larger VF event, S0796b, has magnitude $\mathrm{M}_{\mathrm{W}}^{\mathrm{Ma}} 4.1 \pm 0.2$.

6.3. SF family

The short duration, super high frequency (SF) events are interpreted to have very local sources around the lander, resulting from the thermal con-

traction on the planet's surface due to daily temperature variations (Dahmen et al., 2021a).

The temporal distribution of SF events in V9 and their seasonal characteristic are shown in Fig. 45. In the first Martian year, the high-amplitude SF events were primarily observed during three distinct periods: the first and largest cluster occurred between sols 190–300 starting at 2 hours before the sunset (16:00–18:00 LMST). After that, we see the events forming more linear patterns starting around sol 350, and around sol 460, until the background noise exceeded the detection threshold. As we enter the second Martian year, we observe the first cluster of SF events again (sols 850–950) around sunset, and similar to the first year, the events started to occur after some period of lack of high-amplitude SF events. Remarkably, the event clusters in Martian years 1 and 2 have nearly identical waveforms on the horizontal components, as shown in Fig. 46 for two SF events that are 670 sols (approximately one Martian) year apart.

7. Catalogue and data access

The first public release of the catalogue was on 2020-01-02, covering the events until InSight sol 299 (2019-09-30) (InSight Marsquake Service, 2020a). Clinton et al. (2021) is the first study that comprehensively describes the catalogue, summarising seismicity included in the third catalogue update up to sol 478 (2020-03-31) (InSight Marsquake Service, 2020b). All InSight catalogue versions are available from several resources in QuakeML XML format. MQS produces the catalogues in an extended Mars version as well as with standard basic event description similar to Earth seismic networks.

The official data release end point is the web services provided by the In-

Sight SEIS data portal (InSight Mars SEIS Data Service, 2019a), which also provides links to each catalogue version (https://www.seis-insight.eu/en/science/seis-products/mqs-catalogs). The same resources are archived at the NASA Planetary Data System servers (InSight Mars SEIS Data Service, 2019b).

Additionally, IRIS (Incorporated Research Institutions for Seismology) distributes the catalogues at a Mars InSight events node (http://ds.iris.edu/ds/nodes/dmc/tools/mars-events/). The IRIS tool also provides a simple searchable table for quick and easy access to the event based information.

8. Conclusions

InSight's nominal mission duration was one Martian year, equivalent to roughly two Earth years. The mission has been extended into a second Martian year, and SEIS is still performing exceptionally well after more than 1000 sols on the red planet. Unfortunately, InSight has been facing power issues with dust accumulating on the solar panels that threaten the long term viability of the lander and have resulted in significant reduction of scientific instrument collection. Only the VBB continues to be always on, and are now collecting continuous data at 100 sps.

After 1011 sols on Mars, MQS identified a total of 951 traditional quakes (69 LF, 882 HF), and 1062 SF events which are interpreted to be thermally driven. The V9 catalogue includes two sets of events that were not observed in the first Martian year: First, unlike the vast majority of LF family quakes, the seismometers recorded two of the most distant events so far (S0976a and S1000a). S0976a has been located in the Valles Marineris region $146^\circ \pm 7^\circ$ away from the InSight. The distance for S1000a is determined as $116^\circ \pm 9^\circ$; however, MQS could not obtain a reliable backazimuth (Horleston et al.,

2022). Second, four VF events (S0533a, S0793a, S0981c, S0986c) show associated chirp signals. The largest VF event since the landing (S0976b, $M_W^{Ma}4.1\pm0.2$) is also included in this catalogue version.

The seismicity of the second Martian year has confirmed that the bulk of tectonic activity on InSight's hemisphere of the planet takes place in a relatively limited area, between 25 and 35°epicentral distance and due east. The most likely tectonic source is the Cerberus Fossae graben system (Perrin et al., 2022). The distance distribution of the majority of HF events (20-32°) allows the interpretation that they might also occur there, yet, without backazimuths, this cannot be proven. Their seasonality, that was already hinted at in the first Martian year (Knapmeyer et al., 2021), has been confirmed in the second year, together with an apparent increase in their rate. The VF events are still enigmatic, pretty much equidistributed between 0 and 40°. They could therefore be considered as the most likely candidates for impact events.

Dahmen et al. (2021a) analysed the SF events and concluded that their occurrence is most probably thermally driven and seasonal. In the second Martian year, the patterns that SF events demonstrate are very similar to those observed in the first year with distinct clustering around the sunset (Fig. 45), confirming the findings of Dahmen et al. (2021a).

Since the publication of the last catalogue review (Clinton et al., 2021), the interior of the planet has been much better constrained seismically using additional body wave phases (PP, SS, ScS), which is now reflected in the MQS catalogue locations. The next year will bring more detailed studies on this, as well as tectonic interpretations on the source contexts, which will be reflected in the next catalogue review paper.

The seismicity catalogue is available to the InSight team in near real-

time. The catalogue is made publicly available every three months with a three-month delay alongside the seismic waveform data. All versions of the MQS catalogue contain the events for the whole mission duration at the time of release.

After the likely end of the mission, a final MQS catalogue with a companion paper will reflect the understanding of the InSight science team after more than three years of operation and analysis on the surface of the red planet.

References

W. B. Banerdt, S. E. Smrekar, D. Banfield, D. Giardini, M. Golombek, C. L. Johnson, P. Lognonné, A. Spiga, T. Spohn, C. Perrin, S. C. Stähler, D. Antonangeli, S. Asmar, C. Beghein, N. Bowles, E. Bozdag, P. Chi, U. Christensen, J. Clinton, G. S. Collins, I. Daubar, V. Dehant, M. Drilleau, M. Fillingim, W. Folkner, R. F. Garcia, J. Garvin, J. Grant, M. Grott, J. Grygorczuk, T. Hudson, J. C. E. Irving, G. Kargl, T. Kawamura, S. Kedar, S. King, B. Knapmeyer-Endrun, M. Knapmeyer, M. Lemmon, R. Lorenz, J. N. Maki, L. Margerin, S. M. McLennan, C. Michaut, D. Mimoun, A. Mittelholz, A. Mocquet, P. Morgan, N. T. Mueller, N. Murdoch, S. Nagihara, C. Newman, F. Nimmo, M. Panning, W. T. Pike, A.-C. Plesa, S. Rodriguez, J. A. Rodriguez-Manfredi, C. T. Russell, N. Schmerr, M. Siegler, S. Stanley, E. Stutzmann, N. Teanby, J. Tromp, M. van Driel, N. Warner, R. Weber, and M. Wieczorek. Initial results from the InSight mission on Mars. *Nat. Geosci.*, 13(3):183–189, 2020. ISSN 1752-0894. doi: 10.1038/s41561-020-0544-y.

D. Banfield, J. A. Rodriguez-Manfredi, C. T. Russell, K. M. Rowe, D. Leneman, H. R. Lai, P. R. Cruce, J. D. Means, C. L. Johnson, A. Mittelholz, S. P. Joy, P. J. Chi, I. G. Mikellides, S. Carpenter, S. Navarro, E. Sebastian, J. Gomez-Elvira, J. Torres, L. Mora, V. Peinado, A. Lepinette, K. Hurst, P. Lognonné, S. E. Smrekar, and W. B. Banerdt. InSight Auxiliary Payload Sensor Suite (APSS). *Space Sci. Rev.*, 215(1):4, 2019. doi: 10.1007/s11214-018-0570-x.

M. Böse, J. F. Clinton, S. Ceylan, F. Euchner, M. van Driel, A. Khan, D. Giardini, P. Lognonné, and W. B. Banerdt. A probabilistic framework for single-station location of seismicity on Earth

and Mars. *Phys. Earth Planet. Inter*, 262:48–65, 2017. doi: https://doi.org/10.1016/j.pepi.2016.11.003.

M. Böse, D. Giardini, S. Stähler, S. Ceylan, J. F. Clinton, M. van Driel, A. Khan, F. Euchner, P. Lognonné, and W. B. Banerdt. Magnitude Scales for Marsquakes. *Bull. Seismol. Soc. Am.*, 108(5A):2764–2777, 2018. ISSN 0037-1106. doi: https://doi.org/10.1785/0120180037.

M. Böse, S. C. Stähler, N. Deichmann, D. Giardini, J. Clinton, P. Lognonné, S. Ceylan, M. van Driel, C. Charalambous, N. Dahmen, A. Horleston, T. Kawamura, A. Khan, M. Knapmeyer, G. Orhand-Mainsant, J. Scholz, F. Euchner, and W. B. Banerdt. Magnitude scales for marsquakes calibrated from insight data. *Bull. Seismol. Soc. Am.*, Jun 2021. ISSN 0037-1106. doi: 10.1785/0120210045.

N. Brinkman, S. C. Stähler, D. Giardini, C. Schmelzbach, A. Khan, A. Jacob, N. Fuji, C. Perrin, P. Lognonné, E. Beucler, M. Böse, S. Ceylan, C. Charalambous, J. F. Clinton, M. van Driel, F. Euchner, A. Horleston, T. Kawamura, B. Knapmeyer-Endrun, G. Mainsant, M. P. Panning, W. T. Pike, J.-R. Scholz, J. O. A. Robertsson, and W. B. Banerdt. First focal mechanisms of marsquakes. *J. Geophys. Res.: Planets*, 126(4): e2020JE006546, 2021. doi: https://doi.org/10.1029/2020JE006546.

S. Ceylan, M. van Driel, F. Euchner, A. Khan, J. Clinton, L. Krischer, M. Böse, S. Stähler, and D. Giardini. From Initial Models of Seismicity, Structure and Noise to Synthetic Seismograms for Mars. *Space Sci. Rev.*, 211(1-4), 2017. doi: 10.1007/s11214-017-0380-6.

S. Ceylan, J. F. Clinton, D. Giardini, M. Böse, C. Charalambous, M. van Driel, A. Horleston, T. Kawamura, A. Khan, G. Orhand-Mainsant, J.-

R. Scholz, S. C. Stähler, F. Euchner, W. B. Banerdt, P. Lognonné, D. Banfield, E. Beucler, R. F. Garcia, S. Kedar, M. P. Panning, W. T. Pike, S. E. Smrekar, A. Spiga, N. L. Dahmen, K. Hurst, A. E. Stott, R. D. Lorenz, M. Schimmel, E. Stutzmann, J. ten Pierick, V. Conejero, C. Pardo, and C. Perrin. Companion guide to the marsquake catalog from InSight, Sols 0–478: Data content and non-seismic events. *Phys. Earth Planet. Inter.*, 310:106597, 2021. ISSN 0031-9201. doi: https://doi.org/10.1016/j.pepi.2020.106597.

C. Charalambous, A. E. Stott, W. T. Pike, J. B. McClean, T. Warren, A. Spiga, D. Banfield, R. F. Garcia, J. Clinton, S. Stähler, S. Navarro, P. Lognonné, J.-R. Scholz, T. Kawamura, M. van Driel, M. Böse, S. Ceylan, A. Khan, A. Horleston, G. Orhand-Mainsant, L. M. Sotomayor, N. Murdoch, D. Giardini, and W. B. Banerdt. A comodulation analysis of atmospheric energy injection into the ground motion at insight, mars. *J. Geophys. Res.: Planets*, 126(4):e2020JE006538, 2021. doi: https://doi.org/10.1029/2020JE006538.

J. Clinton, D. Giardini, M. Böse, S. Ceylan, M. van Driel, F. Euchner, R. F. Garcia, S. Kedar, A. Khan, S. C. Stähler, B. Banerdt, P. Lognonne, E. Beucler, I. Daubar, M. Drilleau, M. Golombek, T. Kawamura, M. Knapmeyer, B. Knapmeyer-Endrun, D. Mimoun, A. Mocquet, M. Panning, C. Perrin, and N. A. Teanby. The Marsquake Service: Securing Daily Analysis of SEIS Data and Building the Martian Seismicity Catalogue for InSight. *Space Sci. Rev.*, 214:133, 2018. doi: 10.1007/s11214-018-0567-5.

J. F. Clinton, S. Ceylan, M. van Driel, D. Giardini, S. C. Stähler,

M. Böse, C. Charalambous, N. L. Dahmen, A. Horleston, T. Kawamura, A. Khan, G. Orhand-Mainsant, J.-R. Scholz, F. Euchner, W. B. Banerdt, P. Lognonné, D. Banfield, E. Beucler, R. F. Garcia, S. Kedar, M. P. Panning, C. Perrin, W. T. Pike, S. E. Smrekar, A. Spiga, and A. E. Stott. The marsquake catalogue from insight, sols 0–478. *Phys. Earth Planet. Inter.*, 310:106595, 2021. ISSN 0031-9201. doi: https://doi.org/10.1016/j.pepi.2020.106595.

N. L. Dahmen, J. F. Clinton, S. Ceylan, M. van Driel, D. Giardini, A. Khan, S. C. Stähler, M. Böse, C. Charalambous, A. Horleston, T. Kawamura, G. Orhand-Mainsant, J.-R. Scholz, F. Euchner, W. T. Pike, R. C. Weber, P. Lognonné, and W. B. Banerdt. Super High Frequency Events: A New Class of Events Recorded by the InSight Seismometers on Mars. *J. Geophys. Res.: Planets*, 126(2):e2020JE006599, 2021a. doi: https://doi.org/10.1029/2020JE006599.

N. L. Dahmen, G. Zenhäusern, J. F. Clinton, D. Giardini, S. C. Stähler, S. Ceylan, C. Charalambous, M. van Driel, K. J. Hurst, S. Kedar, P. Lognonné, N. Murdoch, R. Myhill, M. P. Panning, W. T. Pike, M. Schimmel, C. Schmelzbach, J. Scholz, A. E. Stott, E. Stutzmann, and W. B. Banerdt. Resonances and Lander Modes Observed by InSight on Mars (1–9 Hz). *Bull. Seismol. Soc. Am.*, 111(6):2924–2950, 10 2021b. doi: 10.1785/0120210056.

C. Durán, A. Khan, S. Ceylan, G. Zenhäusern, S. Stähler, J. Clinton, and D. Giardini. Seismology on mars: An analysis of direct, reflected, and converted seismic body waves with implications for interior struc-

ture. *Phys. Earth Planet. Inter.*, 325:106851, 2022. ISSN 0031-9201. doi: https://doi.org/10.1016/j.pepi.2022.106851.

D. Giardini, P. Lognonné, W. B. Banerdt, W. T. Pike, U. Christensen, S. Ceylan, J. F. Clinton, M. van Driel, S. Stähler, M. Böse, R. F. Garcia, A. Khan, M. Panning, C. Perrin, D. Banfield, E. Beucler, C. Charalambous, F. Euchner, A. Horleston, A. Jacob, T. Kawamura, S. Kedar, G. Orhand-Mainsant, J.-R. Scholz, S. Smrekar, A. Spiga, C. Agard, D. Antonangeli, S. Barkaoui, E. Barrett, P. Combes, V. Conejero, I. Daubar, M. Drilleau, C. Ferrier, T. Gabsi, T. Gudkova, K. Hurst, F. Karakostas, S. King, M. Knapmeyer, B. Knapmeyer-Endrun, R. Llorca-Cejudo, A. Lucas, L. Luno, L. Margerin, J. McClean, D. Mimoun, N. Murdoch, F. Nimmo, M. Nonon, C. Pardo, A. Rivoldini, J. A. Rodriguez Manfredi, H. Samuel, M. Schimmel, A. E. Stott, E. Stutzman, N. Teanby, T. Warren, R. Weber, M. Wieczorek, and C. Yana. The Seismicity of Mars. *Nat. Geosci.*, 2020. doi: 10.1038/s41561-020-0539-8.

C. R. Harris, K. J. Millman, S. J. van der Walt, R. Gommers, P. Virtanen, D. Cournapeau, E. Wieser, J. Taylor, S. Berg, N. J. Smith, R. Kern, M. Picus, S. Hoyer, M. H. van Kerkwijk, M. Brett, A. Haldane, J. F. del Río, M. Wiebe, P. Peterson, P. Gérard-Marchant, K. Sheppard, T. Reddy, W. Weckesser, H. Abbasi, C. Gohlke, and T. E. Oliphant. Array programming with NumPy. *Nature*, 585(7825):357–362, Sept. 2020. doi: 10.1038/s41586-020-2649-2.

M. Hobiger, M. Hallo, C. Schmelzbach, S. C. Stähler, D. Fäh, D. Giardini, M. Golombek, J. Clinton, N. Dahmen, G. Zenhäusern, B. Knapmeyer-Endrun, S. Carrasco, C. Charalambous, K. Hurst, S. Kedar, and W. B.

Banerdt. The shallow structure of mars at the insight landing site from inversion of ambient vibrations. *Nature Communications*, 12(1):6756, Nov 2021. doi: 10.1038/s41467-021-26957-7.

A. Horleston, J. Clinton, S. Ceylan, D. Giardini, C. Charalambous, J. Irving, P. Lognonné, S. C. Stähler, G. Zenhäusern, N. Dahmen, C. Duran, T. Kawamura, A. Khan, D. Kim, M. Plasman, F. Euchner, C. Beghein, E. Beucler, Q. Huang, M. Knapmeyer, B. Knapmeyer-Endrun, V. Lekić, J. Li, C. Perrin, M. Schimmel, N. Schmerr, A. Stott, E. Stutzmann, N. Teanby, Z. Xu, M. Panning, and W. Banerdt. The far side of Mars: two distant marsquakes detected by InSight. *The Seismic Record*, 2022. doi: 10.1785/0320220007.

J. D. Hunter. Matplotlib: A 2D graphics environment. *Comput. Sci. Eng.*, 9(3):90–95, 2007. doi: 10.1109/MCSE.2007.55.

InSight Mars SEIS Data Service. SEIS raw data, Insight Mission. IPGP, JPL, CNES, ETHZ, ICL, MPS, ISAE-Supaero, LPG, MFSC, 2019a.

InSight Mars SEIS Data Service. InSight SEIS Data Bundle. PDS Geosciences (GEO) Node, 2019b.

InSight Marsquake Service. Mars Seismic Catalogue, InSight Mission; V1 2/1/2020. ETHZ, IPGP, JPL, ICL, ISAE-Supaero, MPS, Univ Bristol. Dataset, 2020a.

InSight Marsquake Service. Mars Seismic Catalogue, InSight Mission; V3 2020-07-01. ETHZ, IPGP, JPL, ICL, ISAE-Supaero, MPS, Univ Bristol. Dataset, 2020b.

InSight Marsquake Service. Mars Seismic Catalogue, InSight Mission; V5 2021-01-04. ETHZ, IPGP, JPL, ICL, ISAE-Supaero, MPS, Univ Bristol. Dataset, 2021a.

InSight Marsquake Service. Mars seismic catalogue, insight mission; v8 2021-10-01, 2021b. URL `https://www.insight.ethz.ch/seismicity/catalog/v8`.

InSight Marsquake Service. Mars Seismic Catalogue, InSight Mission; V9 2022-01-01, 2022. URL `https://www.insight.ethz.ch/seismicity/catalog/v9`.

S. Kedar, M. P. Panning, S. E. Smrekar, S. C. Stähler, S. D. King, M. P. Golombek, M. Manga, B. R. Julian, B. Shiro, C. Perrin, J. A. Power, C. Michaut, S. Ceylan, D. Giardini, P. H. Lognonné, and W. B. Banerdt. Analyzing low frequency seismic events at cerberus fossae as long period volcanic quakes. *J. Geophys. Res.: Planets*, 126(4):e2020JE006518, 2021. doi: https://doi.org/10.1029/2020JE006518.

B. L. Kennett and E. R. Engdahl. Traveltimes for global earthquake location and phase identification. *Geophys. J. Int.*, 105(2):429–465, 1991. doi: 10.1111/j.1365-246X.1991.tb06724.x.

A. Khan, M. van Driel, M. Böse, D. Giardini, S. Ceylan, J. Yan, J. Clinton, F. Euchner, P. Lognonné, N. Murdoch, D. Mimoun, M. Panning, M. Knapmeyer, and W. B. Banerdt. Single-station and single-event marsquake location and inversion for structure using synthetic Martian waveforms. *Phys. Earth Planet. Inter*, 258:28–42, 2016. doi: https://doi.org/10.1016/j.pepi.2016.05.017.

A. Khan, C. Liebske, A. Rozel, A. Rivoldini, F. Nimmo, J. A. D. Connolly, A.-C. Plesa, and D. Giardini. A Geophysical Perspective on the Bulk Composition of Mars. *J. Geophys. Res.: Planets*, 123(2):1–37, Feb. 2018. ISSN 2169-9100. doi: 10.1002/2017JE005371.

A. Khan, S. Ceylan, M. van Driel, D. Giardini, P. Lognonné, H. Samuel, N. C. Schmerr, S. C. Stähler, A. C. Duran, Q. Huang, D. Kim, A. Broquet, C. Charalambous, J. F. Clinton, P. M. Davis, M. Drilleau, F. Karakostas, V. Lekic, S. M. McLennan, R. R. Maguire, C. Michaut, M. P. Panning, W. T. Pike, B. Pinot, M. Plasman, J.-R. Scholz, R. Widmer-Schnidrig, T. Spohn, S. E. Smrekar, and W. B. Banerdt. Upper mantle structure of Mars from InSight seismic data. *Science*, 373(6553):434–438, 2021. doi: 10.1126/science.abf2966.

D. Kim, P. Davis, V. Lekić, R. Maguire, N. Compaire, M. Schimmel, E. Stutzmann, J. C. E. Irving, P. Lognonné, J. Scholz, J. Clinton, G. Zenhäusern, N. Dahmen, S. Deng, A. Levander, M. P. Panning, R. F. Garcia, D. Giardini, K. Hurst, B. Knapmeyer-Endrun, F. Nimmo, W. T. Pike, L. Pou, N. Schmerr, S. C. Stähler, B. Tauzin, R. Widmer-Schnidrig, and W. B. Banerdt. Potential Pitfalls in the Analysis and Structural Interpretation of Seismic Data from the Mars InSight Mission. *Bull. Seismol. Soc. Am.*, 111(6):2982–3002, 10 2021. ISSN 0037-1106. doi: 10.1785/0120210123.

M. Knapmeyer, J. Oberst, E. Hauber, M. Wählisch, C. Deuchler, and R. Wagner. Working models for spatial distribution and level of mars' seismicity. *J. Geophys. Res.: Planets*, 111(E11), 2006. doi: https://doi.org/10.1029/2006JE002708.

M. Knapmeyer, S. Stähler, I. Daubar, F. Forget, A. Spiga, T. Pierron, M. van Driel, D. Banfield, E. Hauber, M. Grott, N. Müller, C. Perrin, A. Jacob, A. Lucas, B. Knapmeyer-Endrun, C. Newman, M. Panning, R. Weber, F. Calef, M. Böse, S. Ceylan, C. Charalambous, J. Clinton, N. Dahmen, D. Giardini, A. Horleston, T. Kawamura, A. Khan, G. Mainsant, M. Plasman, M. Lemmon, R. Lorenz, W. Pike, J.-R. Scholz, P. Lognonné, and B. Banerdt. Seasonal seismic activity on mars. *Earth Planet. Sci. Lett.*, 576:117171, 2021. ISSN 0012-821X. doi: https://doi.org/10.1016/j.epsl.2021.117171.

B. Knapmeyer-Endrun, M. P. Panning, F. Bissig, R. Joshi, A. Khan, D. Kim, V. Lekić, B. Tauzin, S. Tharimena, M. Plasman, N. Compaire, R. F. Garcia, L. Margerin, M. Schimmel, É. Stutzmann, N. Schmerr, E. Bozdağ, A.-C. Plesa, M. A. Wieczorek, A. Broquet, D. Antonangeli, S. M. McLennan, H. Samuel, C. Michaut, L. Pan, S. E. Smrekar, C. L. Johnson, N. Brinkman, A. Mittelholz, A. Rivoldini, P. M. Davis, P. Lognonné, B. Pinot, J.-R. Scholz, S. Stähler, M. Knapmeyer, M. van Driel, D. Giardini, and W. B. Banerdt. Thickness and structure of the martian crust from insight seismic data. *Science*, 373(6553):438–443, 2021. doi: 10.1126/science.abf8966.

L. Krischer, T. Megies, R. Barsch, M. Beyreuther, T. Lecocq, C. Caudron, and J. Wassermann. ObsPy: a bridge for seismology into the scientific Python ecosystem. *Comput. Sci. Discov.*, 8(1):014003, 2015.

P. Lognonné, W. Banerdt, D. Giardini, W. Pike, U. Christensen, P. Laudet, S. de Raucourt, P. Zweifel, S. Calcutt, M. Bierwirth, K. Hurst, F. Ijpelaan, J. Umland, R. Llorca-Cejudo, S. Larson, R. Garcia, S. Kedar,

B. Knapmeyer-Endrun, D. Mimoun, A. Mocquet, M. Panning, R. Weber, A. Sylvestre-Baron, G. Pont, N. Verdier, L. Kerjean, L. Facto, V. Gharakanian, J. Feldman, T. Hoffman, D. B. Klein, K. Klein, N. Onufer, J. Paredes-Garcia, M. Petkov, J. Willis, S. Smrekar, M. Drilleau, T. Gabsi, T. Nebut, O. Robert, S. Tillier, C. Moreau, M. Parise, G. Aveni, S. Ben Charef, Y. Bennour, T. Camus, P. Dandonneau, C. Desfoux, B. Lecomte, O. Pot, P. Revuz, D. Mance, J. ten Pierick, N. Bowles, C. Charalambous, A. Delahunty, J. Hurley, R. Irshad, H. Liu, A. Mukherjee, I. Standley, A. Stott, J. Temple, T. Warren, M. Eberhardt, A. Kramer, W. Kühne, E.-P. Miettinen, M. Monecke, C. Aicardi, M. André, J. Baroukh, A. Borrien, A. Bouisset, P. Boutte, K. Brethomé, C. Brysbaert, T. Carlier, M. Deleuze, J. M. Desmarres, D. Dilhan, C. Doucet, D. Faye, N. Faye-Refalo, R. Gonzalez, C. Imbert, C. Larigauderie, E. Locatelli, L. Luno, J.-R. Meyer, F. Mialhe, J. M. Mouret, M. Nonon, Y. Pahn, A. Paillet, P. Pasquier, G. Perez, R. Perez, L. Perrin, B. Pouilloux, A. Rosak, I. Savin de Larclause, J. Sicre, M. Sodki, N. Toulemont, B. Vella, C. Yana, F. Alibay, O. Avalos, M. Balzer, P. Bhandari, E. Blanco, B. Bone, J. Bousman, P. Bruneau, F. Calef, R. Calvet, S. D'Agostino, G. de los Santos, R. Deen, R. Denise, J. Ervin, N. Ferraro, H. Gengl, F. Grinblat, D. Hernandez, M. Hetzel, M. E. Johnson, L. Khachikyan, J. Lin, S. Madzunkov, S. Marshall, I. Mikellides, E. Miller, W. Raff, J. Singer, C. Sunday, J. Villalvazo, M. Wallace, D. Banfield, J. Rodriguez-Manfredi, C. Russell, A. Trebi-Ollennu, J. Maki, E. Beucler, M. Böse, C. Bonjour, J. Berenguer, S. Ceylan, J. Clinton, V. Conejero, I. Daubar, V. Dehant, P. Delage, F. Euchner, I. Estève, L. Fayon, L. Ferraioli, C. L. Johnson, J. Gagnepain-Beyneix, M. Golombek, A. Khan, T. Kawamura, B. Kenda, P. Labrot, N. Murdoch,

C. Pardo, C. Perrin, L. Pou, A. Sauron, D. Savoie, S. Stähler, E. Stutzmann, N. Teanby, J. Tromp, M. van Driel, M. Wieczorek, R. Widmer-Schnidrig, and J. Wookey. SEIS: Insight's Seismic Experiment for Internal Structure of Mars. *Space Sci. Rev.*, 215(1):12, 2019. doi: 10.1007/s11214-018-0574-6.

P. Lognonné, W. Banerdt, W. Pike, D. Giardini, U. Christensen, R. Garcia, T. Kawamura, S. Kedar, B. Knapmeyer-Endrun, L. Margerin, F. Nimmo, M. Panning, B. Tauzin, J.-R. Scholz, D. Antonangeli, S. Barkaoui, E. Beucler, F. Bissig, N. Brinkman, M. Calvet, S. Ceylan, C. Charalambous, P. Davis, M. van Driel, M. Drilleau, L. Fayon, R. Joshi, B. Kenda, A. Khan, M. Knapmeyer, V. Lekic, J. McClean, D. Mimoun, N. Murdoch, L. Pan, C. Perrin, B. Pinot, L. Pou, S. Menina, S. Rodriguez, C. Schmelzbach, N. Schmerr, D. Sollberger, A. Spiga, S. Stähler, A. Stott, E. Stutzmann, S. Tharimena, R. Widmer-Schnidrig, F. Andersson, V. Ansan, C. Beghein, M. Böse, E. Bozdag, J. Clinton, I. Daubar, P. Delage, N. Fuji, M. Golombek, M. Grott, A. Horleston, K. Hurst, J. Irving, A. Jacob, J. Knollenberg, S. Krasner, C. Krause, R. Lorenz, C. Michaut, B. Myhill, T. Nissen-Meyer, J. ten Pierick, A.-C. Plesa, C. Quantin-Nataf, J. Robertsson, L. Rochas, M. Schimmel, S. Smrekar, T. Spohn, N. Teanby, J. Tromp, J. Vallade, N. Verdier, C. Vrettos, R. Weber, D. Banfield, E. Barrett, E. Bierwirth, S. Calcutt, N. Compaire, C. Johnson, D. Mance, F. Euchner, L. Kerjean, G. Mainsant, A. Mocquet, J. Antonio Rodriguez Manfredi, G. Pont, P. Laudet, T. Nebut, S. de Raucourt, O. Robert, C. Russell, A. Sylvestre-Baron, S. Tillier, T. Warren, M. Wieczorek, C. Yana, and P. Zweifel. Constraints on the shallow elastic and anelastic structure of Mars from InSight seismic data. *Nat. Geosci.*,

2020. doi: 10.1038/s41561-020-0536-y.

R. D. Lorenz, G. M. Martínez, A. Spiga, A. Vicente-Retortillo, C. E. Newman, N. Murdoch, F. Forget, E. Millour, and T. Pierron. Lander and rover histories of dust accumulation on and removal from solar arrays on mars. *Planetary and Space Science*, 207:105337, 2021. ISSN 0032-0633. doi: https://doi.org/10.1016/j.pss.2021.105337.

L. Martire, R. F. Garcia, L. Rolland, A. Spiga, P. H. Lognonné, D. Banfield, W. B. Banerdt, and R. Martin. Martian Infrasound: Numerical Modeling and Analysis of InSight's Data. *J. Geophys. Res.: Planets*, 125(6): e2020JE006376, 2020. doi: https://doi.org/10.1029/2020JE006376.

C. Perrin, A. Jacob, A. Lucas, R. Myhill, E. Hauber, A. Batov, T. Gudkova, S. Rodriguez, P. Lognonné, J. Stevanović, M. Drilleau, and N. Fuji. Geometry and segmentation of cerberus fossae, mars: Implications for marsquake properties. *J. Geophys. Res.: Planets*, 127(1):e2021JE007118, 2022. doi: https://doi.org/10.1029/2021JE007118.

H. Samuel, M. D. Ballmer, S. Padovan, N. Tosi, A. Rivoldini, and A.-C. Plesa. The thermo-chemical evolution of Mars with a strongly stratified mantle. *J. Geophys. Res.: Planets*, n/a(n/a):e2020JE006613, 2021. ISSN 2169-9100. doi: 10.1029/2020JE006613.

J.-R. Scholz, R. Widmer-Schnidrig, P. Davis, P. Lognonné, B. Pinot, R. F. Garcia, K. Hurst, L. Pou, F. Nimmo, S. Barkaoui, S. de Raucourt, B. Knapmeyer-Endrun, M. Knapmeyer, G. Orhand-Mainsant, N. Compaire, A. Cuvier, É. Beucler, M. Bonnin, R. Joshi, G. Sainton, E. Stutzmann, M. Schimmel, A. Horleston, M. Böse, S. Ceylan, J. Clinton, M. van

Driel, T. Kawamura, A. Khan, S. C. Stähler, D. Giardini, C. Charalambous, A. E. Stott, W. T. Pike, U. R. Christensen, and W. B. Banerdt. Detection, Analysis, and Removal of Glitches From InSight's Seismic Data From Mars. *Earth and Space Science*, 7(11):e2020EA001317, 2020. doi: https://doi.org/10.1029/2020EA001317.

D. Schorlemmer, F. Euchner, P. Kastli, J. Saul, and the QuakeML Working Group. QuakeML: status of the XML-based seismological data exchange format. *Annals of Geophysics*, 2011. doi: 0.4401/ag-4874.

D. E. Smith, M. T. Zuber, H. V. Frey, J. B. Garvin, J. W. Head, D. O. Muhleman, G. H. Pettengill, R. J. Phillips, S. C. Solomon, H. J. Zwally, W. B. Banerdt, T. C. Duxbury, M. P. Golombek, F. G. Lemoine, G. A. Neumann, D. D. Rowlands, O. Aharonson, P. G. Ford, A. B. Ivanov, C. L. Johnson, P. J. McGovern, J. B. Abshire, R. S. Afzal, and X. Sun. Mars orbiter laser altimeter: Experiment summary after the first year of global mapping of mars. *J. Geophys. Res.: Planets*, 106(E10):23689–23722, 2001. doi: https://doi.org/10.1029/2000JE001364.

S. Stähler, A. Khan, W. Bruce Banerdt, P. Lognonné, D. Giardini, Savas Ceylan, M. Drilleau, C. Duran, R. F. Garcia, Quancheng Huang, Doyeon Kim, V. Lekic, H. Samuel, M. Schimmel, N. Schmerr, D. Sollberger, Éléonore Stutzmann, Zongbo Xu, D. Antonangeli, Constantinos Charalambous, P. Davis, J. C. Irving, T. Kawamura, M. Knapmeyer, R. Maguire, A. G. Marusiak, M. P. Panning, C. Perrin, Ana-Catalina Plesa, A. Rivoldini, C. Schmelzbach, G. Zenhäusern, Éric Beucler, J. Clinton, N. Dahmen, M. Van Driel, T. Gudkova, A. Horleston, W. Thomas Pike, M. Plasman, and S. E. Smrekar. Inte-

rior models of mars from inversion of seismic body waves, 2021a. URL https://www.seis-insight.eu/en/science/seis-products/interior-models-of-mars-from-i

S. C. Stähler, A. Khan, W. B. Banerdt, P. Lognonné, D. Giardini, S. Ceylan, M. Drilleau, A. C. Duran, R. F. Garcia, Q. Huang, D. Kim, V. Lekic, H. Samuel, M. Schimmel, N. Schmerr, D. Sollberger, É. Stutzmann, Z. Xu, D. Antonangeli, C. Charalambous, P. M. Davis, J. C. E. Irving, T. Kawamura, M. Knapmeyer, R. Maguire, A. G. Marusiak, M. P. Panning, C. Perrin, A.-C. Plesa, A. Rivoldini, C. Schmelzbach, G. Zenhäusern, É. Beucler, J. Clinton, N. Dahmen, M. van Driel, T. Gudkova, A. Horleston, W. T. Pike, M. Plasman, and S. E. Smrekar. Seismic detection of the martian core. *Science*, 373(6553):443–448, 2021b. doi: 10.1126/science.abi7730.

D. A. Storchak, J. Schweitzer, and P. Bormann. The IASPEI Standard Seismic Phase List. *Seismological Research Letters*, 74(6):761–772, 11 2003. ISSN 0895-0695. doi: 10.1785/gssrl.74.6.761.

S. Stähler. marsquakeservice/locator: Release for v5 MQS catalog, Dec 2020. URL https://doi.org/10.5281/zenodo.4302312.

M. van Driel, S. Ceylan, J. F. Clinton, D. Giardini, A. Horleston, L. Margerin, S. C. Stähler, M. Böse, C. Charalambous, T. Kawamura, A. Khan, G. Orhand-Mainsant, J.-R. Scholz, F. Euchner, M. Knapmeyer, N. Schmerr, W. T. Pike, P. Lognonné, and W. B. Banerdt. High-frequency seismic events on Mars observed by InSight. *J. Geophys. Res.: Planets*, 126(2):e2020JE006670, 2021. doi: https://doi.org/10.1029/2020JE006670.

G. Zenhäusern, S. C. Stähler, J. F. Clinton, D. Giardini, S. Ceylan, and R. F. Garcia. Low frequency marsquakes and where to find them: Back azimuth

determination using a polarization analysis approach. *Bull. Seismol. Soc. Am.*, pages 1–19, 2022. doi: 10.1785/0120220019.

P. Zweifel, D. Mance, J. ten Pierick, D. Giardini, C. Schmelzbach, T. Haag, T. Nicollier, S. Ceylan, S. Stähler, M. van Driel, D. Sollberger, F. Euchner, J. F. Clinton, M. Bierwirth, M. Eberhardt, P. Lognonné, W. T. Pike, and W. B. Banerdt. Seismic High-Resolution Acquisition Electronics for the NASA InSight Mission on Mars. *Bull. Seismol. Soc. Am.*, 111(6):2909–2923, 10 2021. ISSN 0037-1106. doi: 10.1785/0120210071.

Data availability

The InSight seismic event catalogue version 9 (InSight Marsquake Service, 2022) and waveform data (InSight Mars SEIS Data Service, 2019a,b) are available from the IPGP Datacenter and IRIS-DMC, as are previous catalogue versions. Seismic waveforms are also available from NASA PDS (National Aeronautics and Space Administration Planetary Data System) (https://pds.nasa.gov/).

Declaration of Competing Interest

The authors declare that they have no known competing financial interests or personal relationships that could have appeared to influence the work reported in this paper.

Acknowledgements

We acknowledge NASA, CNES, their partner agencies and Institutions (UKSA, SSO, DLR, JPL, IPGP-CNRS, ETHZ, IC, MPS-MPG) and the

flight operations team at JPL, SISMOC, MSDS, IRIS-DMC and PDS for providing SEED SEIS data. The InSight event catalogue and waveform data are available from the IRIS-DMC, NASA-PDS, SEIS-InSight data portal and IPGP data center (InSight Mars SEIS Data Service, 2019a,b; InSight Marsquake Service, 2022). A.H. is funded by the UKSA under grant numbers ST/R002096/1 and ST/W002523/1. N.D., C.D., G.Z., S.C., and S.C.S. would like to acknowledge support from ETH through the ETH+ funding scheme (ETH+02 19-1: "Planet Mars"). The co-authors from the French institutions acknowledge funding support provided by Centre national d'études spatiales (CNES) and the Agence Nationale de la Recherche (ANR-19-CE31-0008-08 MAGIS) for SEIS operation and SEIS Science analysis. The majority of visualizations are prepared using the matplotlib library (Hunter, 2007). The ObsPy (Krischer et al., 2015) and NumPy (Harris et al., 2020) packages are heavily used for data processing. This manuscript is InSight contribution number 270.

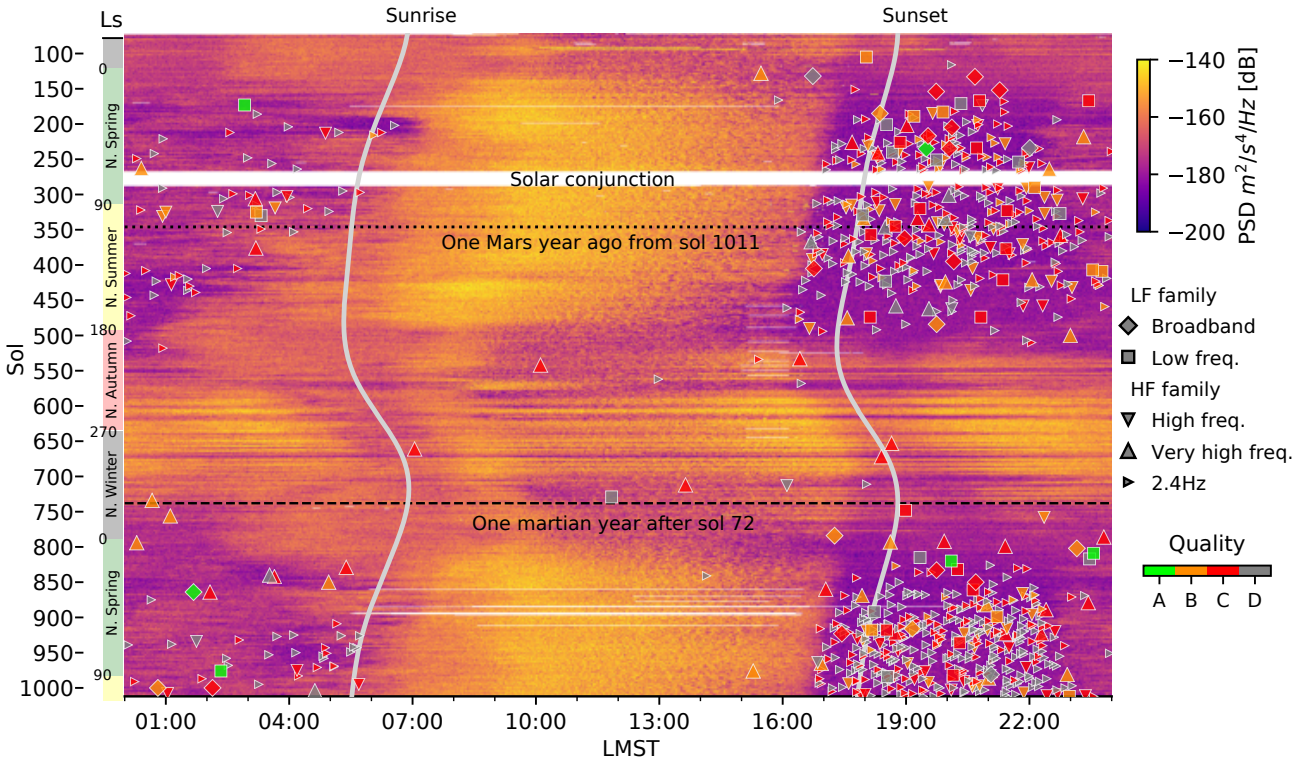

Figure 1: Summary plot for V9 showing the broadband noise evolution recorded by VBB vertical component on Mars. The background image comprises a stack of sol-long acceleration spectrograms for frequencies 0.05–4 Hz. The x-axis is the local mean solar time (LMST). The InSight sols and corresponding solar longitudes (Ls) with Martian seasons in the northern hemisphere are shown on the y-axis. The LF and HF families in the V9 catalogue are marked with symbols, while the event qualities are indicated by colour. The plot covers the period from sol 72, shortly before the WTS was placed and SEIS started continuous recording, up to sol 1011. Sol 72–740 (dashed line) is the first full Martian year of high-quality data. The dotted line at sol 343 indicates the corresponding time one Martian before the end of the V9 period on sol 1011. The white regions on the spectrograms are data gaps, the largest being the solar conjunction. The previous catalogue paper (Clinton et al., 2021) ends on sol 478, which was described in V3.

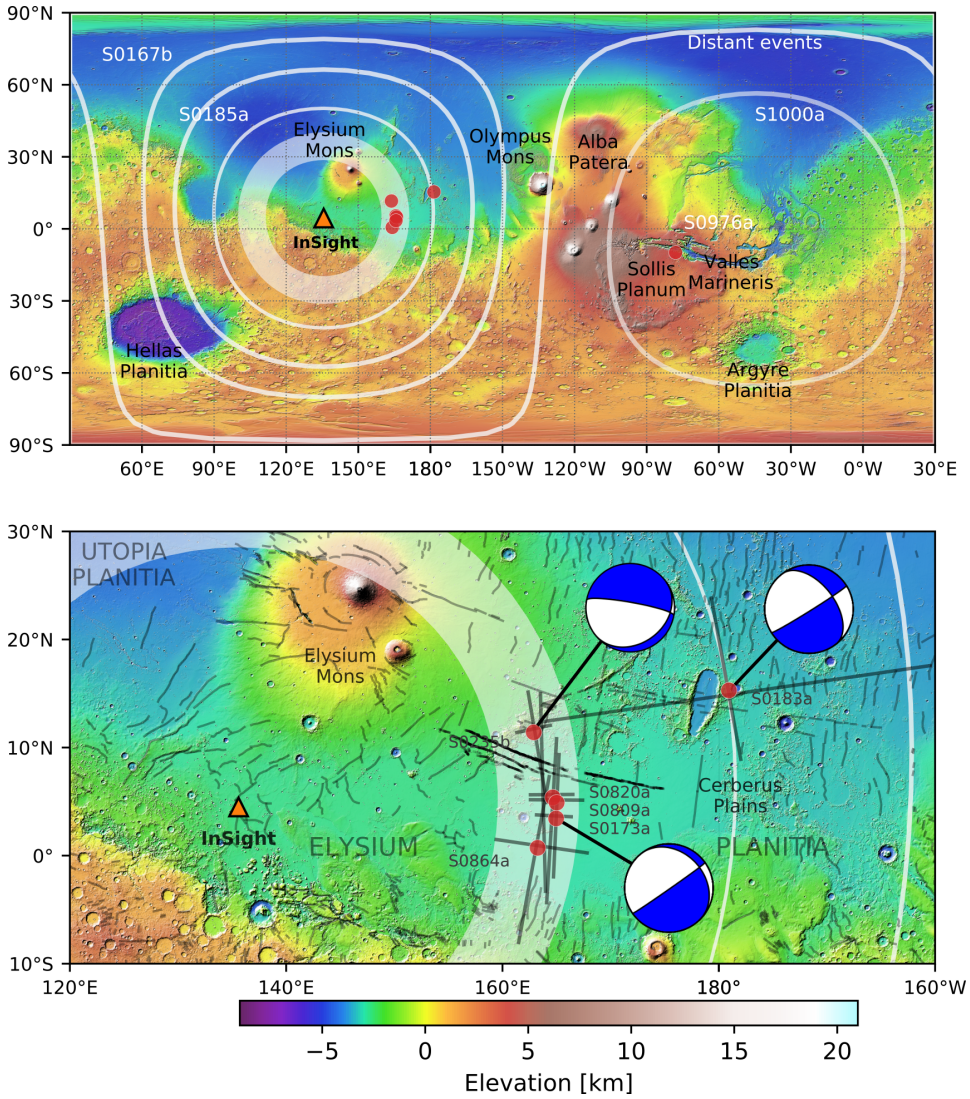

Figure 2: The seismicity map of Mars for the LF family events. The background map is from Mars Orbiter Laser Altimeter (MOLA, Smith et al. (2001)). The top panel shows the events at the global scale, while the bottom panel zooms around the Cerberus Fossae region. The focal mechanisms in the bottom panel are from Brinkman et al. (2021). The uncertainties in backazimuth and distance estimates are shown with lines in the bottom panel. The fault data are from Knapmeyer et al. (2006) and Perrin et al. (2022).

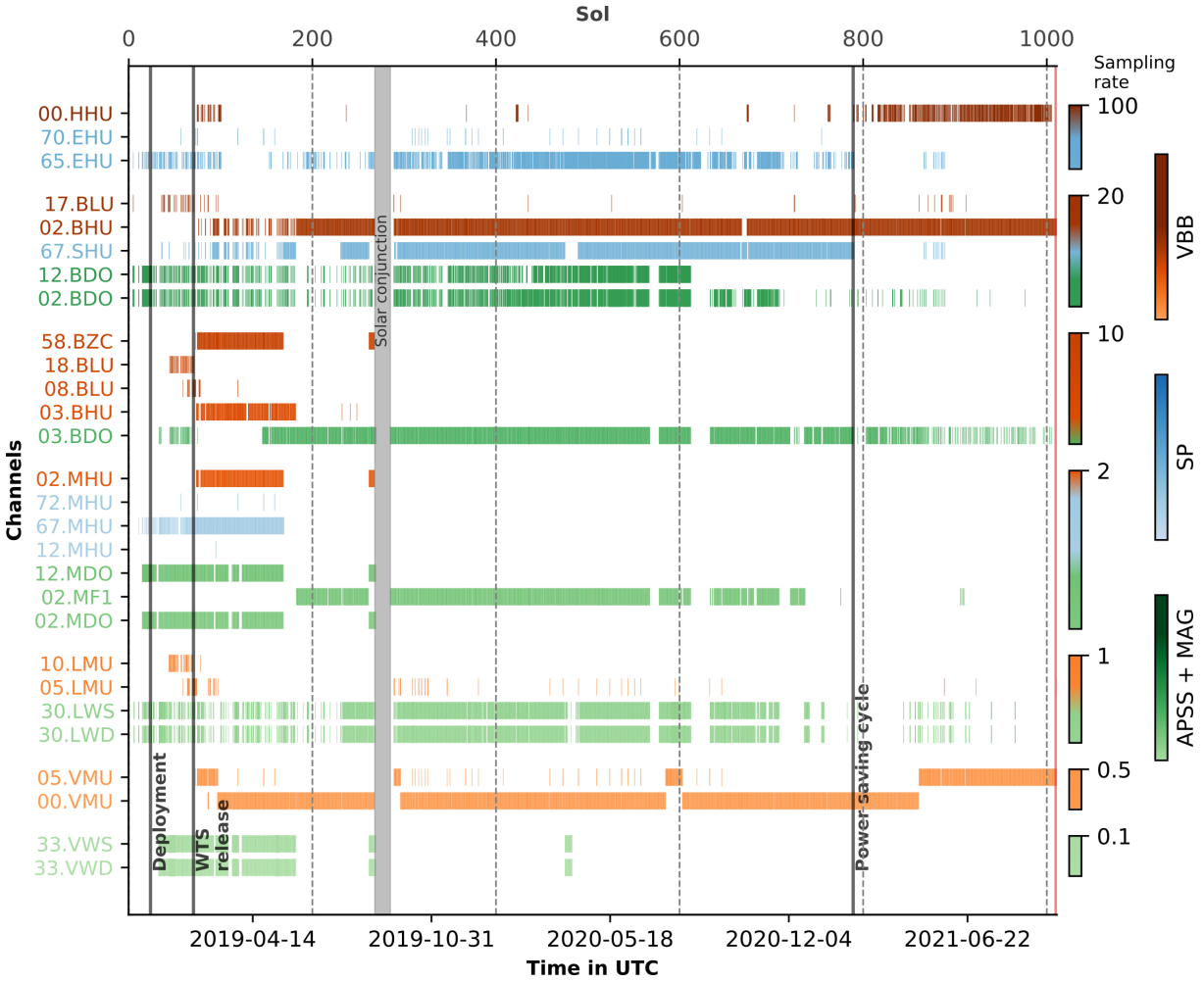

Figure 3: Summary of data collected from InSight between sols 0–1011 for channels commonly used by MQS (see Ceylan et al. (2021) for definition of channel codes). For simplicity, only one of the channels for 3–component sensors is shown. The colours represent instrument types. Channels are grouped by sampling rate. VBB and SP are the seismic sensors. APSS includes the wind and pressure channels, and MAG is the magnetometer. VBB is the preferred sensor for seismic monitoring. Since around sol 180, the 20 sps VBB channels (02.BHU/V/W) are the main data streams MQS utilizes for data monitoring. SP continuous operation stopped on sol 789 due to power saving cycle as labelled.

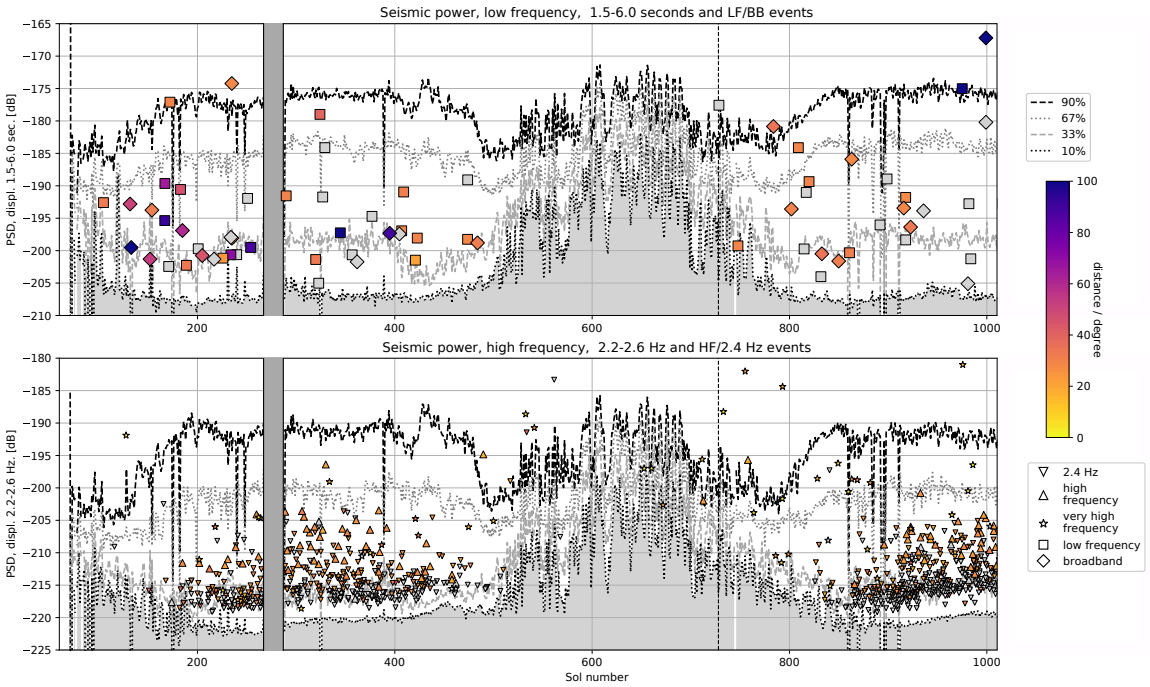

Figure 4: Summary image showing the evolving Martian background noise as recorded by the VBB vertical component as well as the occurrence, amplitude and distances of LF family (top) and HF family (bottom) marsquakes in the V9 catalogue. Symbols indicate the marsquake event type and colour bar shows event distances. Percentiles of the noise for each sol are indicted. Note the clear evolution of noise amplitudes across the seasons and the repeating noise levels from year to year. The first full Martian year ends on sol 740, indicated by the vertical dashed line. These extended periods of low noise in spring and summer coincide with the routine detection of HF events. The noise evolution at longer periods and at 2.4 Hz follow the same trends.

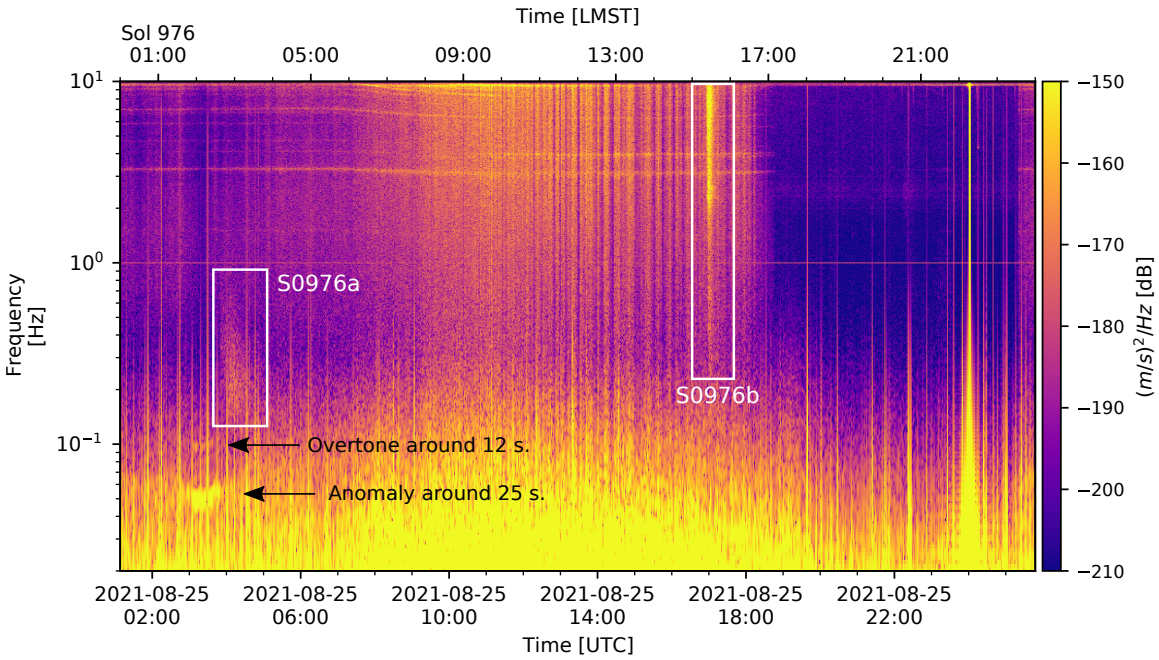

Figure 5: Velocity spectrogram for sol 976 using VBB North component. This sol includes two significant events (S0976a, LF QA and S0976b, VF QB), which are discussed in the review of seismicity section. Note that S0976a is preceded by the 18–25 s anomaly and its harmonics at around 12 s. The feature at 1 Hz with constant amplitude is an artefact caused by electronics referred as *tick noise* (Zweifel et al., 2021). Note the lander modes at higher frequencies are activated when the background noise is amplified during the windy periods.

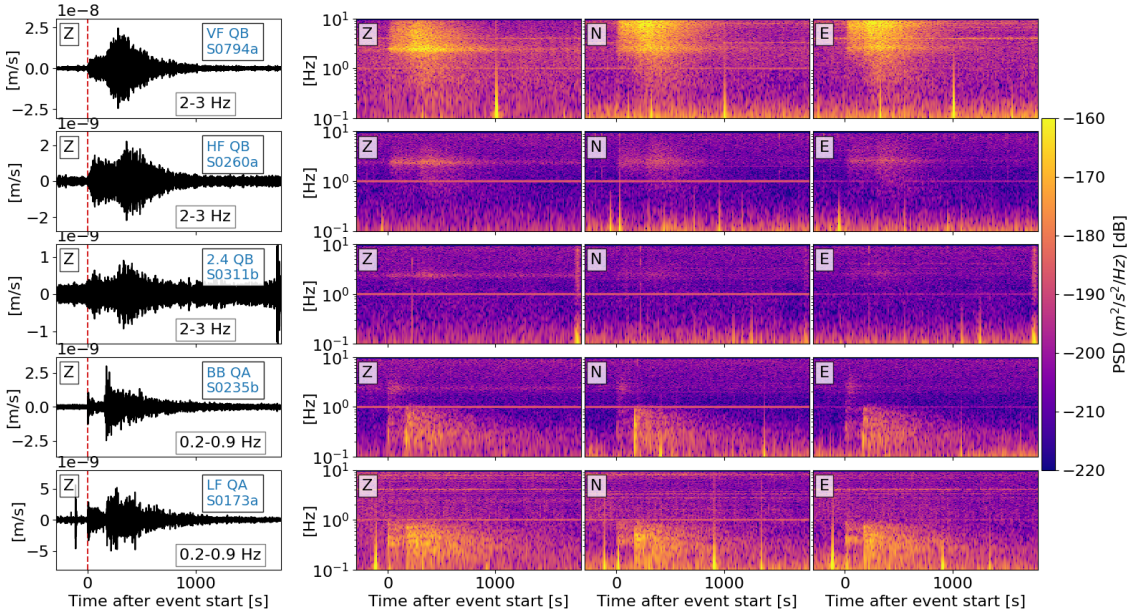

Figure 6: Examples of seismic events of the highest quality from each event type. The top three rows are from the HF family (QB), while bottom two rows show events from the LF family (QA). The waveforms are bandpass filtered vertical component seismic data as indicated in each panel. Spectrograms are for all three components in m/s.

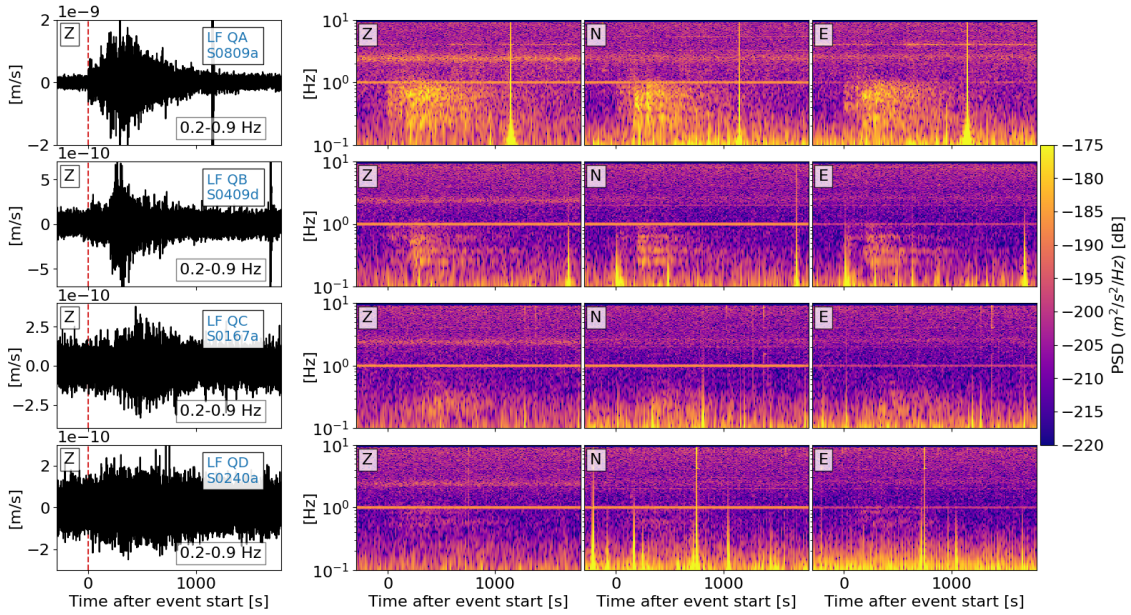

Figure 7: Examples of degrading event quality for LF events. The waveforms are band-pass filtered vertical component VBB data. Frequency range is indicated in each panel. Spectrograms are for all three components in m/s.

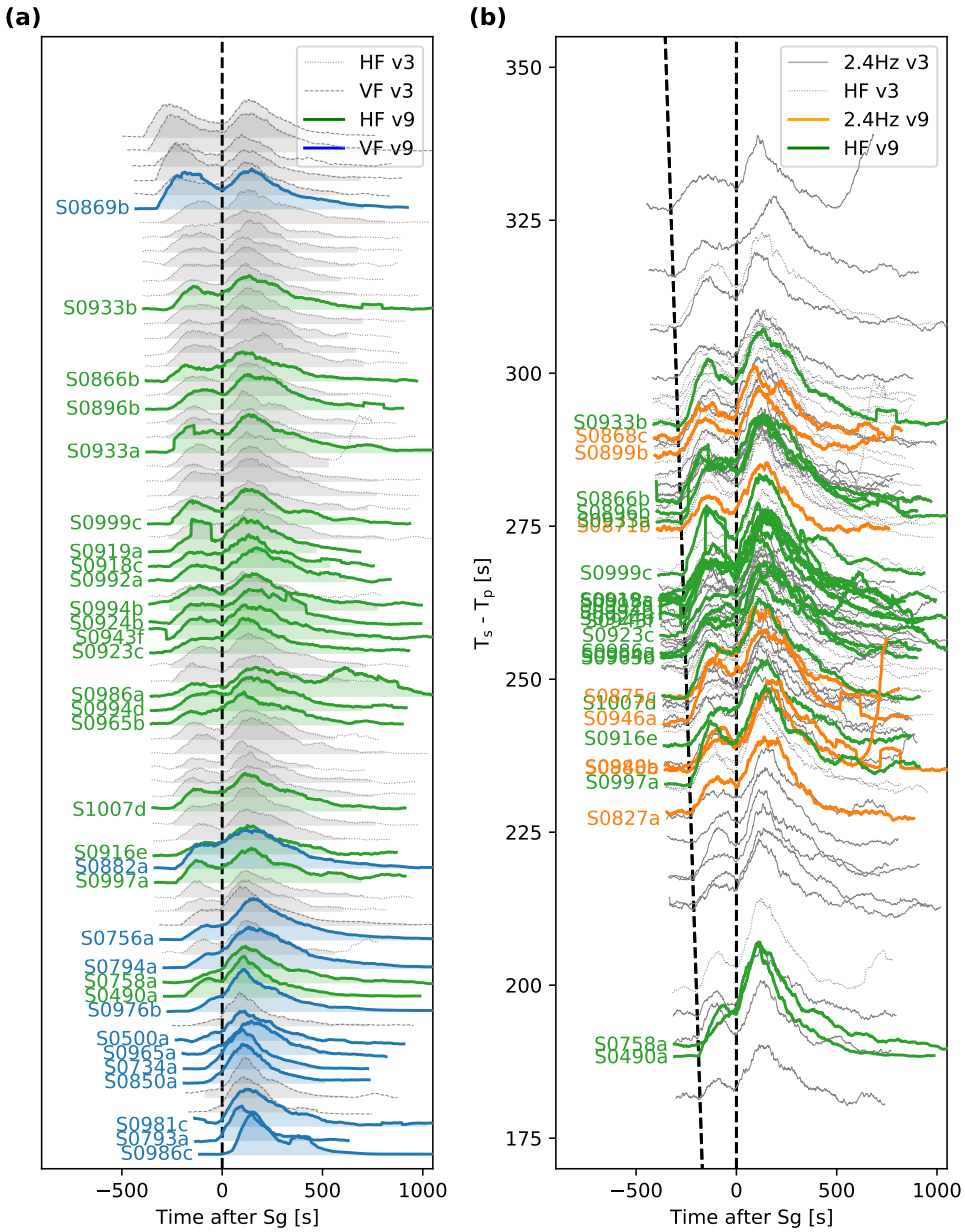

Figure 8: Envelopes for quality B high-frequency events. (a) HF and VF aligned on the Sg arrivals, sorted by distance with regular spacing, and (b) HF and 2.4 Hz events ordered by Ts–Tp differential times. The events reported in the V3 catalogue are plotted in grey, while coloured envelopes show V9 events. The envelopes are normalized and computed using the vertical component of VBB. The figure follows van Driel et al. (2021).

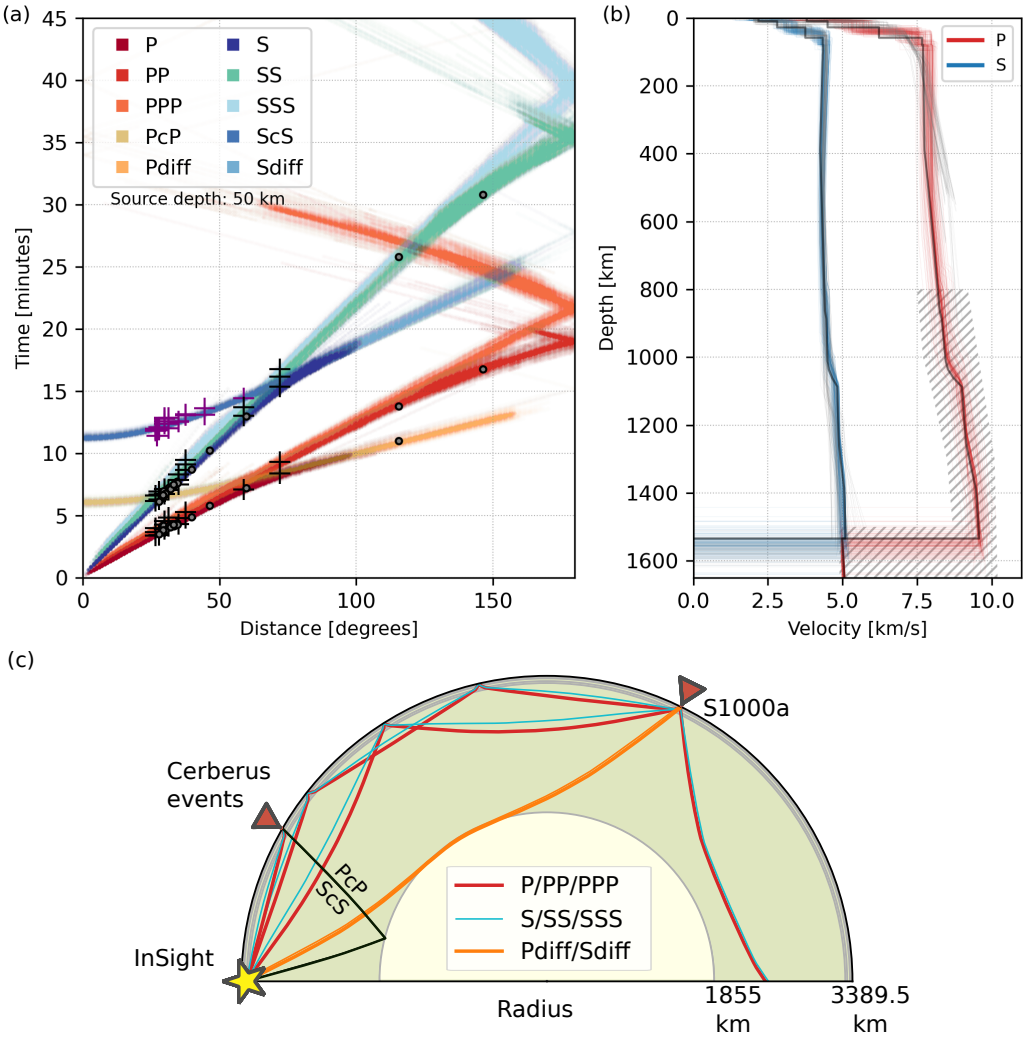

Figure 9: Theoretical arrival times for major seismic phases using a reference model from Stähler et al. (2021b) (Supp. Table S3). (a) Travel time curves for P– and S–waves, their surface reflections (PP, PPP and SS, SSS), core reflected (PcP and ScS) and core diffracted (Pdiff, Sdiff) phases for a source at 50 km depth. The black crosses denote the seismic phase picks used in Khan et al. (2021) for body-wave multiples, and purple crosses show core reflected ScS phases as reported in Stähler et al. (2021b). Grey circles are seismic phase picks of MQS used for locating the events. The phase picks do not reflect the pick uncertainties. (b) Seismic wave speed profiles of the models used in panel (a). The hatched region on the P-wave profiles is not constrained by observations; therefore, the P-wave travel time curves beyond $\sim 100^\circ$ are purely from model predictions. The solid black line is the reference model used for alignments. A reference travel time table is provided in the Supp. Table S3 using the same reference model. (c) The ray paths of the seismic phases shown in panel (a).

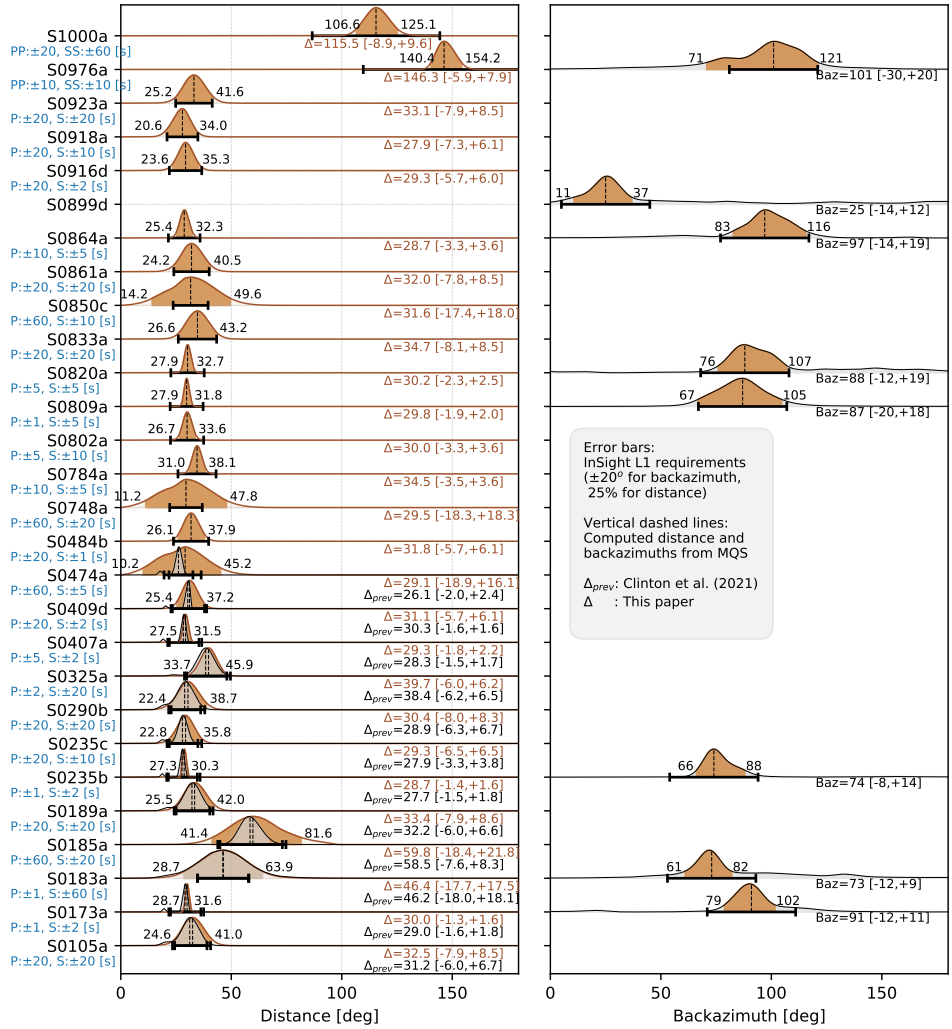

Figure 10: Distance and backazimuth probability density functions (PDF). The tan-coloured PDFs are from catalogue V3 (InSight Marsquake Service, 2020b; Clinton et al., 2021), orange PDFs indicate uncertainties from this study after the fix in the location codes. The horizontal error bars show the L1 mission requirements as indicated in the legend. S0183a is a QB event with a full location, and is the only exception in the catalogue.

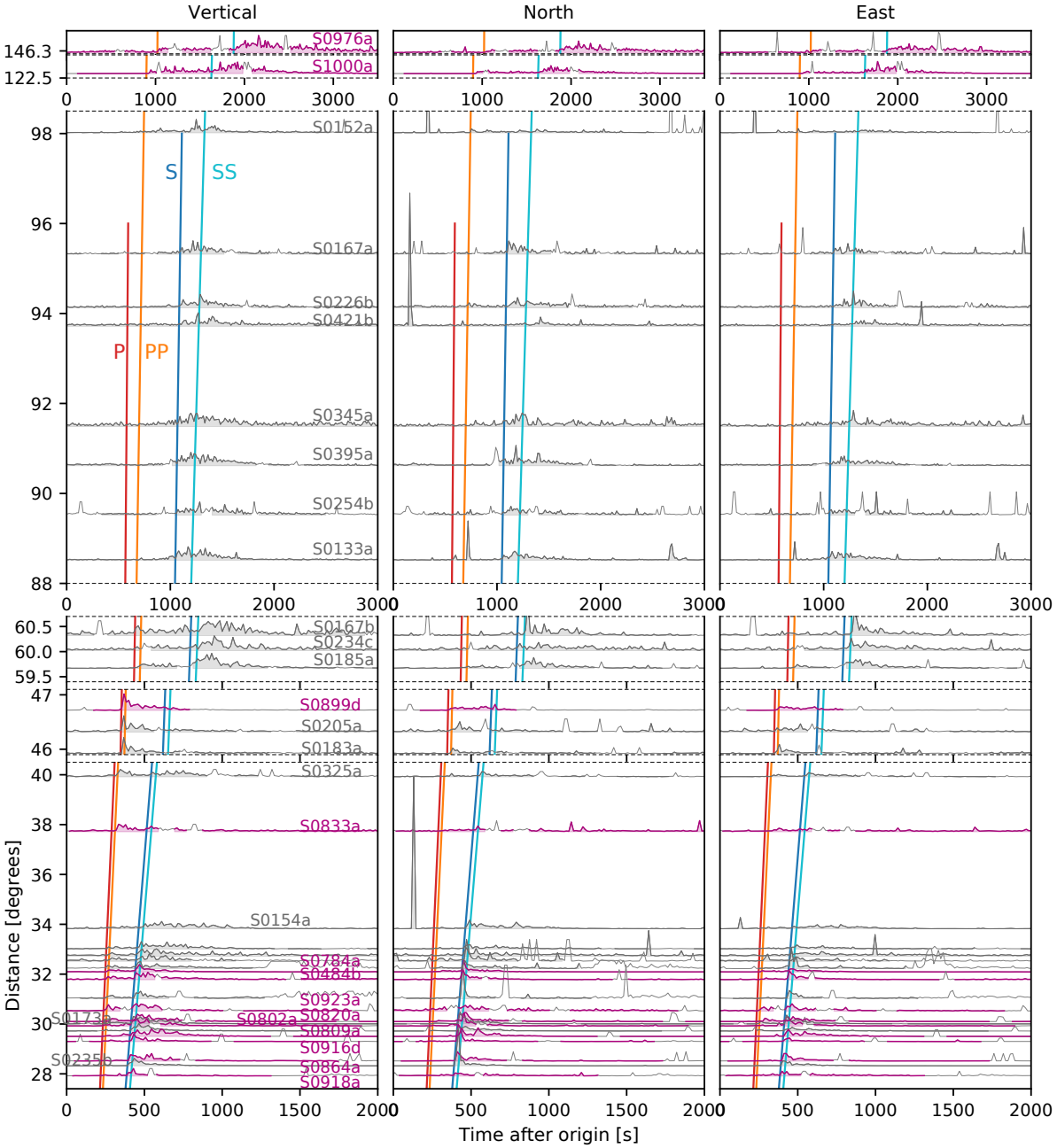

Figure 11: Alignment summary for events in the V9 catalogue. Events new to this catalogue are highlighted in purple. The events up to ∼45° are aligned against the P- and S-wave envelopes. Events around 90° do not show any indication of a P-phase. These events are temporarily aligned with the S-wave energy arrival and their S–wave coda length. Further out events are aligned with respect to PP and SS phases. The reference model for travel times is from Stähler et al. (2021b) (Fig. 9b). The spikes especially dominant on the horizontal components are glitches (Ceylan et al., 2021; Scholz et al., 2020)

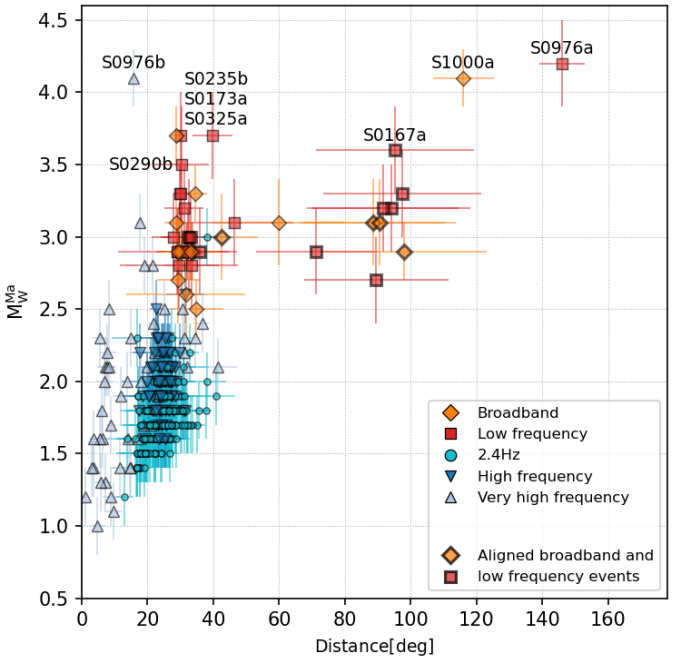

Figure 12: Distance vs. Mars-calibrated moment magnitude (M_W^{Ma}) distribution of the events included in the V9 catalogue. The magnitudes are computed following Böse et al. (2021). The events with $M_W^{Ma} \geq 3.5$ are labelled. Markers with thicker edges indicate the events that have a distance from alignments. Other events have been located using the phase picks from MQS.

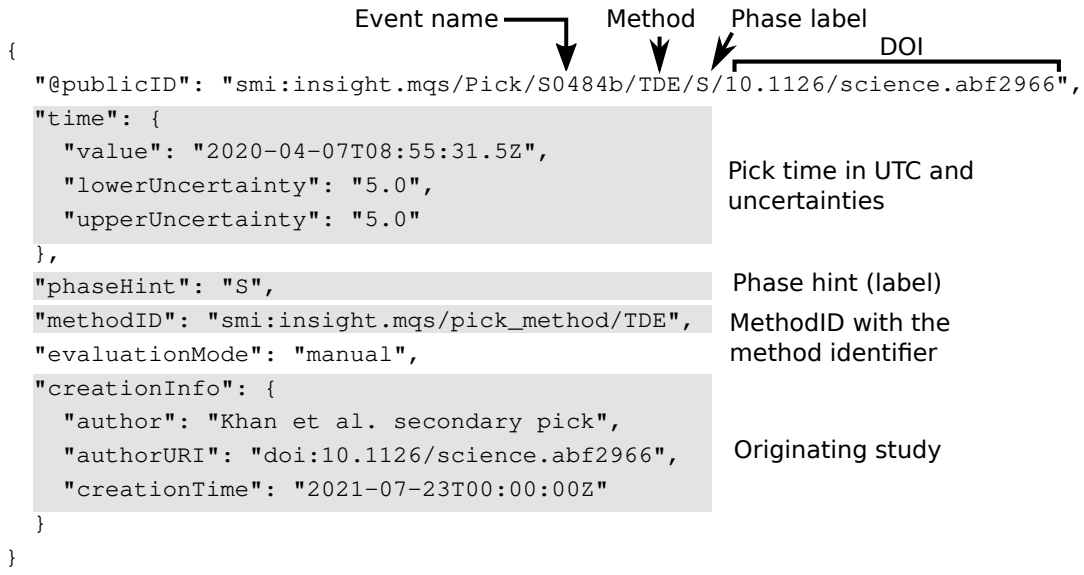

Figure 13: An example QuakeML (Schorlemmer et al., 2011) pick block for an S–phase picked by Khan et al. (2021) for S0484b. The publicID is constructed with all key pick attributes. The methodID identifies which method was used to make the pick, in this case TDE (time domain envelopes, see Table 2).

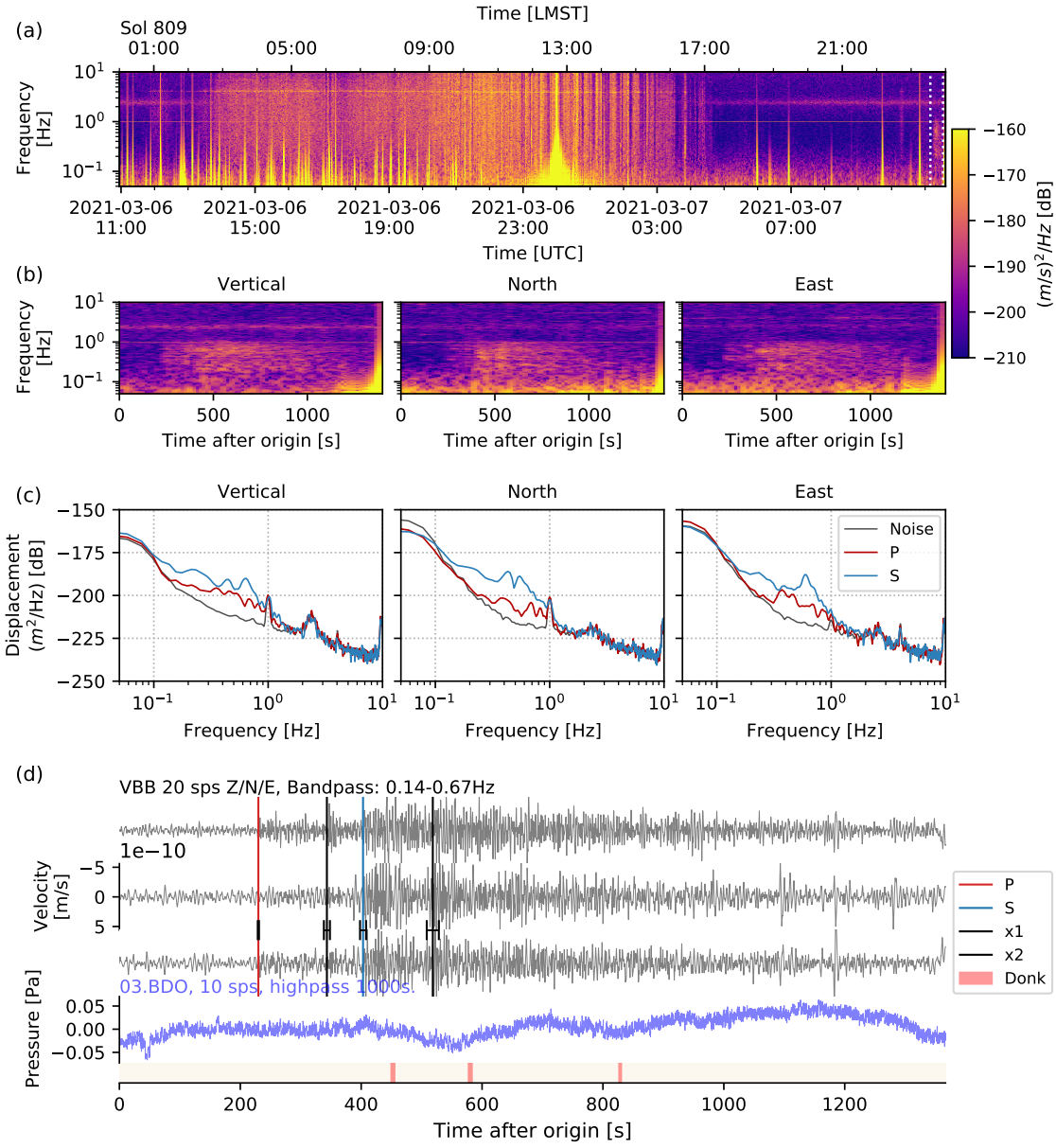

Figure 14: Summary of S0809a (LF, QA). (a) Sol-long velocity spectrogram for 20 sps VBB vertical component. The event is marked with white dashed lines between its origin time and signal end. The spectrogram is computed using a window length of 200 s with 50% overlap. The broadband high-amplitude features are glitches. (b) Three-component velocity spectrograms (window length 80 s, overlap 80%) zooming around the event as shown in panel (a). (c) The displacement spectra for three component VBBs, calculated using Welch's method using a window length of 25 s and 50% overlap. The time windows for noise and phases are hand-picked. (d) Bandpass filtered VBB waveforms. Artefacts like glitches or donks (Ceylan et al., 2021) are marked with purple boxes at the bottom panel. The coloured vertical lines show phase picks, while horizontal error bars indicate pick uncertainties.

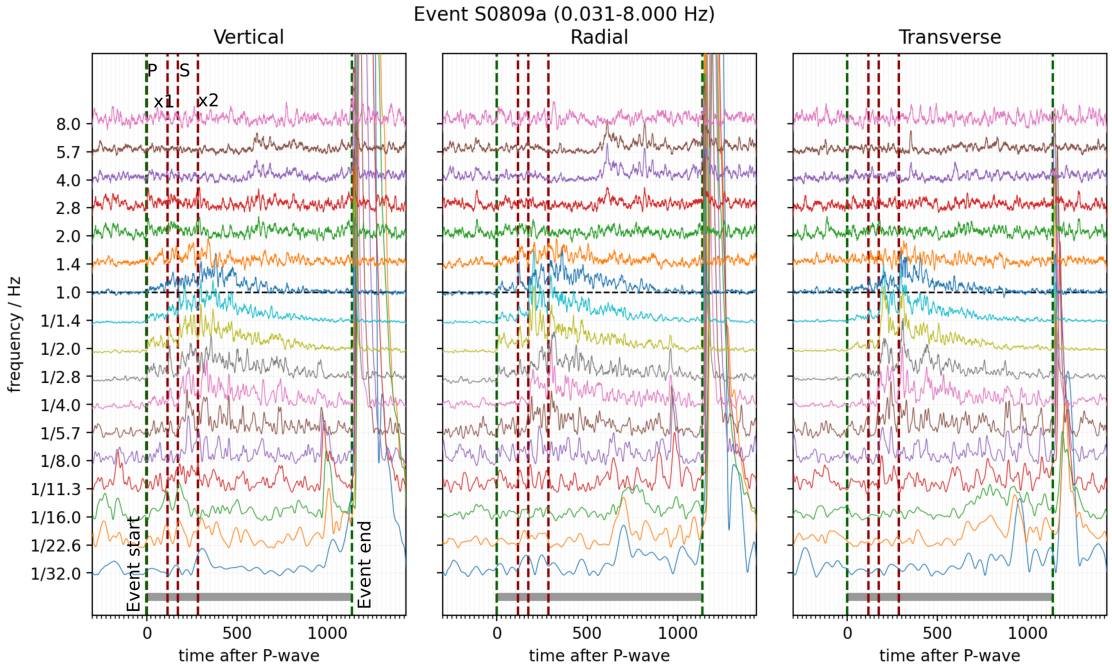

Figure 15: Filterbanks for S0809a (LF, QA) between 1/32–8 Hz for three components using 20 sps VBB velocity data. The seismic phases (P, S, x1 and x2) as picked by MQS are marked. The data are rotated into vertical-radial-transverse coordinate framework. Filterbanks are 1 octave wide, centered on the indicated frequencies.

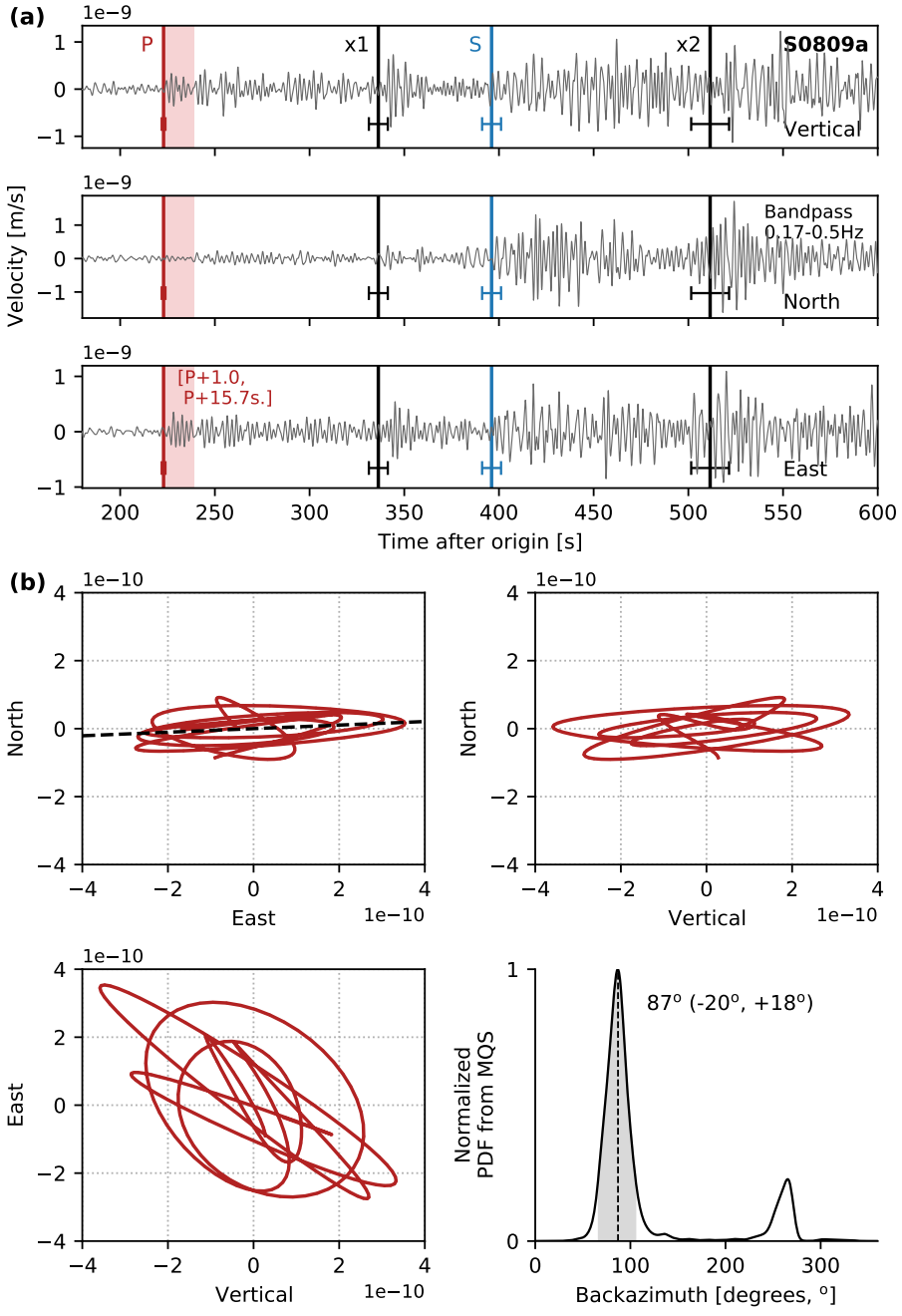

Figure 16: Polarization analysis of S0809a (LF, QA). (a) three-component waveforms, bandpass filtered between 0.17–0.5 Hz as indicated on North component. (b) particle motion plots for East–North, Vertical–North, and Vertical–East components. Bottom-right panel shows the normalized backazimuth PDF (probability density function) from MQS with backazimuth estimate and uncertainties marked.

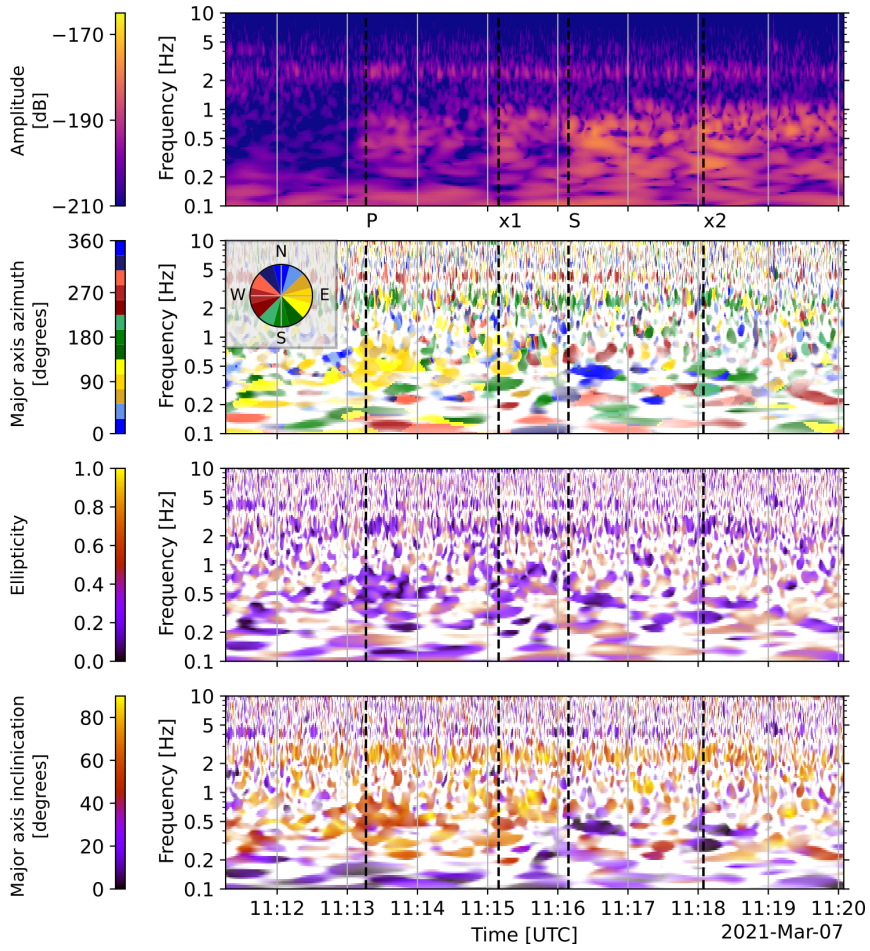

Figure 17: Polarization analysis of S0809a (LF, QA) using wavelet transform following Zenhäusern et al. (2022). The top panel is the 3-component velocity scalogram zooming around phase picks. The polarization attributes are shown as the major axis azimuth from North (second panel), ellipticity (third panel), and inclination from horizontal (last panel). P, S, x1, and x2 phases are marked with vertical dashed lines. The P and x1 phases point to azimuth of $\sim 90^\circ$ due East.

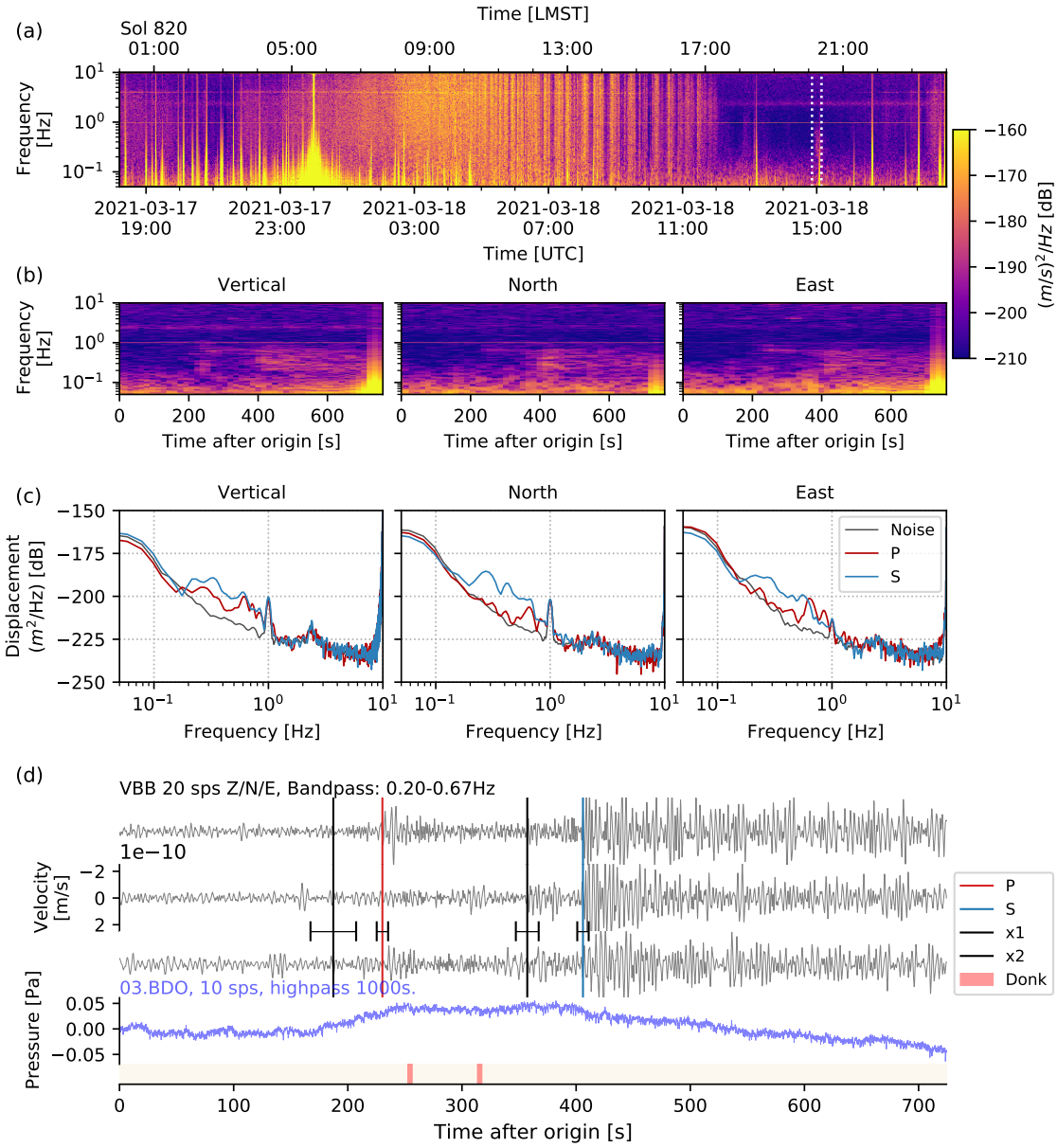

Figure 18: Event summary for S0820a (LF, QA). The figure caption and processing parameters follow Fig. 14.

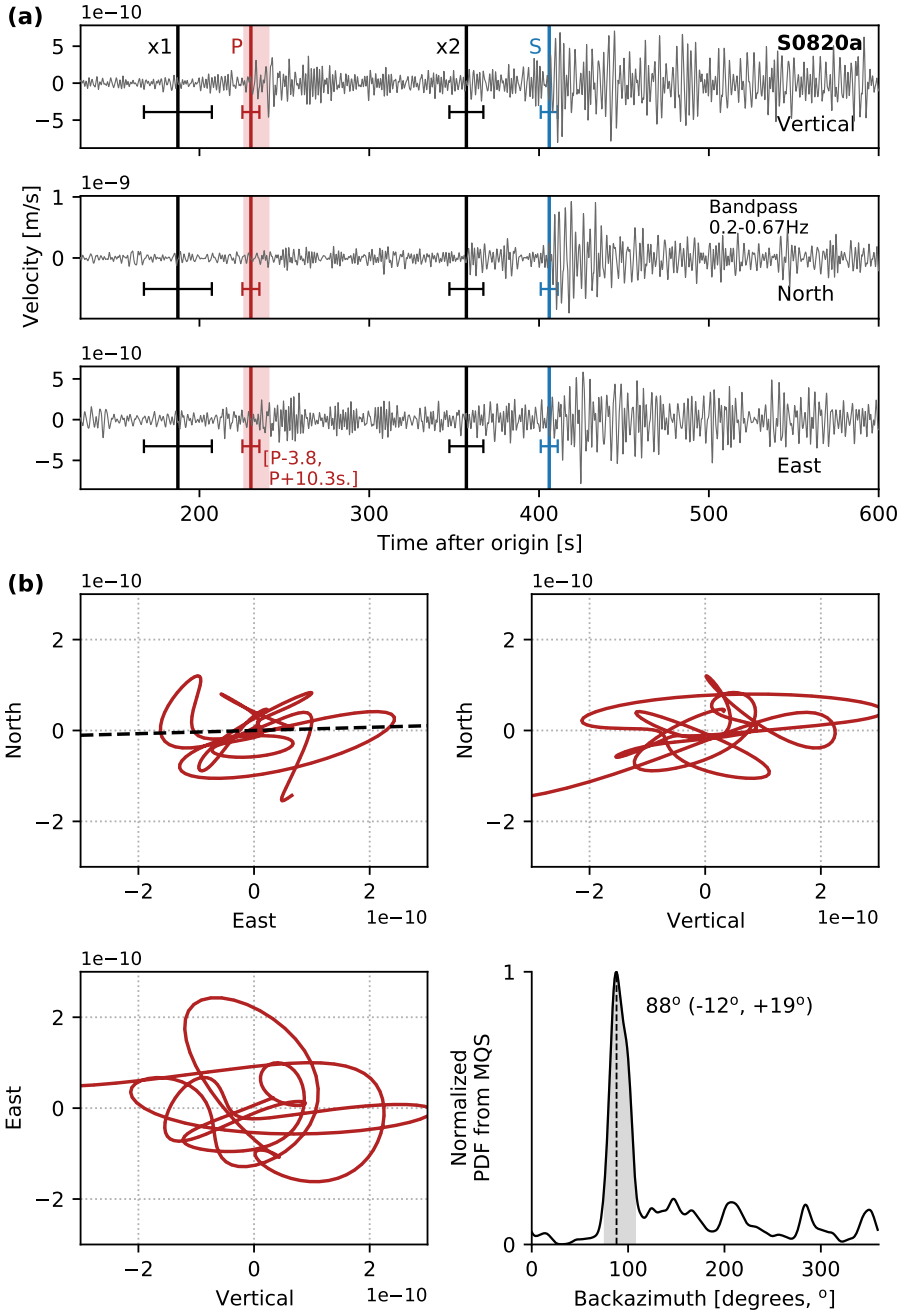

Figure 19: Polarization analysis of S0820a (LF, QA). The waveforms in (a) are bandpass filtered between 0.2-0.67 Hz as indicated. Other details follow Fig. 16.

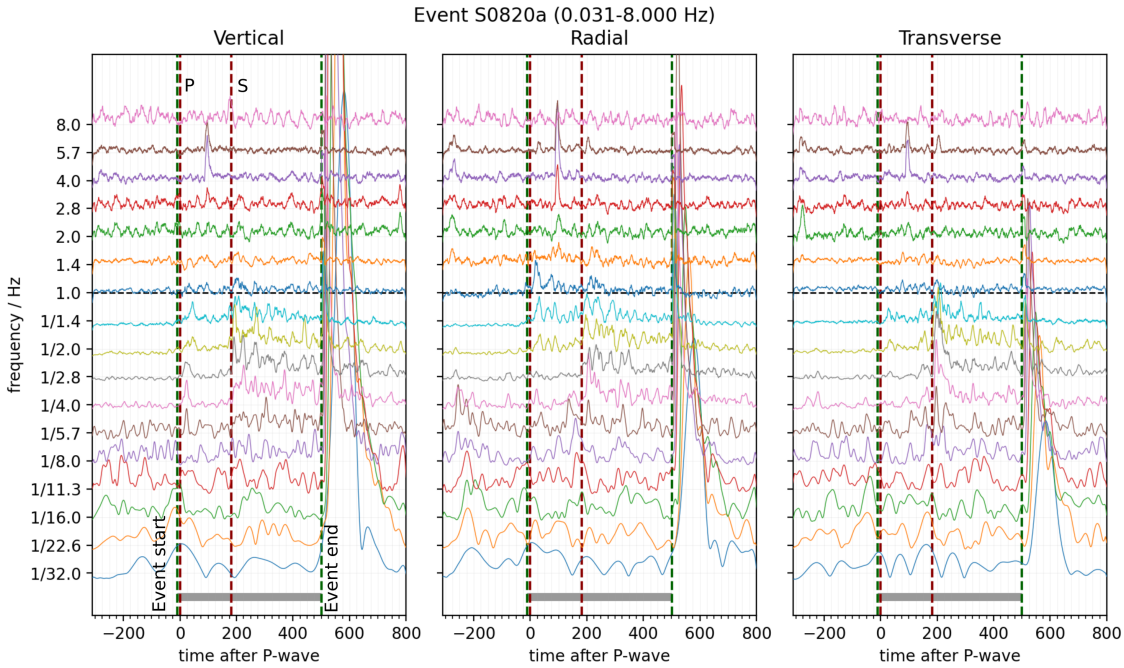

Figure 20: Filterbanks for S0820a (LF, QA). The figure caption follows Fig. 15. The high amplitude feature visible on all frequency bands after the event end is a glitch. The spike between P- and S-picks between 2.8–5.7 Hz is a donk, a very frequent and short duration (∼30 s) data artefact seen at frequencies above 10 Hz. Some of the large-amplitude donks may excite lander modes as seen in this example.

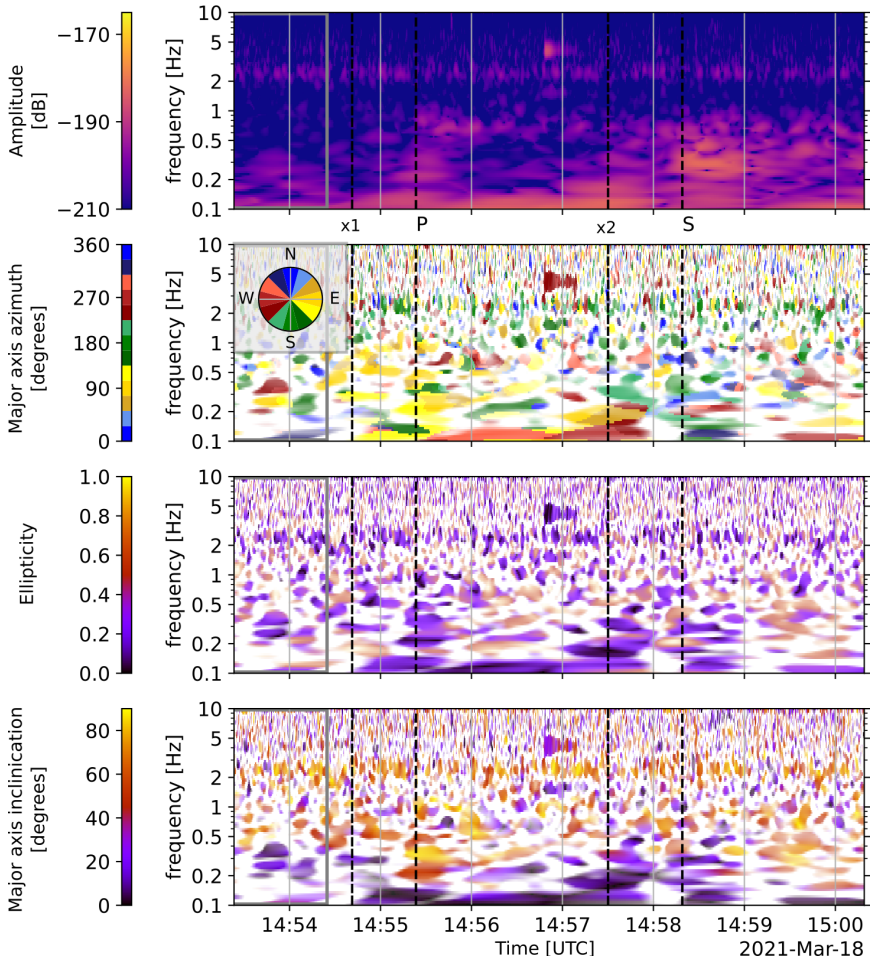

Figure 21: Polarization for S0820a (LF, QA) using wavelet transform. The figure caption follows Fig. 17. The P and x1 phases point to an azimuth of 90°.

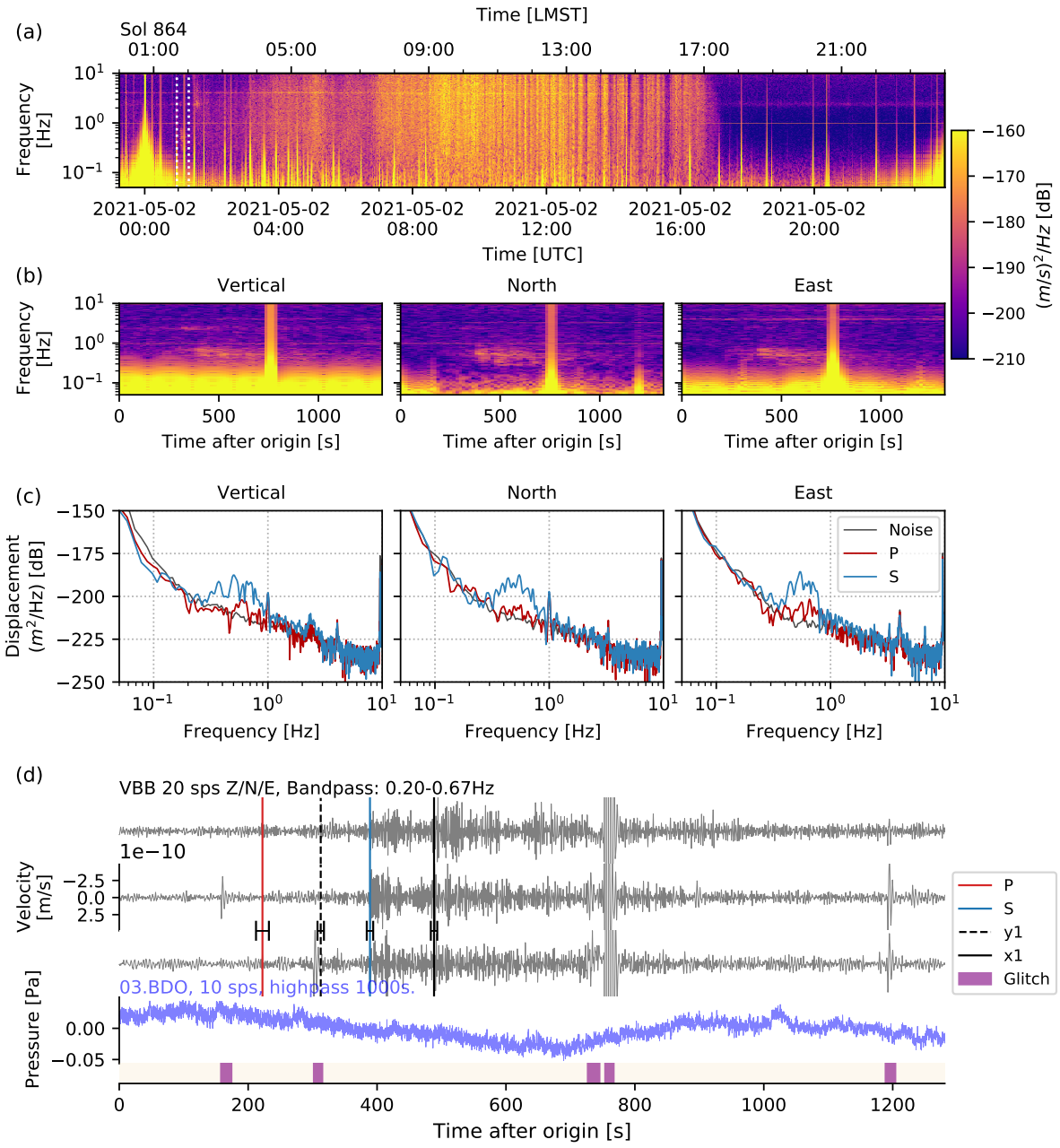

Figure 22: Event summary of S0864a (BB, QA). The figure caption and processing parameters follow Fig. 14.

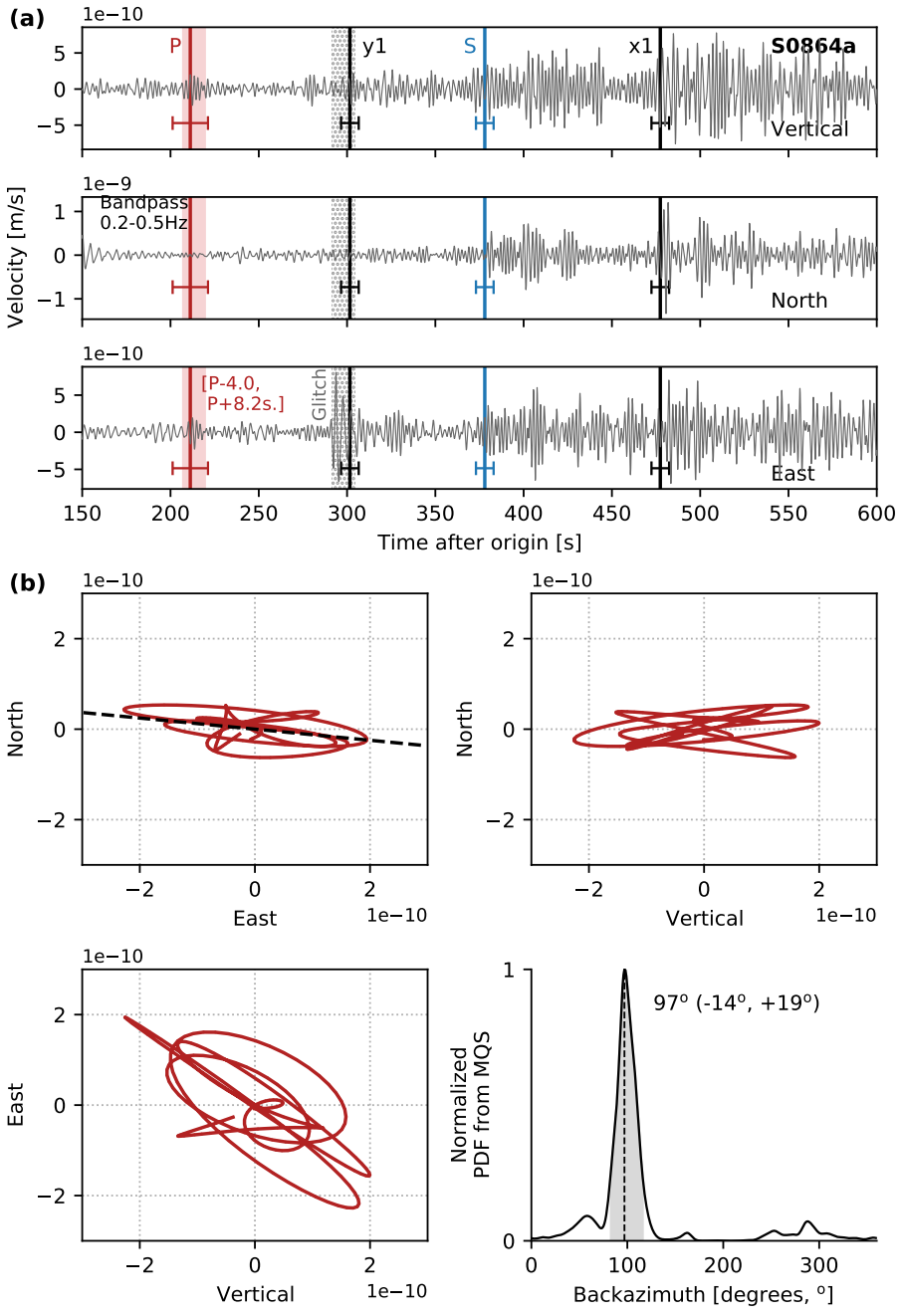

Figure 23: Polarization analysis of S0864a (BB, QA). The waveforms in (a) are bandpass filtered between 0.2-0.5 Hz as indicated, other details follow Fig. 16.

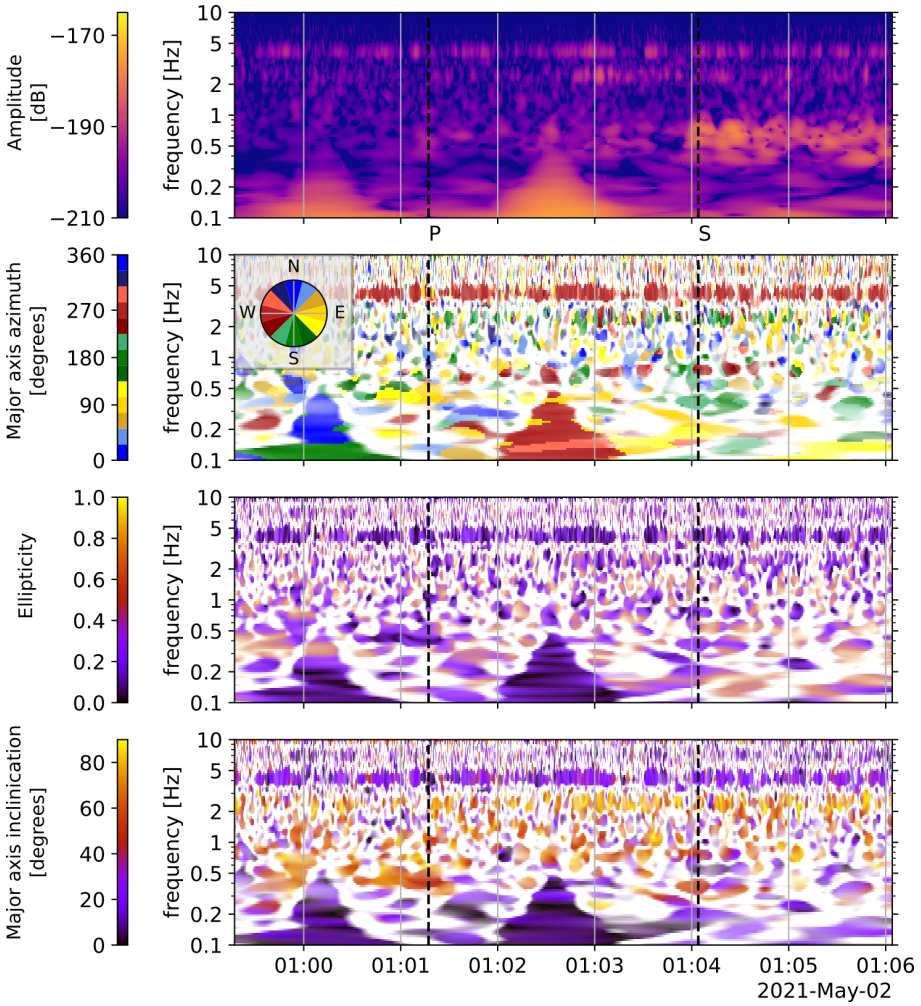

Figure 24: Polarization analysis of S0864a (BB, QA) using wavelet transform analysis. The figure caption follows Fig. 17.

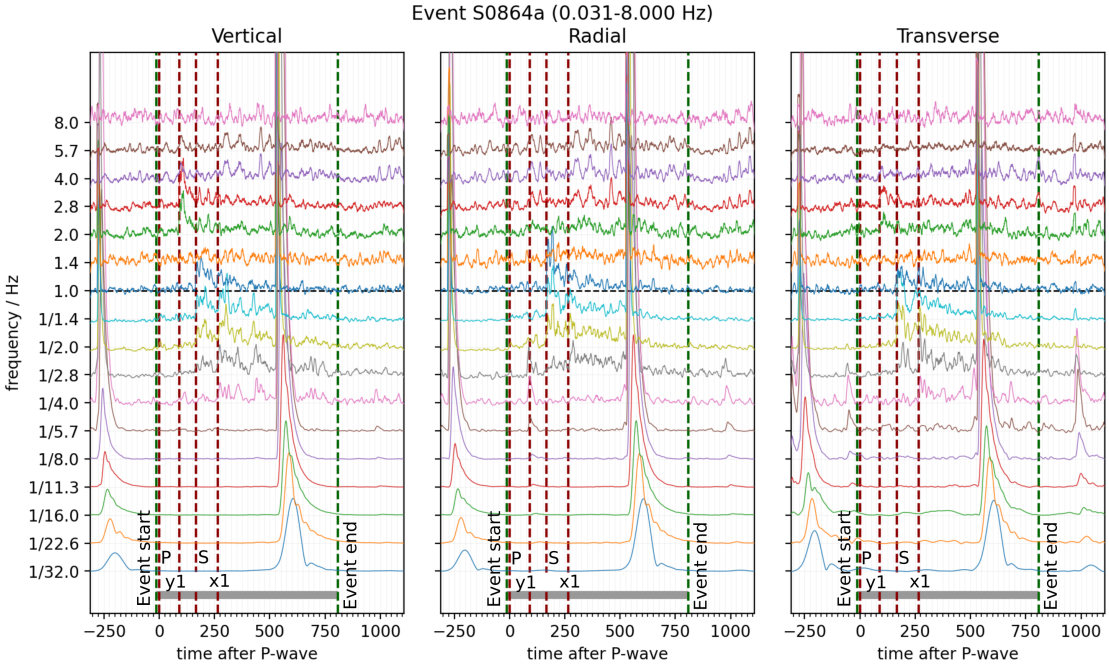

Figure 25: Filterbanks for S0864a (BB, QA). The figure caption follows Fig. 15.

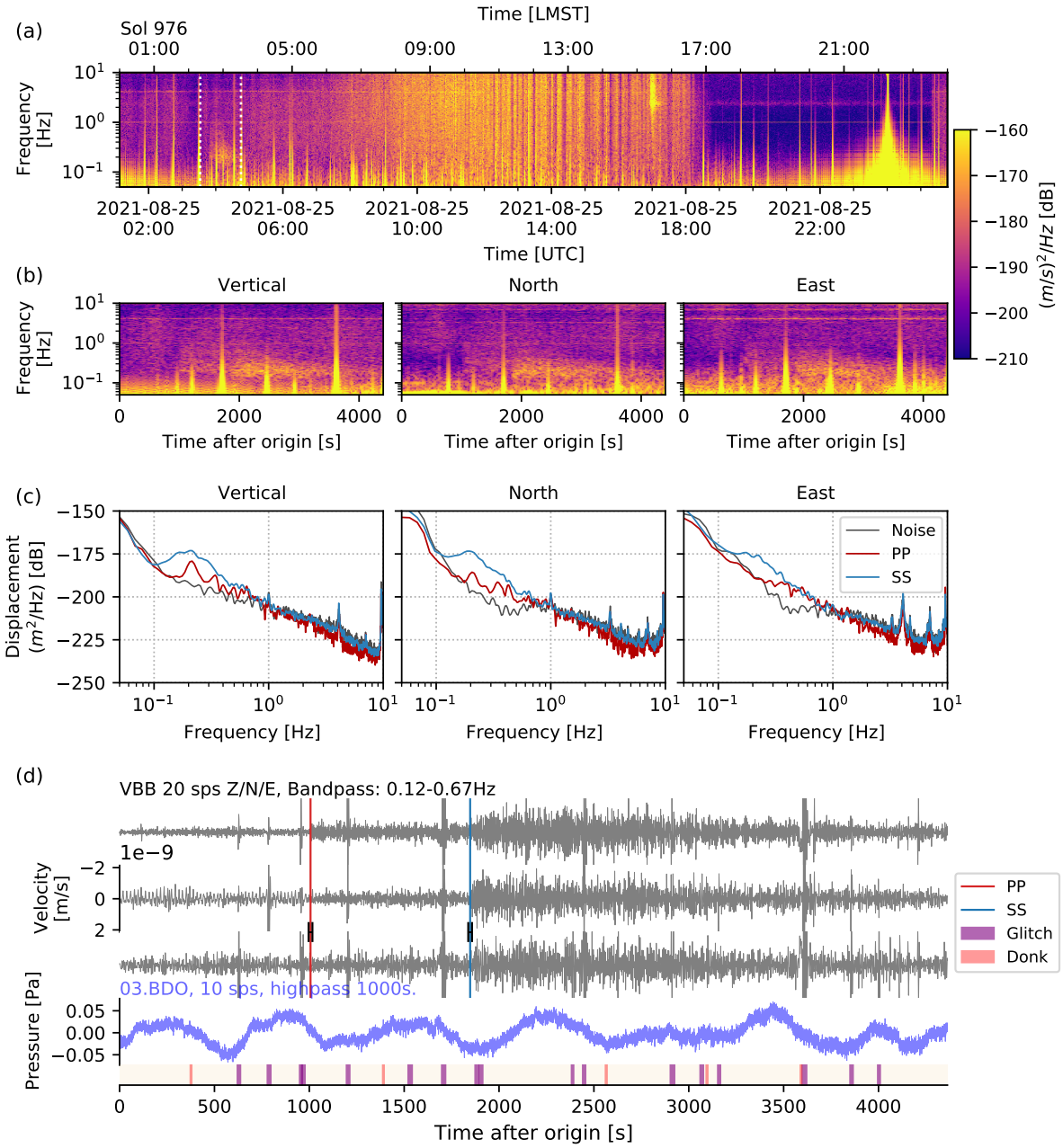

Figure 26: Summary of S0976a (LF, QA). The spectra are computed using a window length of 400 s with 50% overlap in (a), 120 s with 80% overlap in (b) and 30 s with 50% overlap in (c). Other details follow Fig. 14. Note clear presence of 25 s noise harmonics in pre-event noise on the North component.

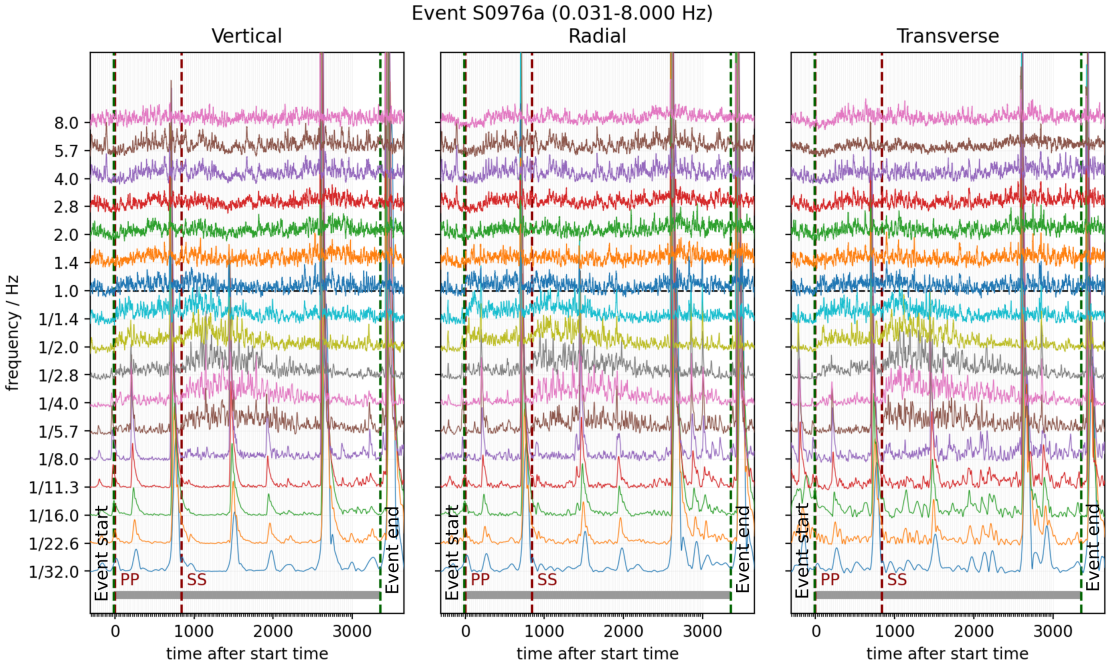

Figure 27: Filterbanks for S0976a (LF, QA). The figure caption follows Fig. 15.

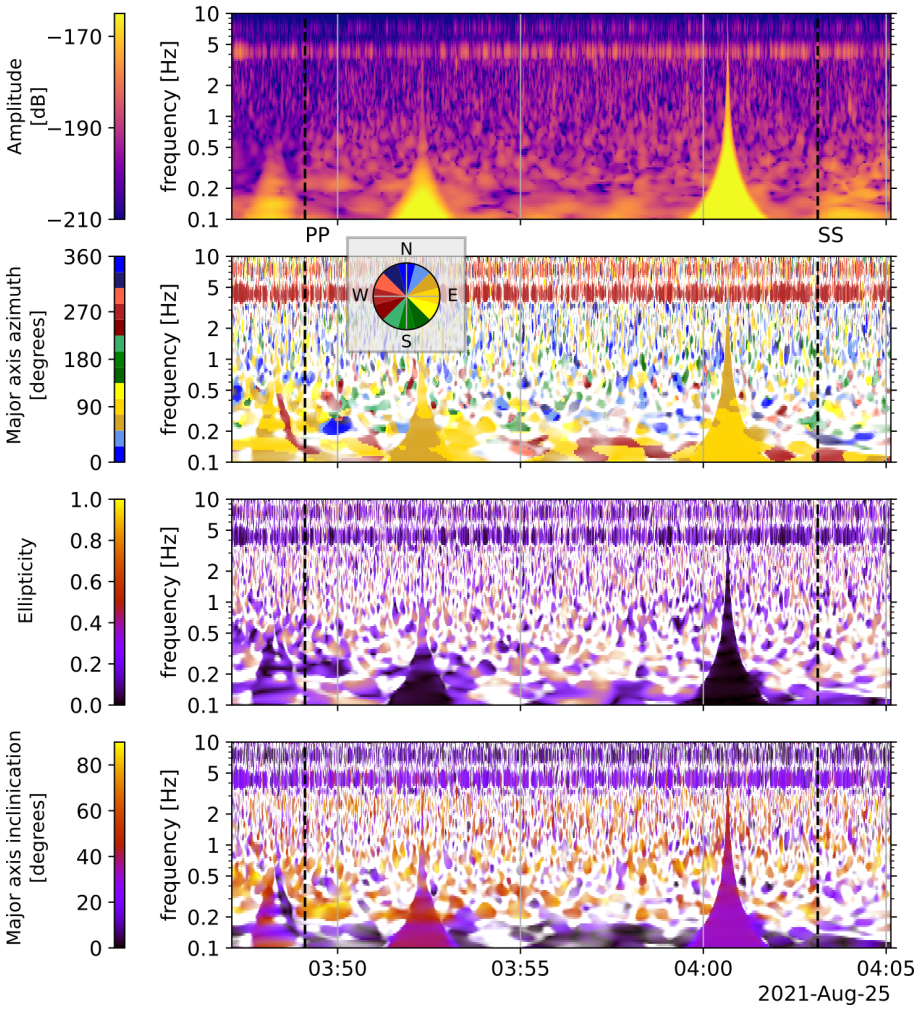

Figure 28: Polarization analysis of S0976a (LF, QA) using wavelet transform analysis. The figure caption follows Fig. 17.

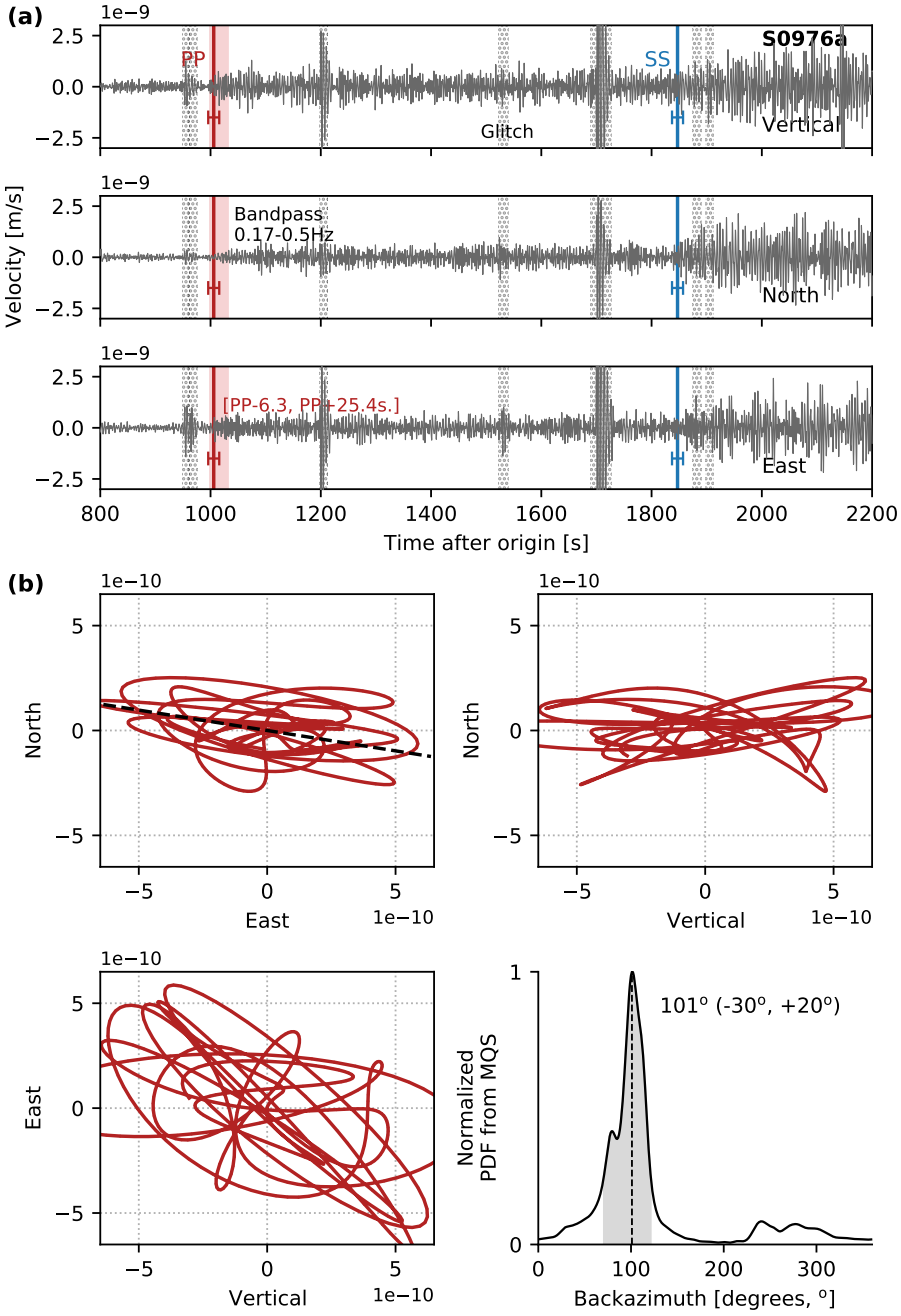

Figure 29: Polarization analysis of S0976a (LF, QA). The waveforms in (a) are bandpass filtered between 0.17-0.5 Hz as indicated, other details follow Fig. 16.

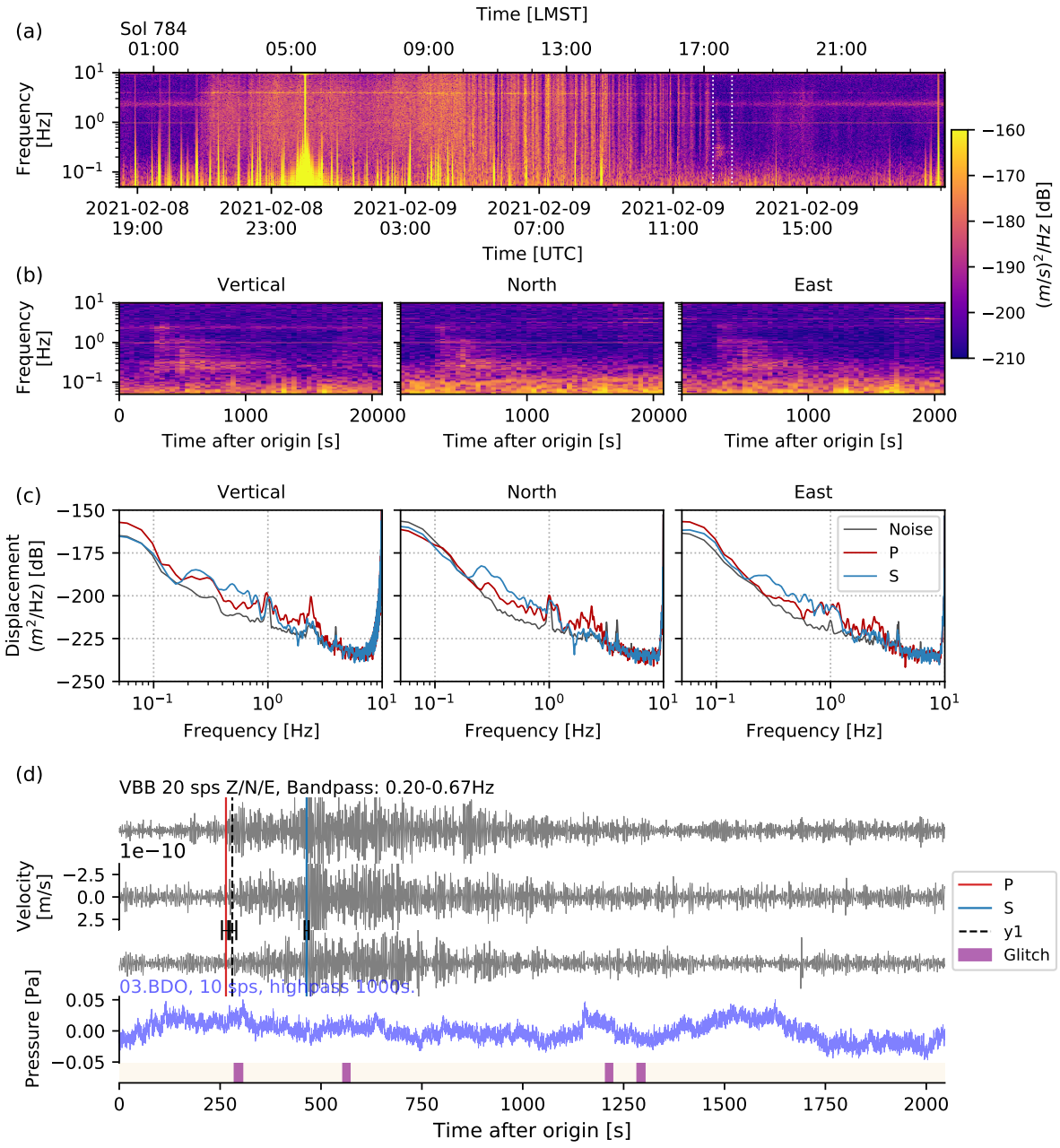

Figure 30: Summary of S0784a (BB, QB). The window lengths used are (a) 200 s (b) 50 s (c) 25 s. All panels were computed using an overlap of 50%. Other details follow Fig. 14.

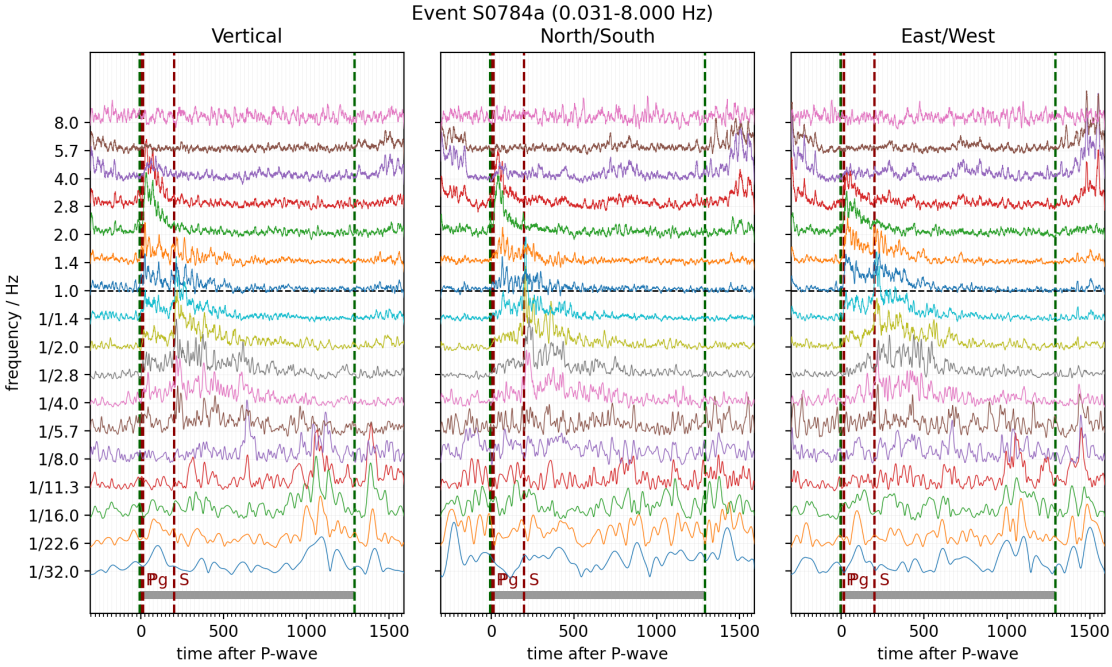

Figure 31: Filterbanks for S0784a (BB, QB). The figure caption follows Fig. 15.

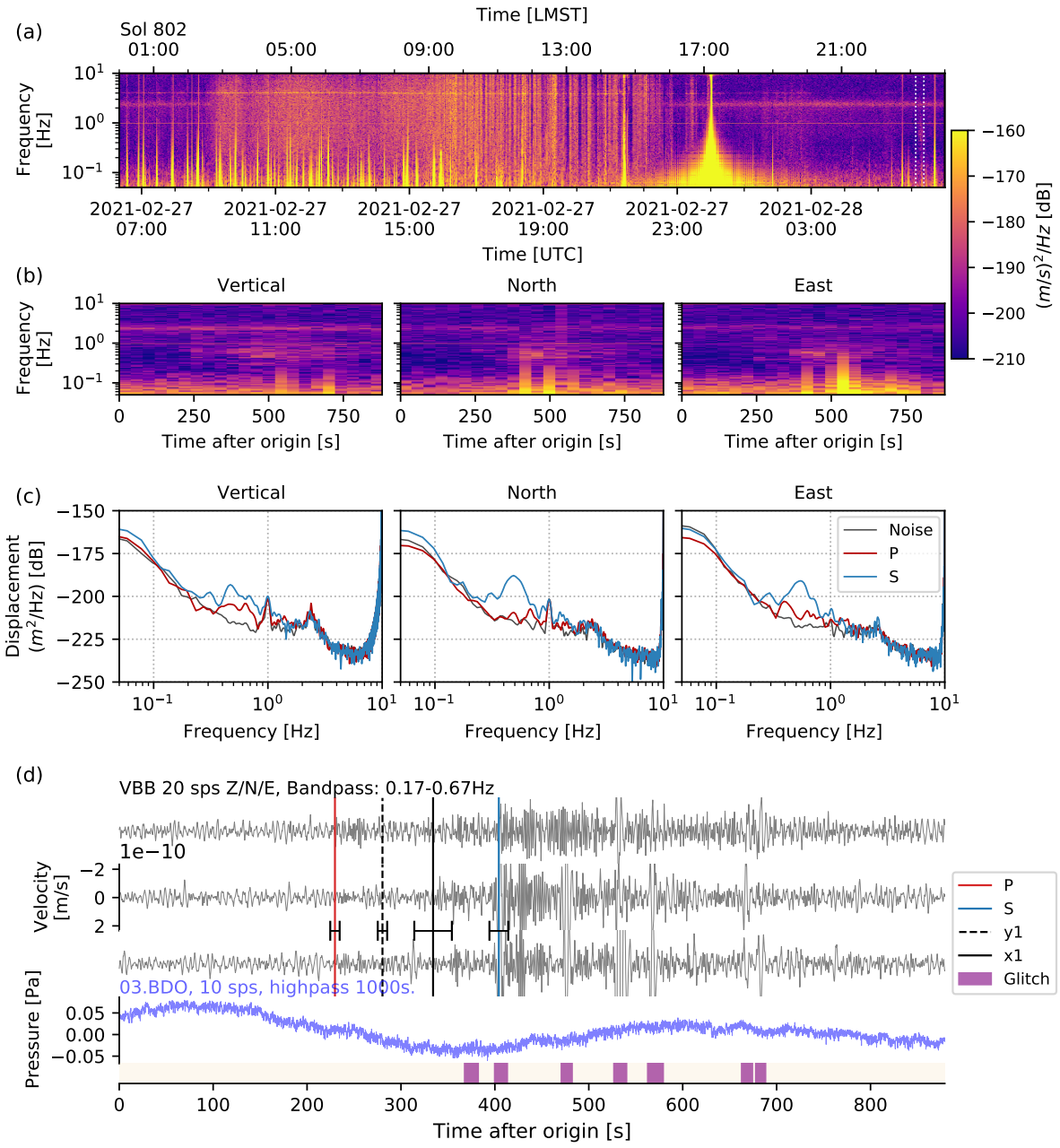

Figure 32: Summary of S0802a (BB, QB). The figure caption and processing parameters follow Fig. 14

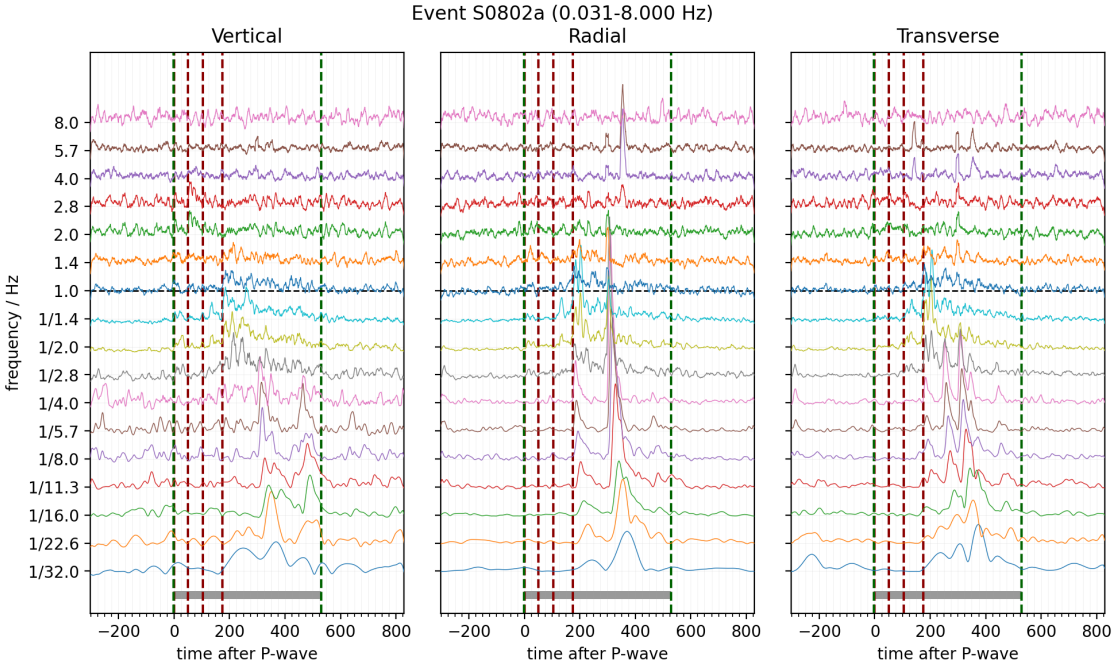

Figure 33: Filterbanks for S0802a (BB, QB). The figure caption follows Fig. 15.

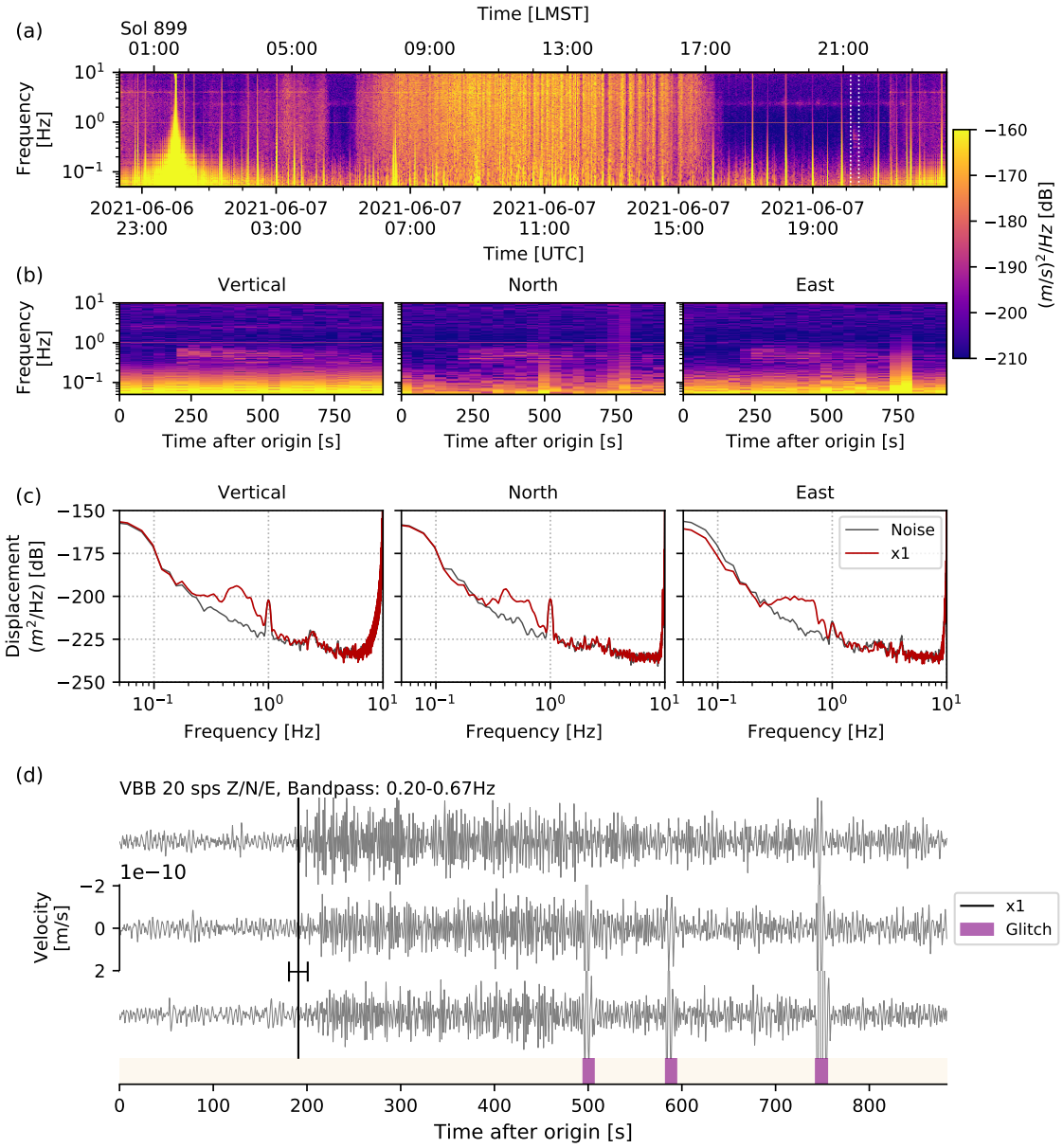

Figure 34: Summary of S0899d (LF, QB). The figure caption and processing parameters follow Fig. 14.

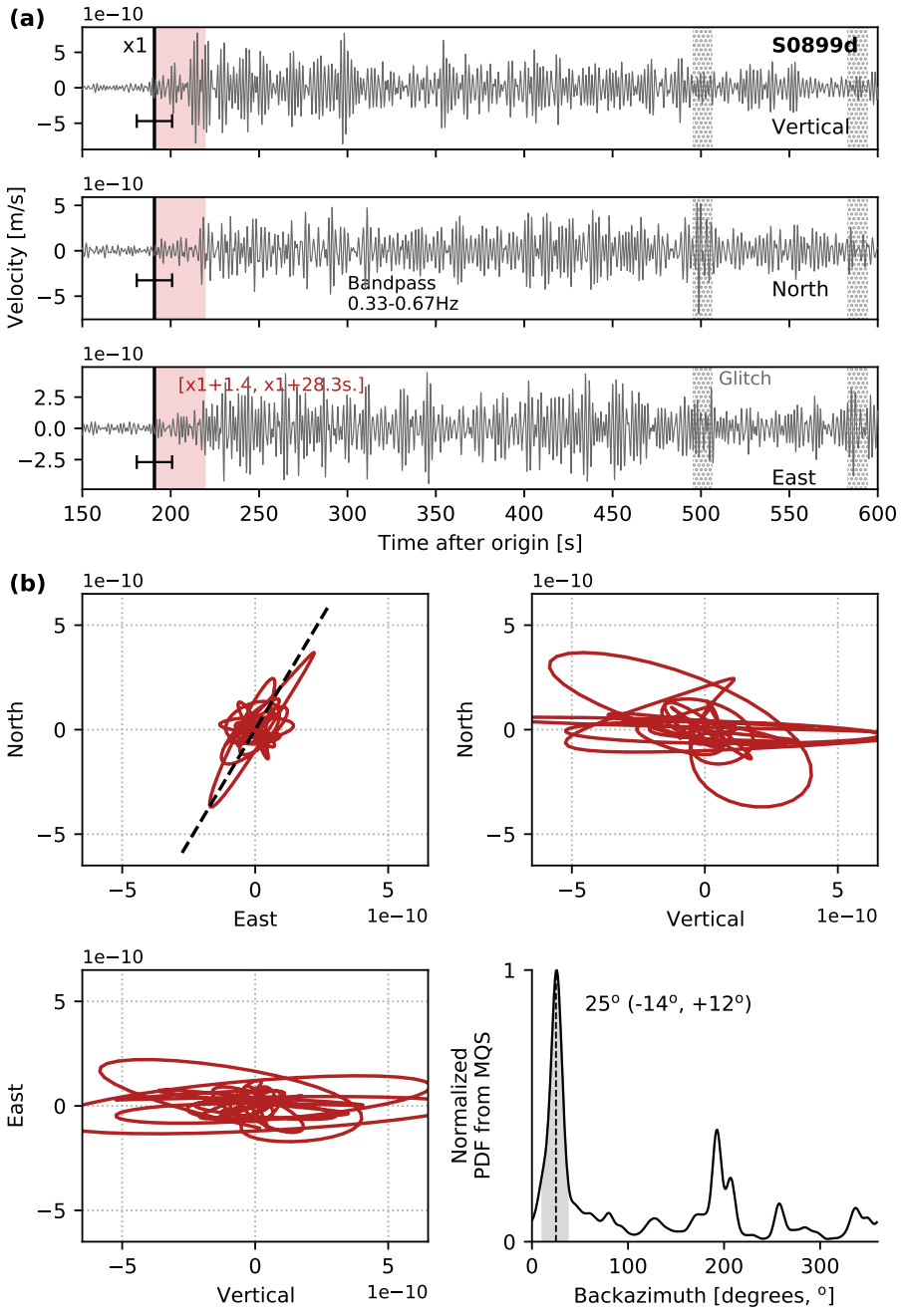

Figure 35: Polarization analysis of S0899d (LF, QB). The figure caption follows Fig. 16.

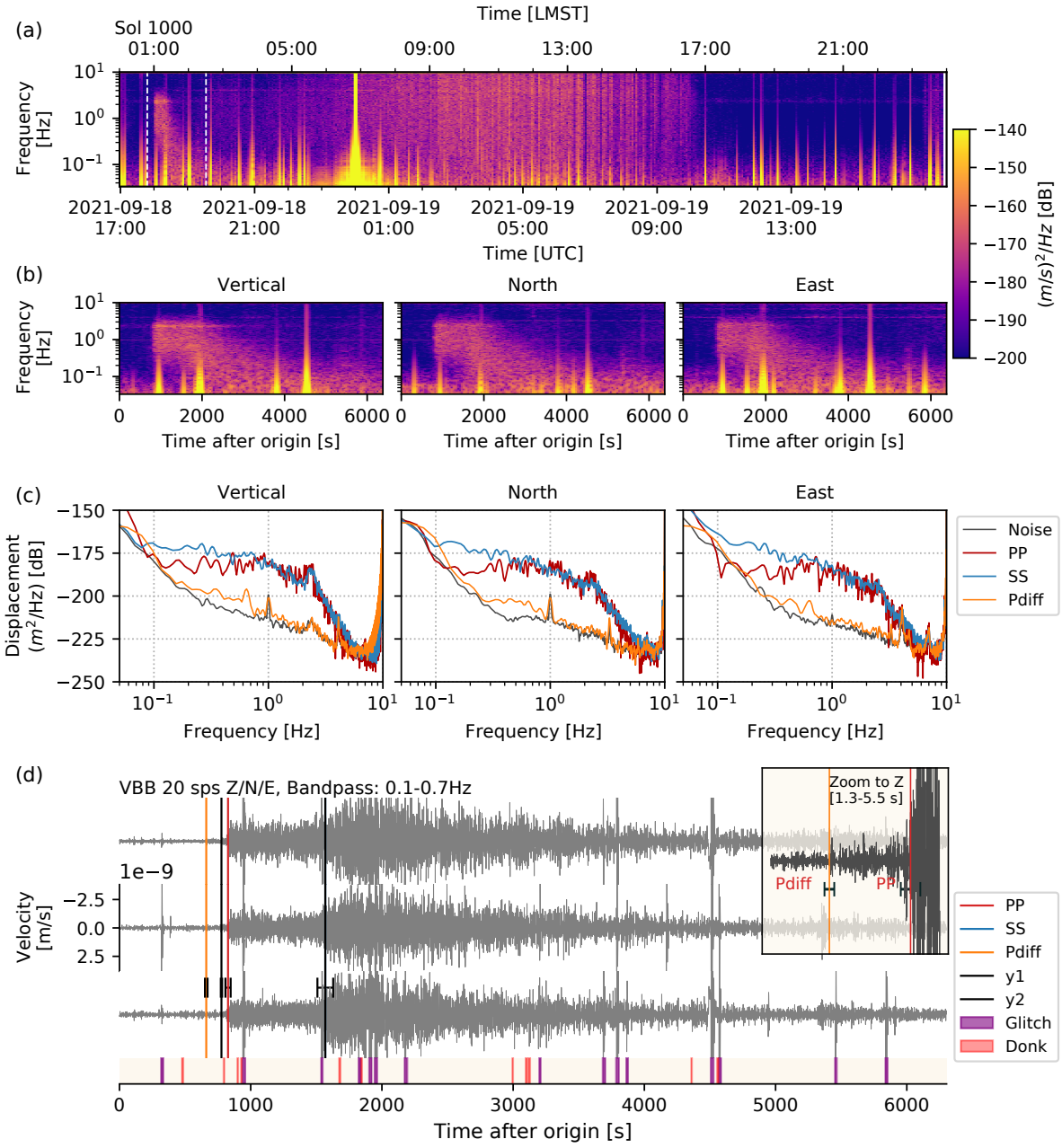

Figure 36: Summary of S1000a (BB, QB). The figure caption and processing parameters follow Fig. 14. The inset in panel (d) zooms around Pdiff and PP phases on the vertical component.

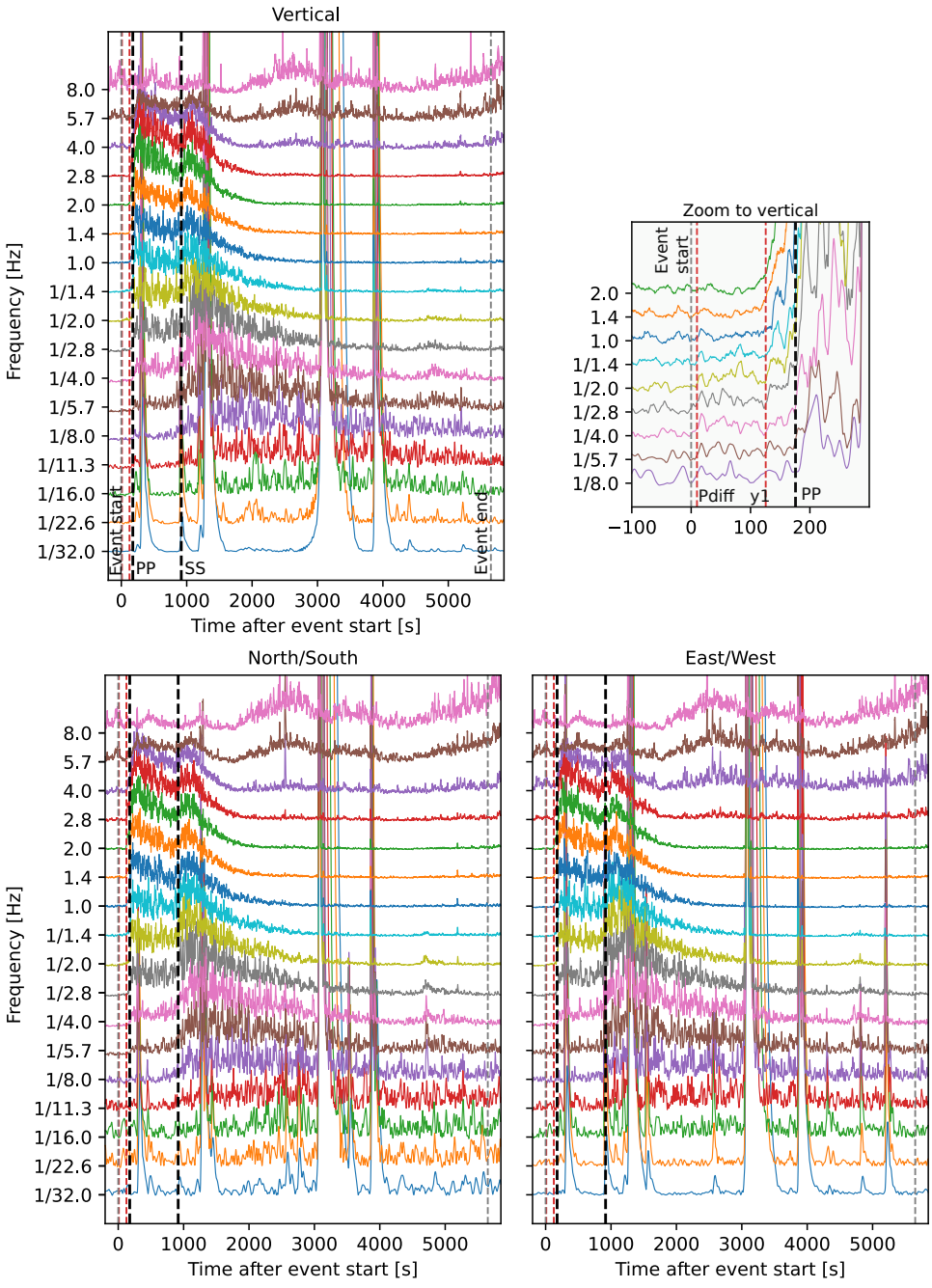

Figure 37: Filterbanks for S1000a (BB, QB) for vertical, North/South, and East/West components. The seismic phase picks that were used for locating the event are labelled. The inset zooms around the Pdiff and PP picks on the vertical component.

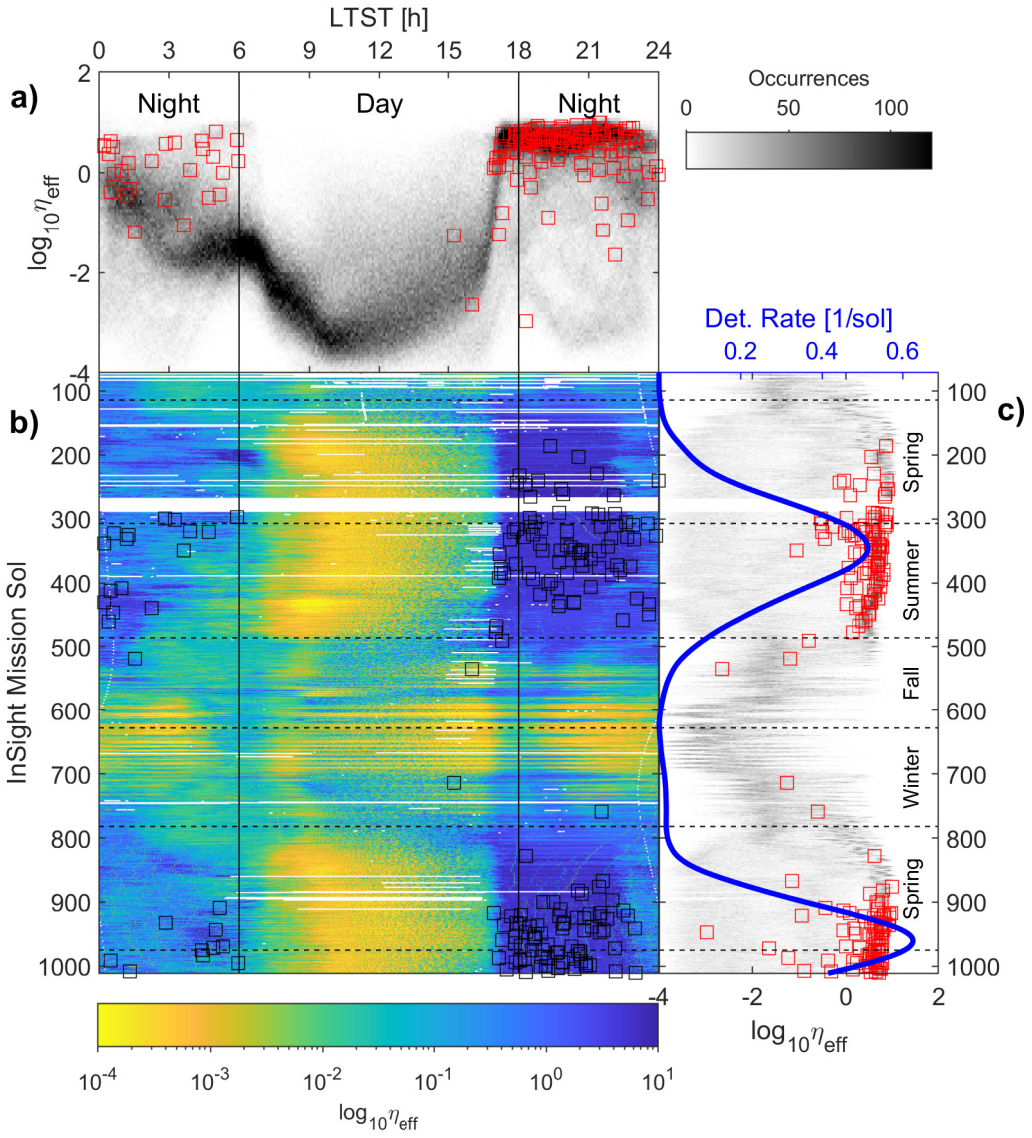

Figure 38: HF family: event rate estimation and detection efficiency, as function of sol number and Local True Solar Time (LTST). Events used all have displacements above -208 dB and SNR_S above 2.08, and assuming that the observed amplitude follows a power law with slope -0.12 events/dB, as resulting from an analysis of catalogue representativeness. (a) count density of detection efficiency, evaluated in 2 min windows and plotted against LTST. Red squares indicate the detection efficiency at the times of detected events. (b) HF event detection times (black squares) compared to the detection efficiency (colored background), with sol number on the vertical and LTST on the horizontal axis. Note that, in LTST, sunrise and sunset occur at 06:00 and 18:00 regardless of season; the sudden increase of detection efficiency at about 17:00 LTST corresponds to the collapse of atmospheric turbulence. (c) as (a), but plotted as function of sol number. In addition, a Kernel density estimation of the event rate is overlain (upper horizontal axis). This rate is not corrected for the variable detection efficiency. The apparent decrease of the estimated rate after sol 950 is an artefact of the limited observation window, in connection with the 10 sols KDE bandwidth.

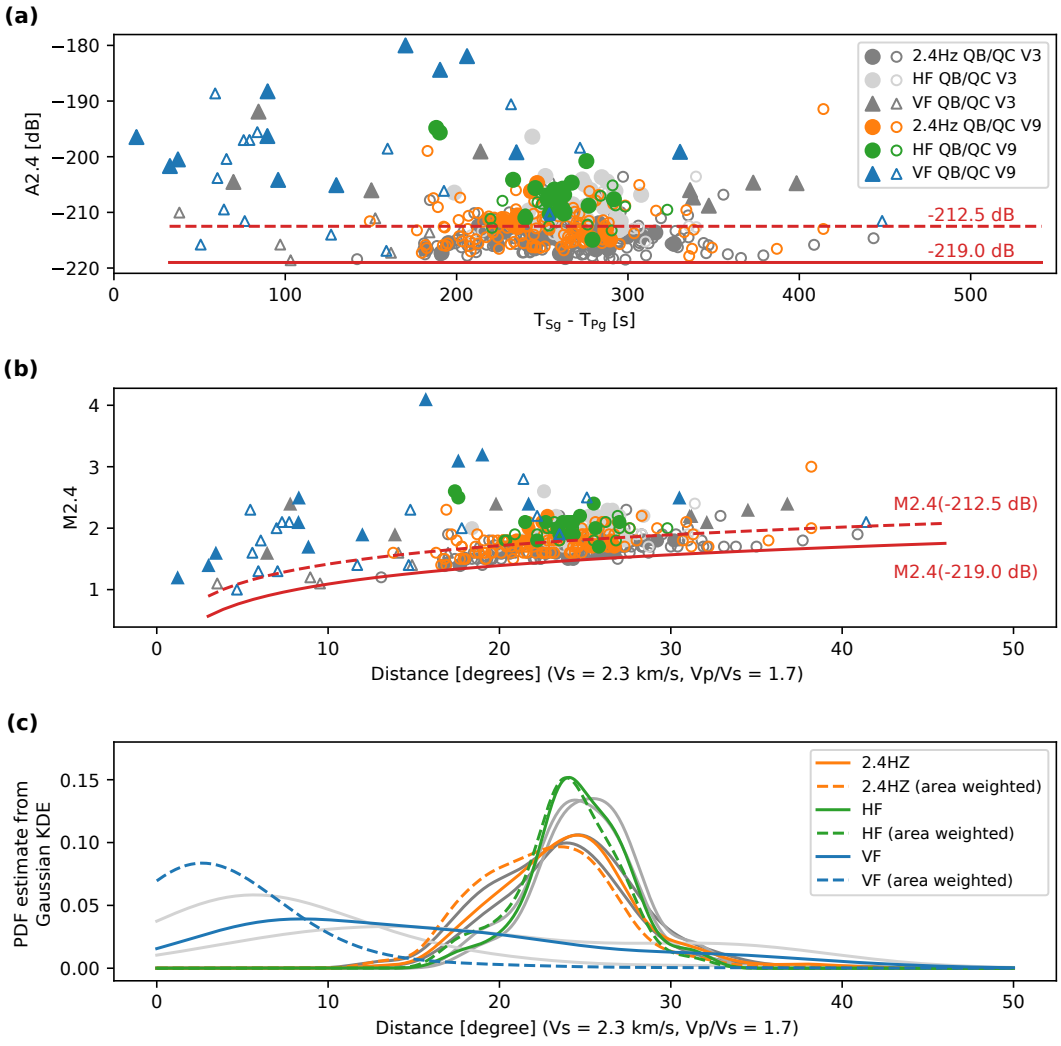

Figure 39: HF events magnitude and amplitude comparison after van Driel et al. (2021). (a) Spectral amplitude measured on the 2.4 Hz resonance versus $Pg-Sg$ differential arrival times. The red solid line shows the detection threshold of -219 dB during the quietest times. The red dashed line is the amplitude (-212.5 dB) at which most events are visible outside the 2.4 Hz resonance. (b) The magnitude measured at 2.4 Hz resonance vs. the computed distance. The seismic wave speeds used for distance computation are indicated in the x-axis label. (c) Kernel density estimation (KDE) vs. distance.

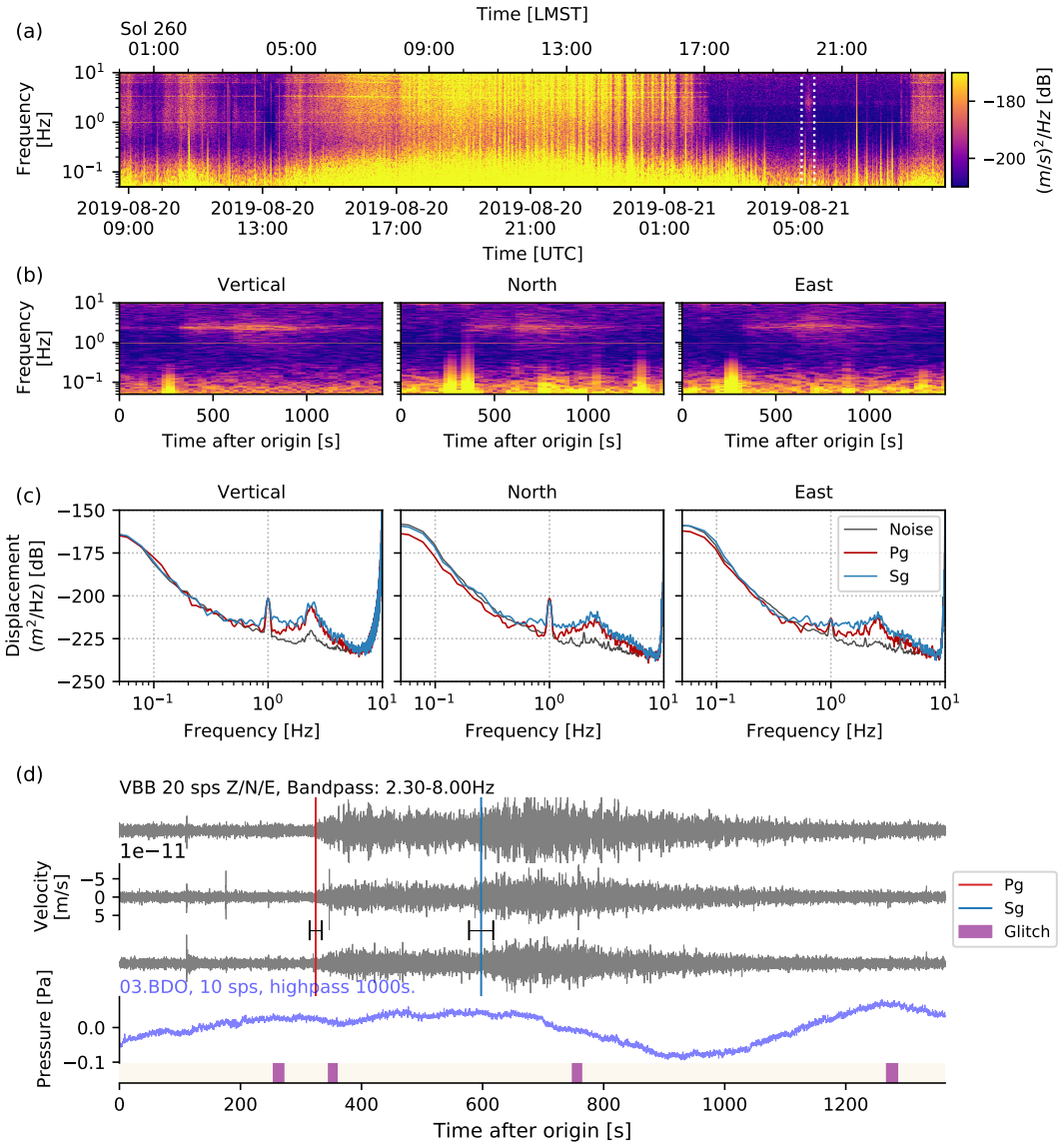

Figure 40: Summary of S0260a (HF, QB). The window lengths used are (a) 200 s with 80% (b) 80 s with 80% overlap, and (c) 25 s with 50%. The Pg and Sg picks from MQS are marked with their uncertainties. Note the weak energy extending down to 5 s period in panels (b) and (c). See the caption of Fig. 14 for other details.

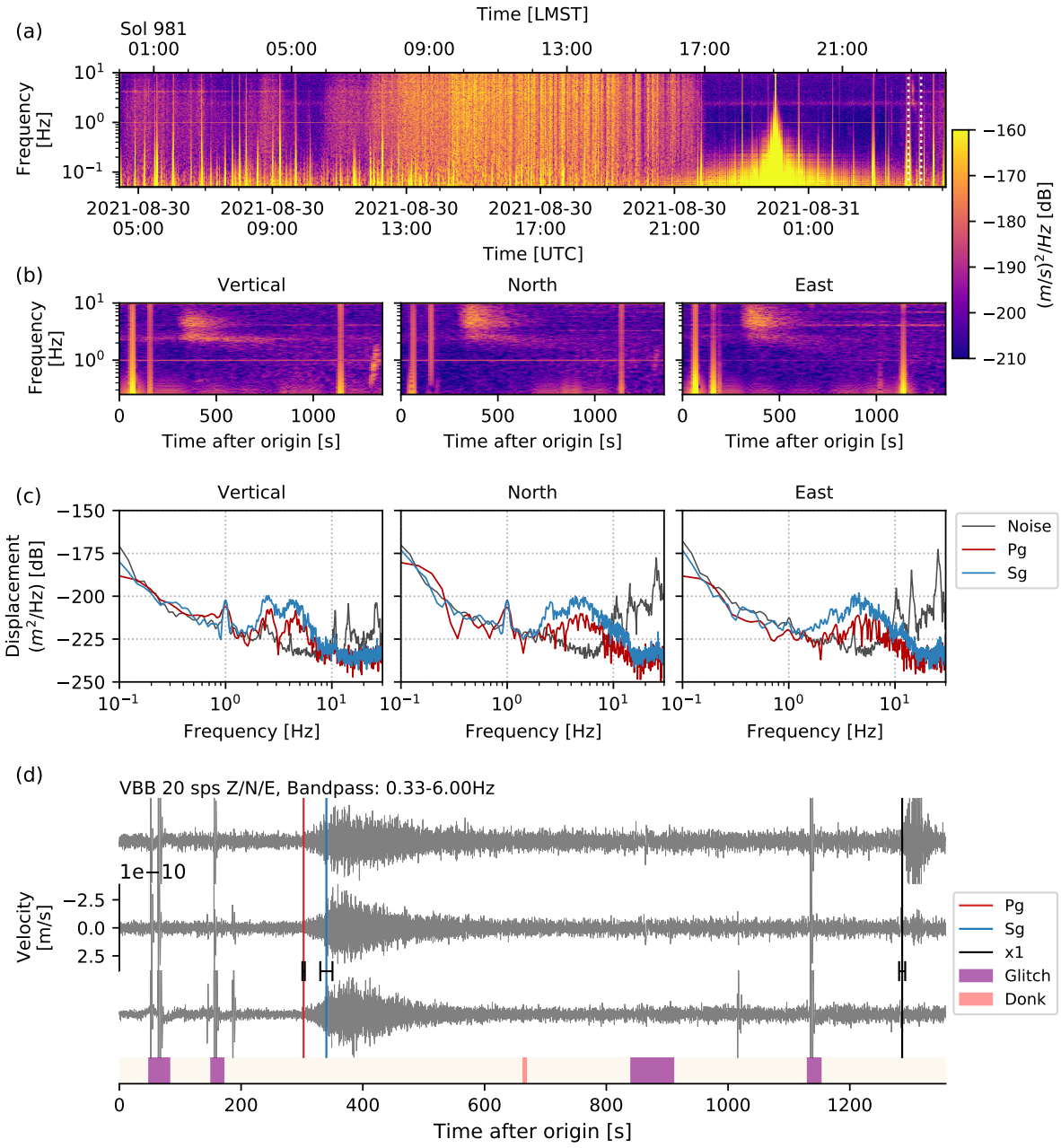

Figure 41: Summary of S0981c (VF, QB). The window lengths used are (a) 200 s (b) 50 s (c) 25 s. All panels were computed using an overlap of 50%. The chirp signal is visible in the spectrograms in panel (b), as well as in the time-domain in (d) just before the event end time.

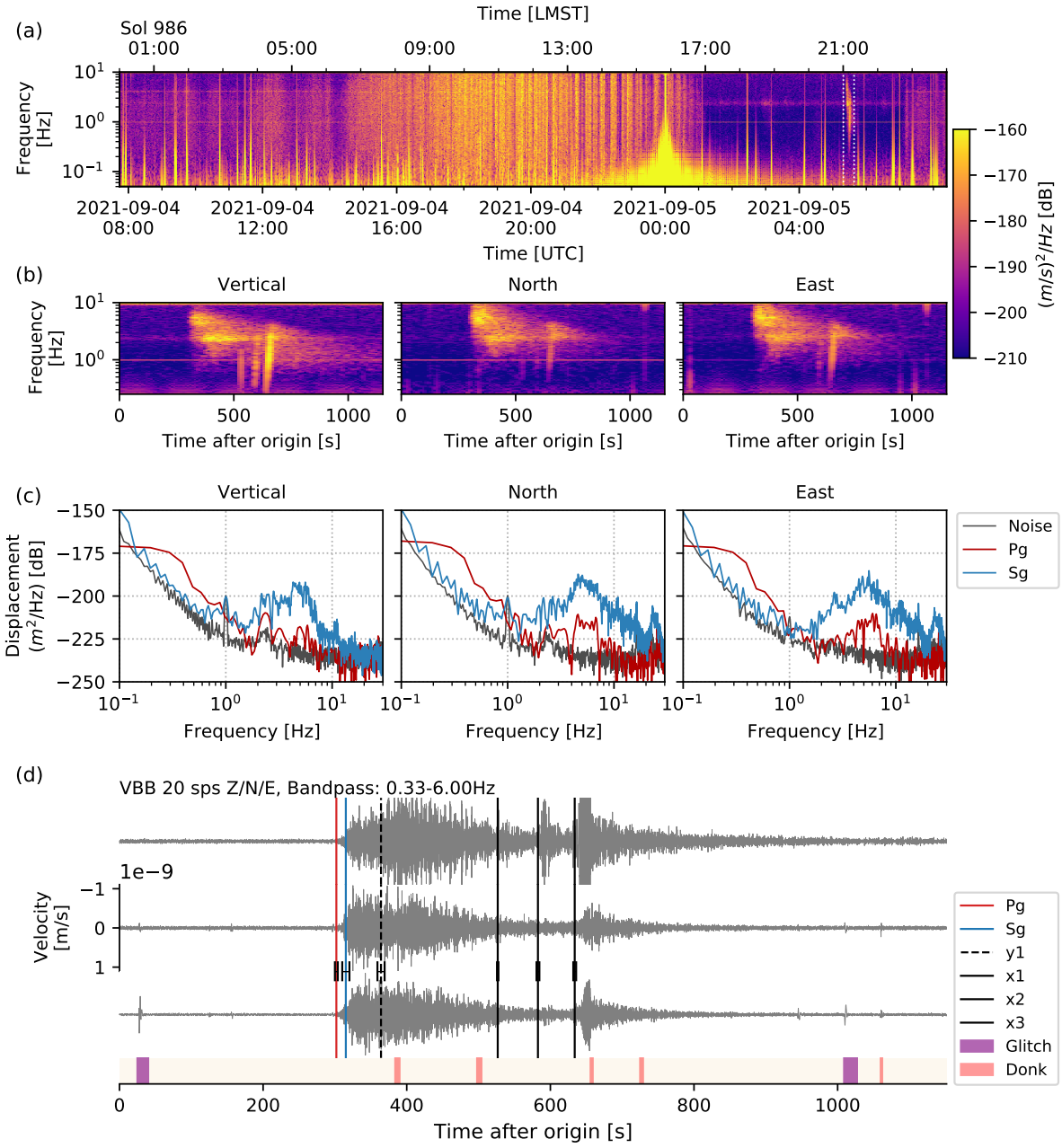

Figure 42: Summary of S0986c (VF, QB). The three chirp signals are visible in the spectrograms in panel (b), as well as in the time-domain in (d). The figure caption and processing parameters follow Fig. 41.

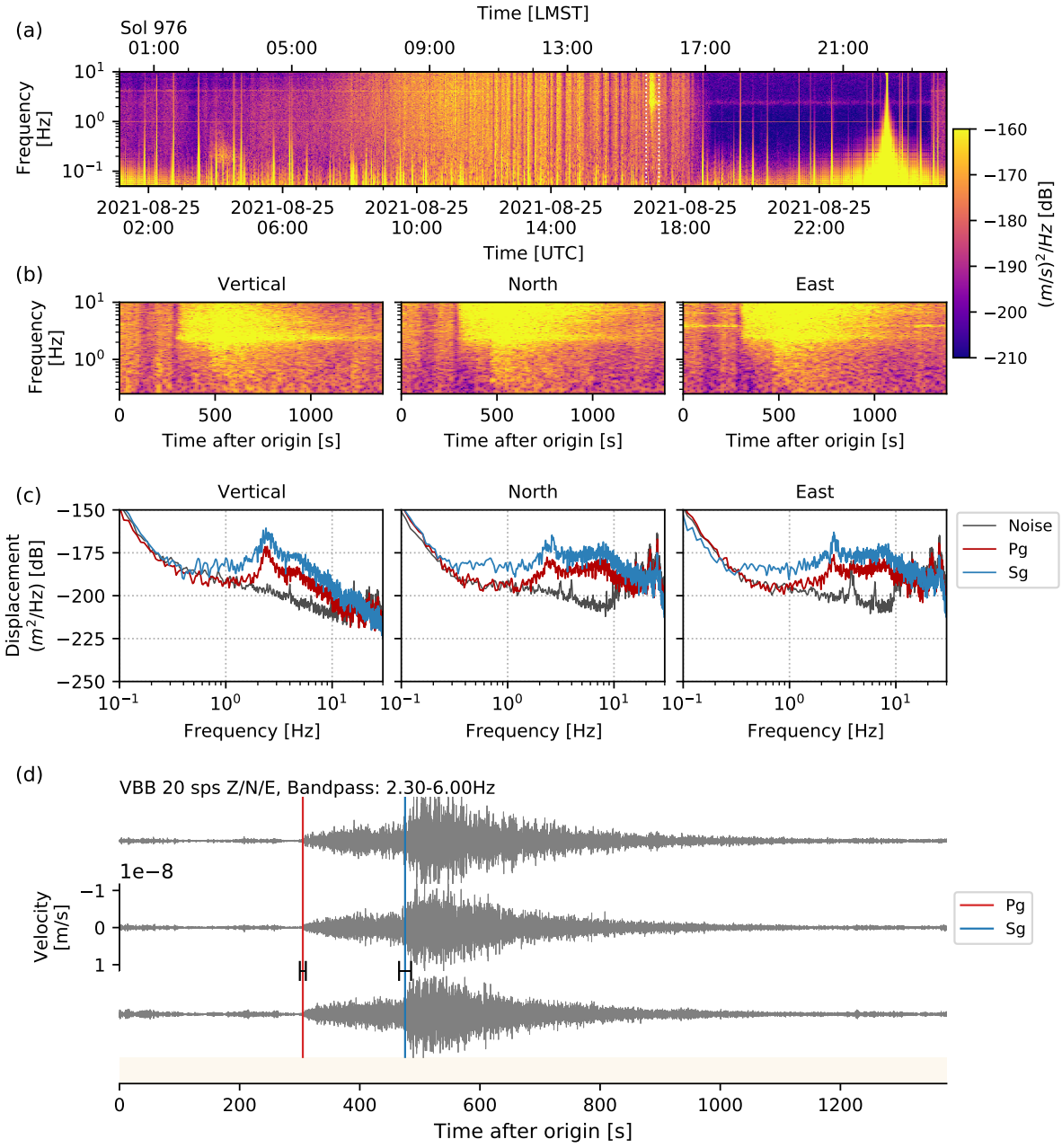

Figure 43: Summary of S0976b (VF, QB). The figure caption and processing parameters follow Fig. 41.

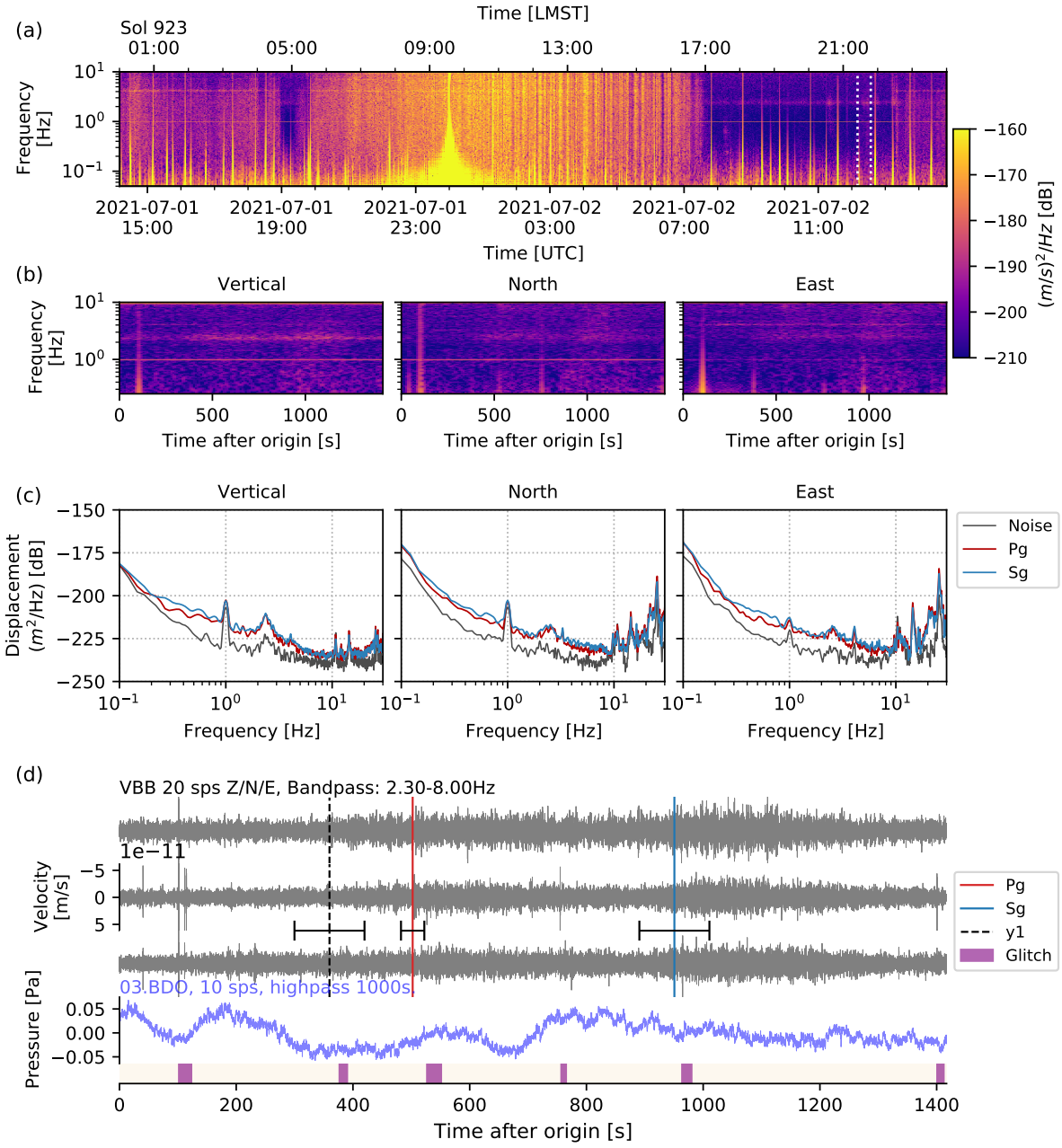

Figure 44: Summary of S0923d (VF, QC). The figure caption and processing parameters follow Fig. 41.

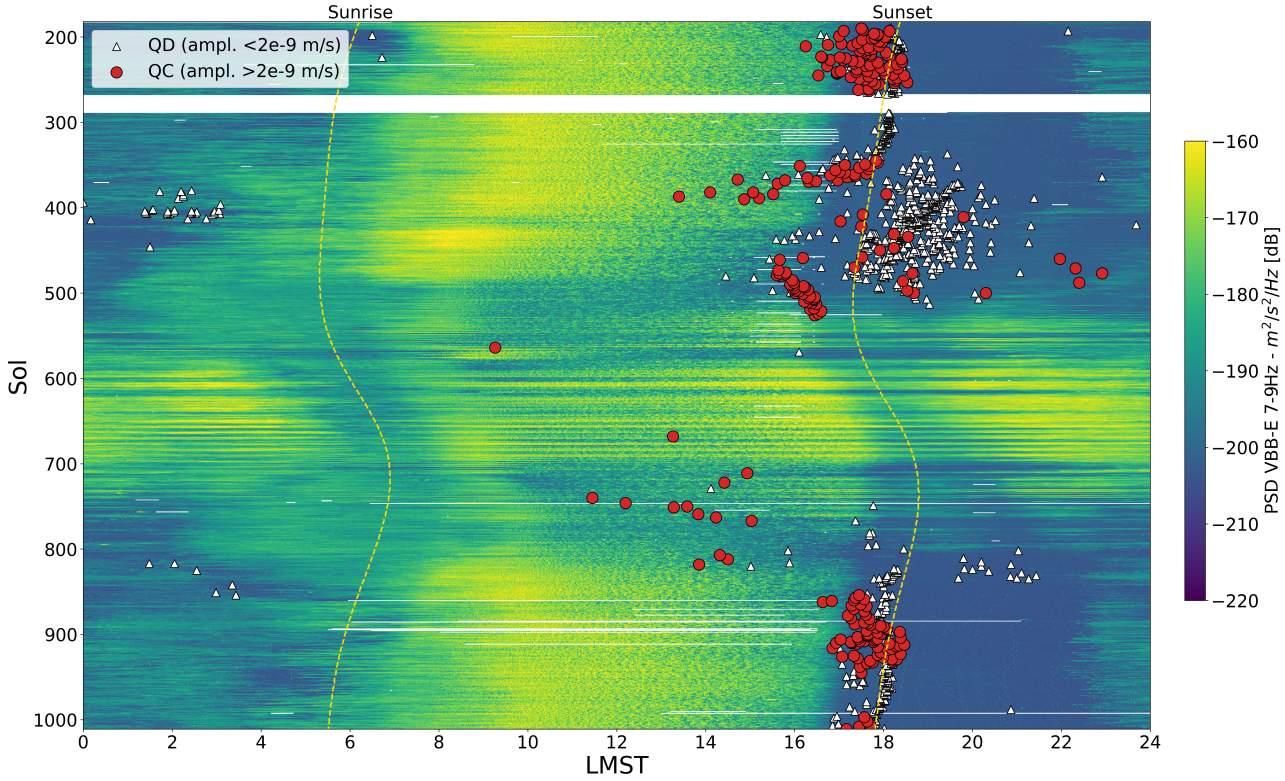

Figure 45: The spectrogram stack for catalogued SF events from sol 182 (start of continuous 20 sps data) to sol 1011. Background noise given by energy in 7-9 Hz bandpass on the East component (channel and location codes 02.BHE and 07.BLE; Lognonné et al. (2019)). Event quality is based on the amplitude threshold as indicated in the legend, which is computed as the maximum of horizontal energy using the Euclidean norm.

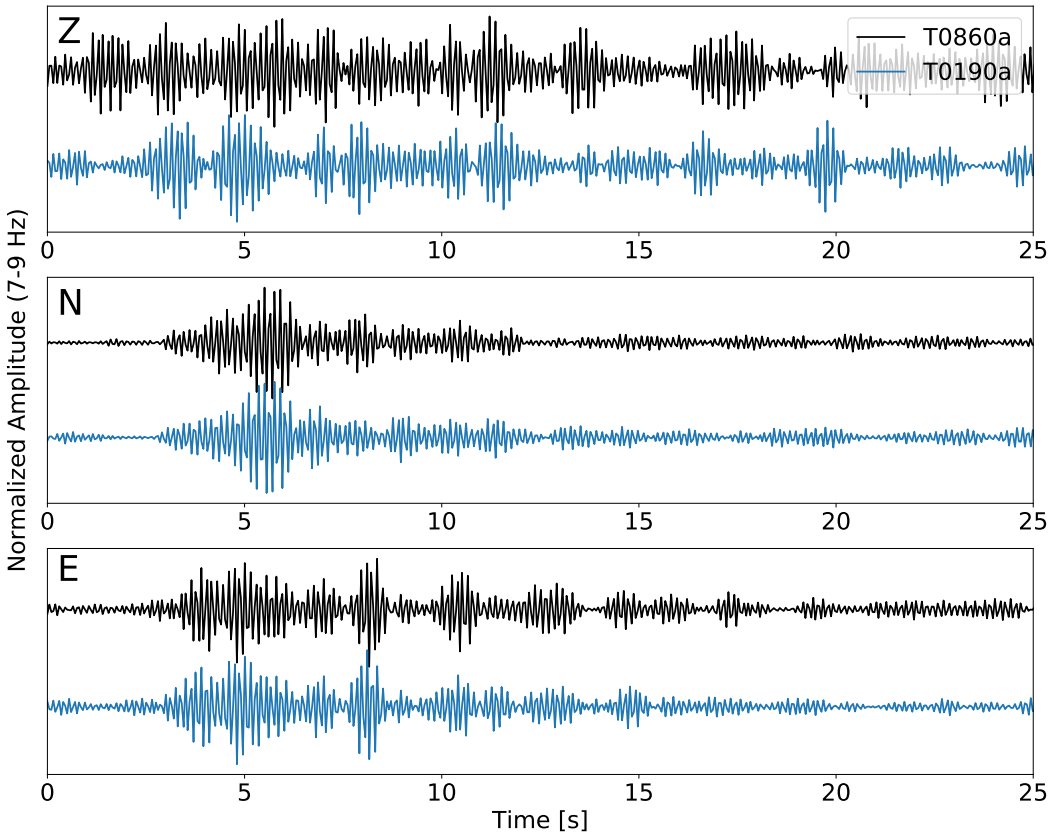

Figure 46: Example of two SF events with nearly repeating waveforms (T0190a and T0860a, both QC), approximately one Martian year apart. Note that the signal is stronger on the horizontal components with respect to the background noise, which is one of the characteristics of the SF events. The amplitudes are normalized individually for each component, and shifted along the y-axis for visual clarity.